Silver nanoprisms in plasmonic organic solar cells

Zhixiong Cao

To cite this version:

Zhixiong Cao. Silver nanoprisms in plasmonic organic solar cells. Micro and nanotechnologies/Microelectronics. Ecole Centrale Marseille, 2014. English. NNT : 2014ECDM0015 . tel-01406363

ÉCOLE CENTRALE DE MARSEILLE

École Doctorale ED 353 - Sciences Physiques pour l'Ingénieur

Préparée au laboratoire IM2NP, UMR-CNRS 7334, équipe Opto-PV

THÈSE DE DOCTORAT

pour obtenir le grade de

DOCTEUR de l'ÉCOLE CENTRALE de MARSEILLE

Discipline : Micro Nano électronique

TITRE DE LA THÈSE : Silver nanoprisms in plasmonic organic solar cells

Par

CAO Zhixiong

Directeur de thèse : ESCOUBAS Ludovic
Co-directrice de thèse : CHEN Zhuoying

Soutenue le 15 Décembre 2014

devant le jury composé de :

LEQUEUX Nicolas	Prof de l'ESPCI, Paris	Rapporteur
VIGNAU Laurence	Prof de l'Université de Bordeaux I, Bordeaux	Rapporteur
RATIER Bernard	Prof de l'Université de Limoges, Limoges	Examinateur
ESCOUBAS Ludovic	Prof de l'Université d'Aix-Marseille, Marseille	Directeur de thèse
CHEN Zhuoying	Chargé de recherche au CNRS, ESPCI, Paris	Co-directrice de thèse

Acknowledgements

First of all, this thesis is a project of collaboration between Chinese Scholarship Council (CSC) and Ecole Centrale groups of Lille, Nantes, Lyon, Paris, and Marseille. I appreciate the CSC and Ecole Centrale de Marseille, as well as the OPTO-PV group, IM2NP (Institut Matériaux Microélectronique Nanosciences de Provence), Aix-Marseille University and CNRS 7334 & 8213 for financial support.

I would like also thank my thesis committee, which includes Prof. VIGNAU Laurence, LEQUEUX Nicolas and RATIER Bernard.

Particularly, I really appreciate my thesis supervisors, Dr. CHEN Zhuoying and Prof. ESCOUBAS Ludovic. They helped me so much: they gave me many advices on experiments, took a lot of time to correct all my thesis and paper in detail…. Anyway, without their helps, tolerance and encouragement, I could probably not finish my thesis. Thank you, my supervisors!

I also want to thank my dear brother, Mr. CAO Chaoqun. Without his sacrifice and financial support, I could not finish my studies in high school and in university, and so that I would not finish my thesis. I would like to say: you are great, my brother!

I also acknowledge the technicians, M. FAURE Yves, WARCHOL François and COMBES Alain, FIORIDO Tomas, as well as mu colleagues and friends: PASQUINELLI Marcel, BARAKEL Damien, BRISSONNEAU Vincent, BERENGUIER Baptiste, BOU Adrien, BRUCKNER Jean-Baptiste, WOOD Thomas, ZHU Mingxuan and VEDRAINE Sylvain for their helps. I appreciate Dr. XU Xiangzhen (ESPCI, Paris), the courtesy of Concept Scientific Instruments and ScienTec Company for their helps in characterizations.

In the end, I would like to thank all of my friends and colleagues appeared in my life in France. It was a joyful and colorful life staying in France with them.

Table of Contents

Table of Figures

List of Tables

General introduction

There has been a strong global demand for renewable and clean energy over the last decades due to the rapid consumption of non-renewable fossil fuels and the resulting greenhouse effects. Photovoltaics, which can convert the energy of sunlight into electricity, represent one of the most promising avenues to harvest clean and renewable energy. Among different photovoltaic technologies, the conjugated polymer/fullerene solar cells have been intensively investigated due to advantages such as property tunability through chemical modifications and the compatibility to low-cost manufacturing processes. Despite these advantages, the power conversion efficiency of organic photovoltaic (OPV) devices still has to be improved for them to be commercialized in large scale. Among different strategies, the incorporation of metallic nanoparticles with sub-wavelength size represents an important tool to improve the device performance through boosting the light harvest and the charge generation efficiency in optical thin OPV devices.

In this thesis, we synthesized silver nanoprisms (Ag NPSMs) through thermal reduction method and we incorporated them into the PEDOT:PSS layer of organic solar cell (OSC). PEDOT:PSS layer typically acts as a buffer layer between photoactive layer and anodic electrode in OPV devices. We studied the effects of such incorporation on the structural, optical and electrical properties of PEDOT:PSS films and the device performance of the resultant plasmonic solar cells.

Chapter I presents the background knowledge on OPV and plasmonic OPV devices. This knowledge includes the state-of-art of photovoltaic results, the operational mechanism of OPV devices, introduction on bulk heterojunction OPV devices using polymer and fullerene derivatives, bulk plasmons, surface plasmons, localized surface plasmon resonance (LSPR) and the applications of LSPR in OPV devices.

Chapter II introduces the experimental materials, general methods and techniques used in this thesis. These techniques and methods were used throughout this thesis to prepare thin film samples and OPV devices, to optimize OPV devices, to characterize the structural, optical and electrical properties of the film samples, and to determine the photovoltaic characteristics of the resulting OPV devices.

Chapter III presents the synthesis and characterizations of the Ag NPSMs and their effects on the structural, optical and electrical properties of resulting hybrid PEDOT:PSS-Ag NPSM films.

In Chapter IV, we firstly present the optimization of the regular P3HT:PCBM bulk heterojunction solar cells through an optimization of parameters including thermal annealing, solvent annealing and the incorporation of additives. Subsequently, the effects of incorporating Ag NPSMs into PEDOT:PSS layer on the device performance are studied.

Appendix I describes the synthesis method used for Ag nanospheres. Appendix II describes an alternative approach to synthesize Ag NPSMs by one-step thermal reduction. Appendix III presents photovoltaic characteristics of OSC using PTB7 as donor material and PC70BM as acceptor. Appendix IV presents the method used to obtain a phase transfer of Ag NPSMs from aqueous solution to organic solvents. Appendix V lists the experimental results of incorporating Ag NPSMs within the photoactive layer of OSCs and as well as the resulting photovoltaic characteristics of the plasmonic OSCs.

Chapter I

Introduction and Background Knowledge

1.1. Introduction

In 2013, the oil was still the world's leading fuel and accounted for 32.9% of the global energy consumption, and the coal and natural gas took the second and third place, corresponding to 30.1% and 23.7% respectively. The renewable energy accounted for 2.7% of global energy consumption and 5.3% of global power generation [1]. In the field of renewable energy, photovoltaics (PV) represented at least 0.85% of the global electricity production in 2013 [2]. This is a very small proportion of the total global energy consumption. However, the solar energy reaching the earth per year is much more than the total energy consumed by humanity in one year (~ 10,000 times of the energy consumed in the year of 2004 [3]). This suggests that solar energy has a high potential capacity to contribute to our energy consumption.

For non-renewable energy source such as fossil fuels, they release huge amounts of greenhouse gas (CO_2, CH_4, etc.) and other air pollutants [4–6]. For example, the CO_2 emission of coal can be as high as 1000 g/kWh. Therefore, many governments form mutual agreements in the *Kyoto Protocol to the United Nations Framework Convention on Climate Change* to put an effort for the reduction of the emission of greenhouse gas. One promising choice to solve this problem is to utilize solar energy which is clean and renewable.

In brief, as solar energy has a high capacity to contribute to our ever growing needs of energy consumption, it is necessary to develop the photovoltaic technology to exploit this clean and renewable energy. Such technology, if able to replace entirely or partly those technologies based on fossil fuels, can lead to a significant reduction of greenhouse gas emissions.

1.2. State-of-art of photovoltaics

1.2.1. History and development of photovoltaics

A.E. Becquerel is probably the first researcher who reported the photovoltaic effect in 1839 [7]. This effect allows the transformation of solar energy directly into electricity. Then Charles Fritts created the first working solar cell in 1883 with a power conversion efficiency of about

1%. In 1941, Russell Ohl developed the first silicon *p/n* junction and since then the research on solar cells has been developed very rapidly. Up to 1959, the company Hoffman Electronics has achieved a commercial solar cell showing 10% power conversion efficiency (*PCE*). Up to date, the best solar cell fabricated from research laboratory can reach over 40% in *PCE* by various techniques and materials (record 44.4%, Figure 1.1).

According to the time of their first appearance, solar cells can be mainly classified into three generations. The first-generation solar cells are based on silicon wafers mainly containing single crystalline or polycrystalline silicon. These types of solar cells dominate the market owning to their excellent and stable industrial performance. However, without government subsidy, the fabrication cost of crystalline silicon solar cells is relatively high. Their performance can be summarized as follows:

- ✧ Single crystalline silicon solar cells: Today's best-performing crystalline silicon solar cells from laboratories achieve about 25% in *PCE* (Figure 1.1). Lower *PCE* of 15% ~ 18% can be achieved in cells fabricated by industry [8]. The market share of single crystalline solar cells to total worldwide PV production in 2012 was 40.3% [9].
- ✧ Polycrystalline silicon solar cells: The polycrystalline silicon solar cells have a laboratory efficiency record of 20.4% (Figure 1.1), while the industrial average efficiency is about 13% to 16% [8]. The market share of polycrystalline solar cells in 2012 was 45.0% [9]. This relatively higher market share is due to their cheaper production process comparing to single crystalline solar cells despite of their lower efficiency.

The second-generation solar cells are usually called thin-film solar cells. These cells are made from layers of semiconductors of only a-few-micrometer-thick and exhibit a relatively lower efficiency than those of first-generation solar cells. However, the thin film solar cells are much cheaper to produce due to the reduction of material and less expensive manufacturing processes. This generation of solar cells mainly contains three types: amorphous silicon (a-Si), cadmium telluride (CdTe) and copper indium gallium diselenide (CIGS) solar cells.

- ✧ a-Si solar cells typically have a thickness of a few microns which is much thinner than that of crystalline silicon solar cells (thickness ~ 180 microns).The efficiency of a-Si solar cells made from laboratories can be as high as 13.4% (Figure 1.1) while 10% of *PCE* can be achieved for commercial a-Si solar cells. In 2012, their market share was 4.5% [9].
- ✧ CdTe solar cells have an ideal bandgap (1.44 eV) and thus their absorption show a good match with the solar spectrum. CdTe solar cells have a laboratory efficiency of 20.4%

(Figure 1.1) and an industrial efficiency of 11% with a market share of 6.3% in 2012 [9]. Their modest efficiency together with the use of scarce and toxic elements (i.e. tellurium and cadmium) limit their large-scale commercialization.

- ✧ CIGS solar cells have a relatively high efficiency (laboratory efficiency 20.8%, Figure 1.1) but their mass production turns out to be relatively difficult at competitive prices. This is due to the vacuum processes and the high temperature treatments required in the manufacture as well as the scarcity of indium. Their industrial efficiency is 14% and they took 3.5% market share in 2012 [9].

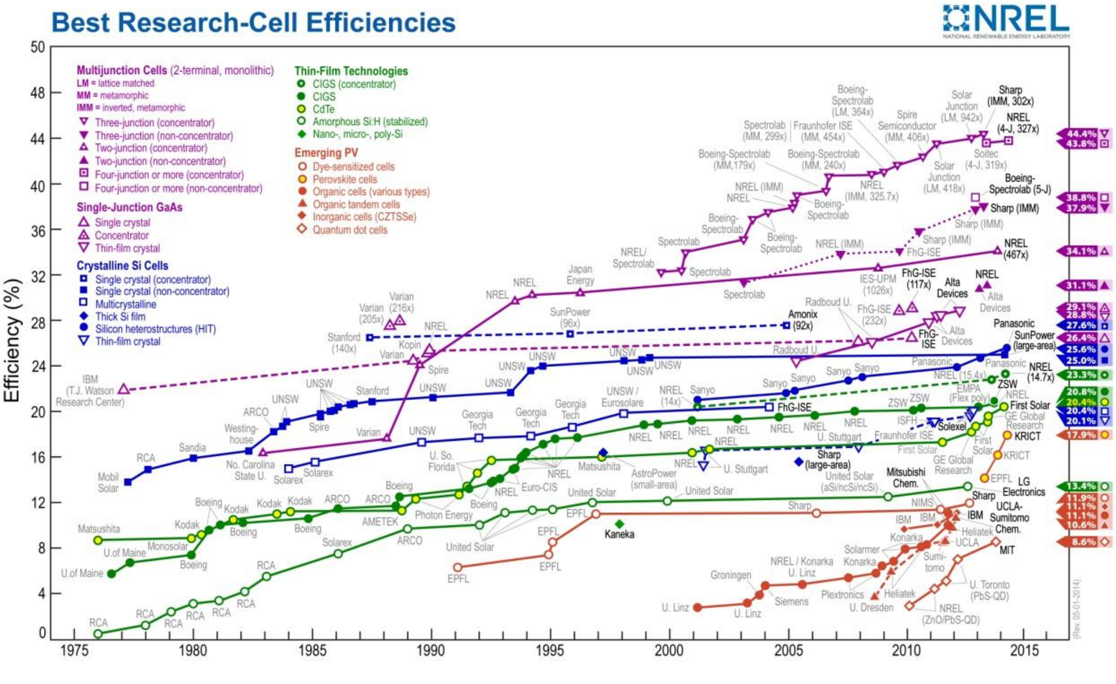

Figure 1.1 Evolution of solar cells' power conversion efficiency record for all types of photovoltaics [10]

The third-generation solar cells refer to a range of technologies, such as concentrator solar cells, tandem solar cells, dye-sensitive solar cells, organic solar cells, and quantum dots solar cells. There are also some other new-concept solar cells, for example, perovskite solar cells and CZTSSe cells. The goal of development here is to improve efficiency, to reduce production cost and to develop non-conventional products offering market diversity. Due to various reasons such as low efficiency, short lifetime and high production cost, most third-generation solar cells are still limited in the laboratory stage.

1.2.2. Development of organic solar cells

Among the third-generation solar cells, there has been intensive interest on the development of organic solar cells. Compared to inorganic solar cells, they can enable low-cost manufacture such as roll-to-roll printing and large-scale applications.

The organic solar cells are typically made from conducting and semiconducting organic materials including polymers and small molecules. The first highly conductive organic polymer, doped polyethylene, was discovered and developed by Hideki Shirakawa, Alan Heeger, and Alan MacDiarmid in 1977 for which they won the Nobel Prize in Chemistry in 2000 [11]. In 1986 C. Tang successfully made the first working heterojunction organic solar cell from copper phthalocyanine (CuPc) and a perylene tetracarboxylic derivative [12]. The device showed an efficiency of about 1% with bi-layer architecture. Then Sariciftci [13] reported the first polymer/buckminsterfullerene (C60) heterojunction device in 1993. In 1994, Yu [14] made the first polymer bulk heterojunction solar cell with poly[2-methoxy-5-(2-ethylhexyloxy)-1,4-phenylenevinylene] (MEH-PPV) and C60. In such a cell an acceptor (C60) and a donor (MEH-PPV) component were mixed and processed simultaneously to act as the active film. After this work, the bulk heterojunction configuration became an important device configuration in this research. Organic solar cells developed very rapidly during the last decade (Figure 1.2). Up to date, a laboratory efficiency record of 11.1% has been achieved by Mitsubishi Chem. (Figure 1.1 & Figure 1.2). However, compared to other technologies, the relatively low efficiency of organic solar cells, together with their short lifetime, limit their large-scale commercialization.

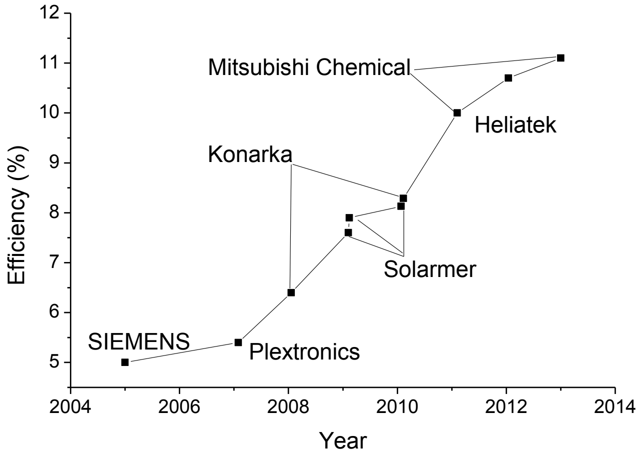

Figure 1.2 Evolution of power conversion efficiency of organic solar cells in the last decade

1.3. Basic knowledge of organic solar cells

To better understand the operational mechanism of organic solar cells, the basic knowledge of organic chemistry and organic solar cells (OSCs) is introduced in this section.

1.3.1. Organic semiconductors and their applications in solar cells

Conjugated semiconducting polymers are long-chain carbon-based large molecules. Some of them show good electrical and optical properties and have many applications in electronic and optoelectronic devices.

In 1958, Giulio Natta first synthesized the linear polyethylene, but the conductivity of this crystalline polyethylene was very low. Until 1977, the conductivity of polyethylene was improved remarkably by doping halogen elements [15]. It has been reported that the conductivity can be enhanced to be close to 560 $\Omega^{-1}\cdot cm^{-1}$ when the polyethylene film is doped with halogen or arsenic pentafluoride ions [16]. Later in 1982, Weinberger *et al.* [17] investigated polyethylene as an active material in organic solar cells. The initial device performance was poor. Then different polythiophenes [18], poly(p-phenylene vinylene) (PPV) [19] and PPV derivatives (e.g., MEH-PPV (Figure 1. 3) [14]) were introduced into organic PV field. The highly regioregular poly(3-hexylthiophene) (P3HT) (Figure 1. 3) came to become the material of choice starting from 1990s. Since then extensive studies have been carried out on P3HT-based solar cells. Recently, low bandgap polymers, such as Poly[2,6-(4,4-bis-(2-ethylhexyl)-4H-cyclopenta [2,1-b;3,4-b′]dithiophene)-alt-4,7(2,1,3-benzothiadiazole)] (PCPDTBT, E_g = 1.46 eV) and Poly({4,8-bis[(2-ethylhexyl)oxy]benzo[1,2-b:4,5-b′]dithiophene-2,6-diyl}{3-fluoro-2-[(2-ethylhexyl)carbonyl]thieno[3,4-b]thiophenediyl}) (PTB7, E_g = ~ 1.8 eV) (Figure 1. 3), are intensively investigated as active materials in organic solar cells due to their ability to harvest more photons from the solar spectrum.

1.3.2. The electronic structure of conjugated polymers

Conjugated polymers have long chains consisting of carbon atoms. These carbon atoms form alternating single (σ) and double bonds (π). Following the law of linear combination of atomic orbitals and the hybrid orbital theory, due to this conjugated structure, the electrons in double bonds can delocalize over several backbone carbon atoms and form a delocalized π electron system which gives the polymer semiconducting properties.

Figure 1. 4 illustrates the structure, electron cloud distribution and bonding π orbital/anti-bonding π* orbital of ethylene. This is the simplest conjugated molecule. The carbon atom has an electronic configuration of $1s^2 2s^2 2p^2$. When forming bonds with other atoms, the $1s^2$ electrons do not participate in bonding since these electrons are strongly bounded to the nucleus. For the $2s^2$ and $2p^2$ orbitals, in the case of ethylene, each carbon atom makes covalent σ bonds with two hydrogen atoms, a single and double bond with the other carbon atom. To achieve this goal, the 2s and the in-plane $2p_x$ and $2p_y$ orbitals overlap with the adjacent carbon atom to form three degenerate sp^2 hybridized orbitals (termed sp^2 orbitals). These hybridized orbitals form three in-plane σ bonds with the other atoms. These hybridized orbitals form three in-plane σ bonds with the other atoms. These single bonds are strong and rigid. The electrons are localized over the two bonded atoms and they are associated with a large bonding energy.

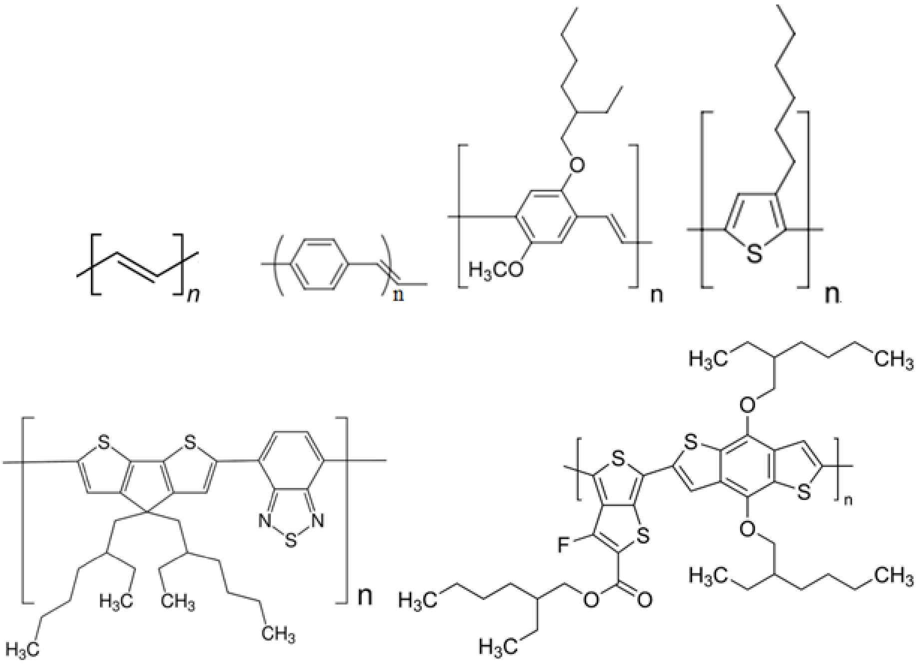

Figure 1. 3 Some conjugated polymers investigated in PV cells. Top: Polyethylene, poly(p-phenylene vinylene) (PPV), poly(2-methoxy-5-(20-ethyl- hexyloxy)-1,4-phenylvinylene) (MEH-PPV), poly(3-hexylthiophene) (P3HT). Bottom: PCPDTBT, PTB7.

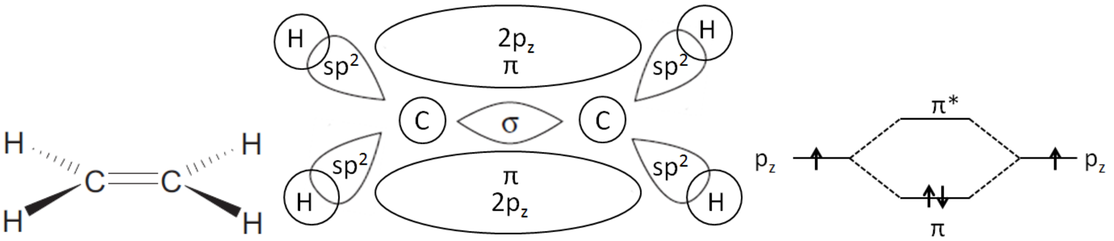

Figure 1. 4 Structure, electron cloud distribution, bonding π orbital to the anti-bonding π* orbital of ethylene

The remaining $2p_z$ orbitals of each carbon atom are extended out of the plane of sp^2 orbitals and these p_z orbitals interact with each other producing a π bond. Electrons forming such double bonds are delocalized with distribution located above and below the plane of the single bonds. The π bond lowers its bonding energy through splitting bond into two molecular orbitals (the bonding π orbital and the anti-bonding π* orbital, Figure 1. 4). In the ground state, both electrons of the π bond lie in the bonding orbital since this orbital has lowest energy. The highest energy level occupied by electrons is bonding π orbital and referred to as the highest-occupied molecular orbital (HOMO). Similarly, the anti-bonding π* orbital is termed as the lowest unoccupied orbital (LUMO).

In the case of ethylene, each carbon atom donates one electron to the π system. When the conjugation length increases, more and more electrons and orbitals participate in bonding. The π molecular orbitals are delocalized over a longer and longer distance as the molecule gets larger. In the meanwhile, the gap between the HOMO and LUMO gets smaller and smaller. The evolution of π molecular orbitals in conjugated polymers with increasing conjugation length is shown in Figure 1. 5.

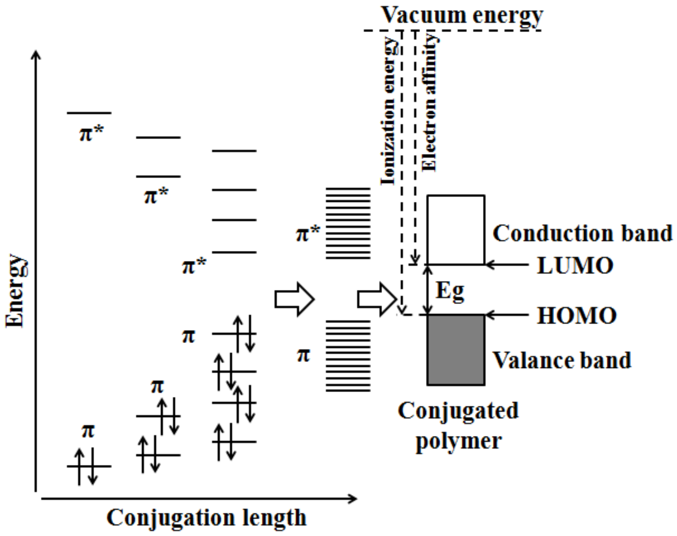

Figure 1. 5 Evolution of π molecular orbitals in conjugated polymers with increasing conjugation length

Theoretically, Hückel theory [20] predicts a continuous ladder of electronic states in an infinitely long conjugated polymer. But in practice, this continuous ladder splits into two bands associated with a lattice deformation to lower the total energy of the system, resulting in a gap opening up at the Fermi level. Hence, the highest-occupied molecular orbital of the lower band is the HOMO, the lowest unoccupied orbital is the LUMO and the energy difference between HOMO and LUMO is the bandgap (Figure 1. 5). Typically, the bandgap is in the order of 2 ~ 3 eV, e.g., ~ 2.1 eV for P3HT, or even smaller for low bandgap conjugated polymer, e.g., ~ 1.8 eV for PTB7 [21].

In fact, conjugated polymer backbones may consist of atoms of some other elements or fused rings, e.g., sulfur atoms, as shown in Figure 1. 3. This replacement can affect the electronic structures [22] of the polymers and thus their properties. In the meanwhile, the side-chains can alter the crystallinity, solubility and also the electronic structure of the polymers [23,24]. The hetero-atom together with the side-chains allow a great tunability of polymer properties.

1.3.3. Excitons and polarons in organic semiconductors

An exciton is a quasiparticle formed by an electron and an electron hole which are attracted to each other by electrostatic Coulomb force. It exists extensively in insulators, semiconductors and in some liquids.

An exciton can be formed by photo-induced excitation in semiconductors, which excites an electron to conduction band from valence band. In semiconductors with large dielectric constants and small energy gaps, the electric field screening tends to reduce the coulomb attraction force between electrons and holes. This screened Coulomb interaction together with the small effective mass of electron, the binding energy of excitons is typically small and on the scale of 0.01 eV. Thus the excitons can extend over many molecular units [25]. This type of excitons are termed as Wannier-Mott exciton [26]. Whereas in organic semiconductors, the dielectric constants are relatively lower (~ 3 to 4) as compared to their inorganic counterparts, leading to a larger screening length and thus a larger binding energy. The binding energy of excitons is typically in the order of 0.4 ~ 0.5 eV [27], with a variation range from 0.1 eV to > 1 eV [28,29]. In this case, the term Frenkel exciton is applied [26]. Since the high binding energy, the Frenkel excitons usually reside on one molecule. Moreover, Frenkel excitons in organic semiconductors have a relatively short lifetime in the scale of nanoseconds and a short diffusion length (typically ~ 10 nm) [30,31]. If not dissociated, the excitons can relax to ground state by photon or phonon emission.

There are two kinds of excitons in organic semiconductors: singlet and triplet excitons. Singlet excitons have total spin $S = 0$. They are generated directly from photon absorption with spin conservation as they are in ground state. The triplet excitons have total spin $S = 1$ with three possible linear combinations of wavefunctions. They normally cannot be gained from direct photon absorption but can be converted from singlet by intersystem crossing (time scale ~ 10 ps) (Figure 1. 10). The triplet excitons have lower energy than singlet due to their larger electron-hole spatial overlap [32].

If the excitons are separated, for instance, by an energetic driving force originated from the difference in the electronic levels of the donor and acceptor materials in organic solar cells [33,34], a positive (hole) and a negative (electron) charge are generated. The presence of a hole or electron charge in organic semiconductors will lead to a local distortion of polymer chains; the coupling of charge and the induced structural relaxation is termed polarons. The presence of polarons creates two new states in the bandgap (since the lattice relaxation lowers the total energy) and thus introduces new absorption transitions (Figure 1. 6).

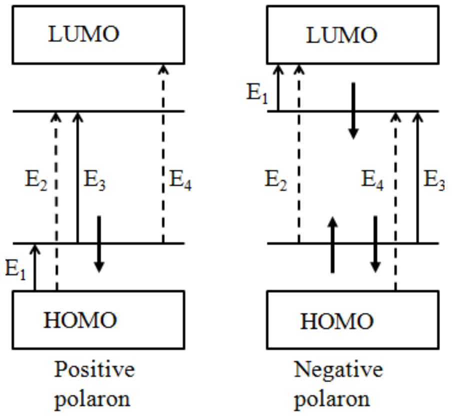

Figure 1. 6 Polaronic (positive and negative polaron) and excitonic (exciton) energy levels and the associated sub-bandgap transitions. Transitions (E_2 & E_4) in dash-line are symmetrically disallowed.

1.3.4. Photo-conversion process

The complete photo-conversion process consists of six steps in organic solar cells. In bulk heterojunction organic solar cells these steps include: (i) absorption of photons, (ii) generation of excitons, (iii) diffusion of excitons, (iv) dissociation of excitons at the donor/acceptor interface, (v) charge transport to electrodes (holes to anode and electrons to cathode) and (vi) charge collection at the electrodes. These six steps are shown in Figure 1. 8. More details about the concept of bulk heterojunction organic solar cells will be given in Section 1.3.5 and 1.4.

1.3.4.1. Absorption of photons and generation of excitons

When sunlight reaches the earth, part of it is scattered by molecules, aerosols and dust particles in the atmosphere; other part of it is absorbed by different gases in the atmosphere, such as oxygen, O_3, H_2O, CO_2. Hence, the intensity and spectrum of sunlight that reaches the Earth’s surface significantly depend on the length of the light path through the Earth’s atmosphere, whereas this length varies during the day time and also depends on latitude and time of year. In practice, the term Air Mass (AM), ratio of any actual sunlight path length to the minimum value (when the sun is directly overhead, *i.e.* at the zenith), is usually used to help characterize the spectral content and intensity of solar radiation after traveling through the Earth's atmosphere. The AM value is given by Equation 1. 1 [35]:

$$\mathrm{AM} = \frac{1}{\cos\theta} \qquad \text{Equation 1. 1}$$

Where θ is the angle of incident ($\theta = 0$ when the sun is directly overhead) (Figure 1. 7).

Hence, just outside the earth's atmosphere, the solar energy intensity is about 1353 W/m^2 [35], and the spectral distribution is referred to as Air Mass zero (AM 0) radiation spectrum. An AM 1.5 ($\theta = 48.2$ °[36]) which has an intensity of 1000 W/m^2 is usually used as standard spectrum to characterize the photovoltaics. The AM 0 and AM 1.5 spectra are shown in Figure 1. 9.

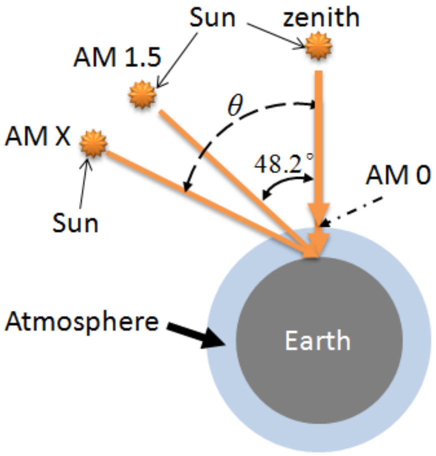

Figure 1. 7 Illustration of AM 0, AM 1.5 and AM X. Note that at the zenith, the sun is directly overhead and $\theta = 0$; AM 0 is the solar spectrum just above the atmosphere at $\theta = 0$; AM 1.5 is the solar spectrum with an incident angle of 48.2 °from the zenith; $X = 1/\cos\theta$.

When sunlight reaches the Earth's surface and strikes a solar cell, part of it will be scattered, reflected, and absorbed by the encapsulation materials and electrodes. Part of the remaining light, successfully reaching the active layer, will be absorbed by the active layer.

The efficiency of photon absorption depends on the thickness and absorption coefficient of the active materials. The absorption coefficient is determined by the components of the active layer. For poly(3-hexylthiophene) (P3HT) with a bandgap of about 2.1 eV, its absorption can cover the visible spectrum up to 660 nm (Figure 1. 9). Considering the absorption coefficient of a layer composing of a blend of P3HT and [6,6]-phenyl-C61-butyric acid methyl ester (PCBM) to be about 10^5 cm^{-1}, ~300 nm thick layers absorb most of the light [37], which is much thinner than silicon solar cells. But due to their modest charge transport properties (e.g., short exciton diffusion length ~ 4 nm to 10 nm [38]), the optimal thickness of active layer for P3HT:PCBM blend is between 100 nm and 200 nm [38–40]. Developing new active materials such as low bandgap polymers (e.g., PTB7) is currently a promising approach to improve light absorption efficiency in organic solar cells.

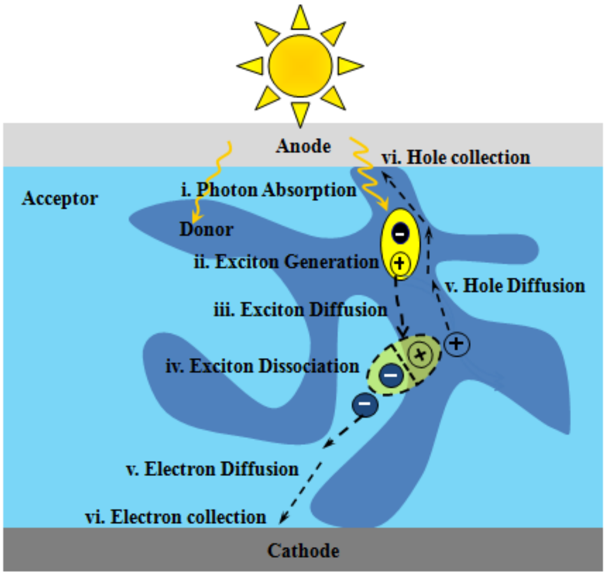

Figure 1. 8 The six steps of photo-conversion process in bulk heterojunction cells

When a photon is absorbed, it will promote an electron from the ground state S_0 into higher lying unoccupied levels, such as S_1 and $S_{n>1}$, creating a singlet exciton. The singlet excitons in higher levels ($S_{n>1}$) then relax back to S_1 through internal conversion by phonon emission. The excitons in S_1 can also relax to the ground S_0 state either by radiative (via photon emission and this phenomenon is termed fluorescence) or non-radiative (such as via phonon emission) recombination (Figure 1. 10).

Singlet excitons may convert to triplet excitons through intersystem crossing. Triplet excitons are most likely to relax to ground state through phonon emission. Triplet excitons can also decay to ground state radiatively but with a much longer lifetime (μs - ms) than singlet recombination. This triplet radiative process leads to photon emission termed phosphorescence.

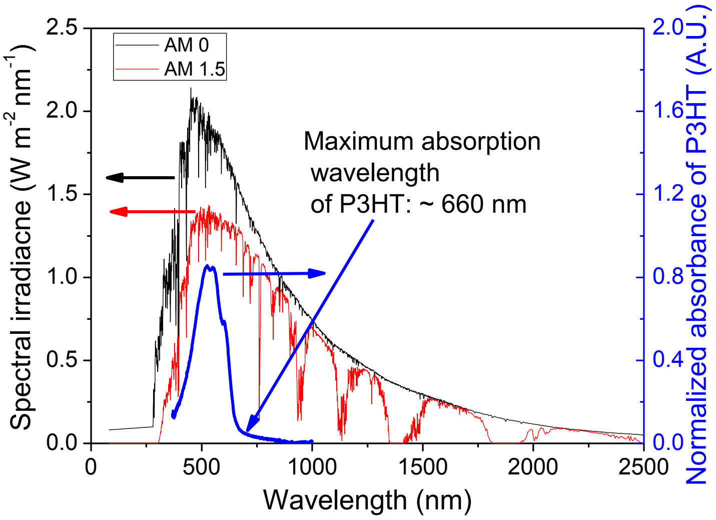

Figure 1. 9 AM 0 and AM 1.5 solar spectra [41] and absorbance of P3HT

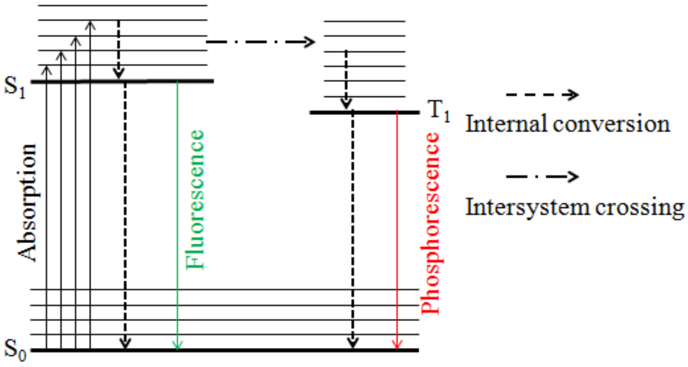

Figure 1. 10 Jablonski diagram of light absorption process in conjugated polymers

1.3.4.2. *Diffusion of excitons*

As shown in Figure 1. 11, we use Förster and Dexter mechanisms to interpret the exciton diffusion process, respectively [40,42]. According the Förster mechanism, it involves the long-range electrostatic coupling between the excitation transition dipoles located at the initial and final sites. In the case of triplet excitons, they diffuse following a short-range exchange (Dexter-type) mechanism relying on the orbital overlap between adjacent sites. As a result, singlet excitons diffuse more rapidly than triplets. But as mentioned in Section 1.3.3, the lifetime of singlet excitons is on the scale of nanosecond, while triplet excitons have a rather longer lifetime (μs - ms). The actual diffusion efficiency of singlets and triplets to the Donor/Acceptor (D/A) interface depends on the actual device system [40].

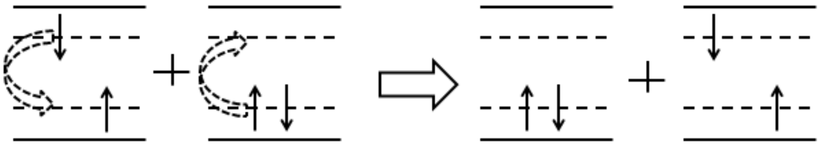

Förster mechanism for singlet exciton (long-range electrostatic coupling ~ 30-100 Å)

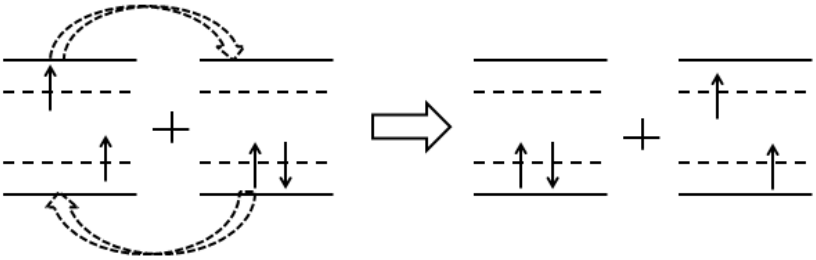

Dexter mechanism for triplet excitons (short-range exchange ~ 6-20 Å)

Figure 1. 11 Förster and Dexter diffusion mechnaisms for singlet and triplet excitons, respectively (Adopted from [42])

1.3.4.3. Dissociation of excitons

When the excitons reach the donor/acceptor (D/A) interface, if they do not recombine, they may be separated at this interface by an energetic driving force originated from the difference in the electronic levels of the donor and acceptor materials [33,34]. An exciton is a quasi-particle formed by a Coulomb-bound electron-hole pair which is initially located on one molecule. The dissociation of excitons at the D/A interface are generally considered to involve two steps [40,43–45] (Figure 1. 12). First, the exciton dissociates into a charge transfer (CT) state (D^+/A^-). In this state, the hole sits in the donor molecule and electron travels to the acceptor molecule by hopping. The next step is that the CT exciton separates into charge-separated (CS) states and finally free charge carriers. The final energy of CS state, $E_{\mathrm{final}} = I_D + E_A$ (I_D is the ionization potential of donor, E_A is the electron affinity of the acceptor and E_{final} is the energy level of completely unbound hole-electron pair (Figure 1. 12)) can be approximately estimated from the energy difference between the LUMO of the acceptor and HOMO of donor [40]. That is to say, the dissociation occurs when the energy of exciton (energy difference of donor LUMO and donor HOMO) is larger than E_{final} [45]. CT excitons could recombine to the ground state, termed geminate recombination. The recombination of CS carriers is termed non-geminate recombination [46].

The mechanism of CT excitons is still under debate. A new excitation mechanism of CT excitons was proposed recently [44,47]. According to this new mechanism an excited CT exciton (also named hot CT excitons, with excess energy than the CT exciton lying in the lowest CT state) could be directly formed by photon absorption (Figure 1. 13).

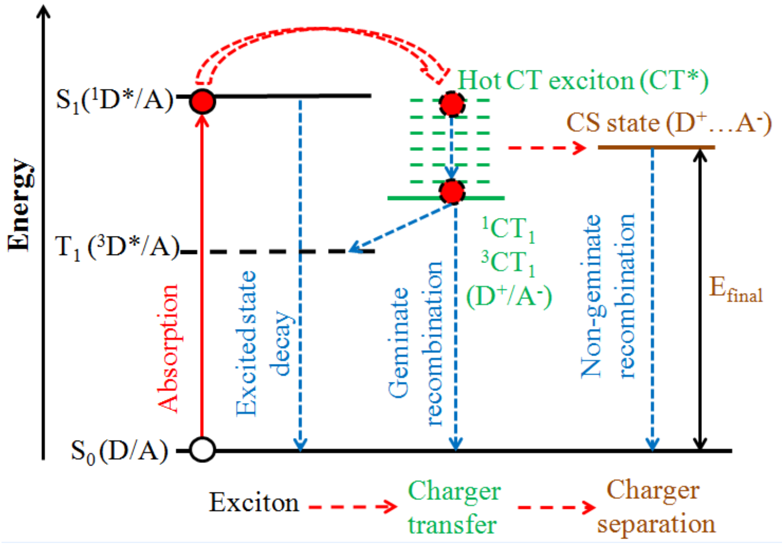

Figure 1. 12 Schematic Jablonski diagram describing the photo-induced charge-carrier formation mechanism in an organic solar cell: S_0 is the singlet ground state of the donor or the acceptor, S_1 and T_1 the first singlet and triplet excited state, respectively; the left superior 1 and 3 denotes the singlet and triplet excitons; symbol * denotes the excited state; + and – represent the positive and negative charge, respectively.(Adopted from reference [40])

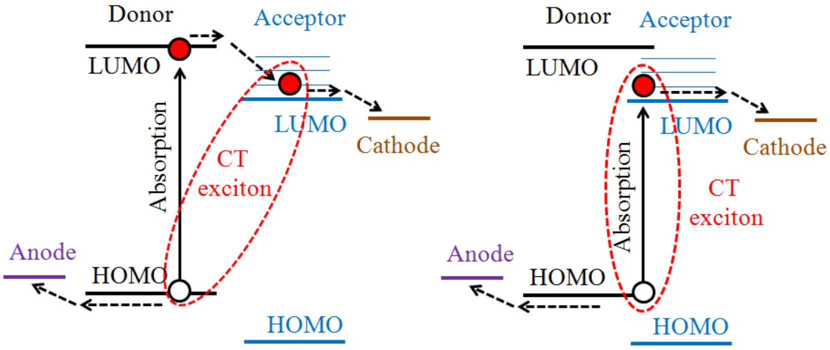

Figure 1. 13 Charge generation process in organic solar cells. Left: indirect formation of CT exciton; right: direct formation of CT exciton by photon absorption (Adopted from reference [44])

1.3.4.4. Transport of charge carriers

Once excitons are separated into free charge carriers, electrons will transport to cathode and holes to anode. Otherwise, non-geminate recombination will occur. Various recombination processes are involved during charge transport: (1) radiative recombination by photon emission; (2) non-radiative recombination by phonon emission; (3) recombination at the sub-bandgap trap states induced by the impurities or defects in the material (Shockley-Read-Hall recombination) [42].

If charges do not recombine, they will travel in the form of polarons (Section 1.3.3) in conjugated organic materials. Polarons moves intra- or inter-molecular by hopping. Compared to the high mobility (on the scale of 10^2 - 10^3 cm^2 V^{-1} s^{-1}) in inorganic semiconductors, the mobilities in organic semiconductors are quite low (typically, 10^{-6}-10^{-3} $cm^2 V^{-1} s^{-1}$) [40,48]. This modest mobility is owing to the weak electronic couplings, large electron-vibration couplings and disorder packing in polymers. As a result, the polymer morphology and crystallinity affect the transport mobilities significantly [40,48]. If the polymer is well crystallized, the mobility can reach over 1 $cm^2 V^{-1} s^{-1}$ [40,48].

1.3.4.5. *Extraction of charges*

Once arriving at the electrodes, polarons may be extracted into the external circuit. Metal conductors form two kinds of contacts with semiconductors: ohmic or Schottky contact, determined by the work function of the metal Φ_M, work function (Φ_{SC}) and electronic affinity (χ_{SC}) of the semiconductors [49]. Here, the work function Φ_M is the minimum energy needed to remove an electron to vacuum from the Fermi level of the metal; Φ_{SC} is the minimum energy needed to remove an electron to vacuum from the Fermi level of the semiconductor; the electronic affinity χ_{SC} is the energy required to promote an electron to the vacuum energy level from the bottom of the conduction band. The formation conditions of these two contacts are shown in Figure 1. 14.

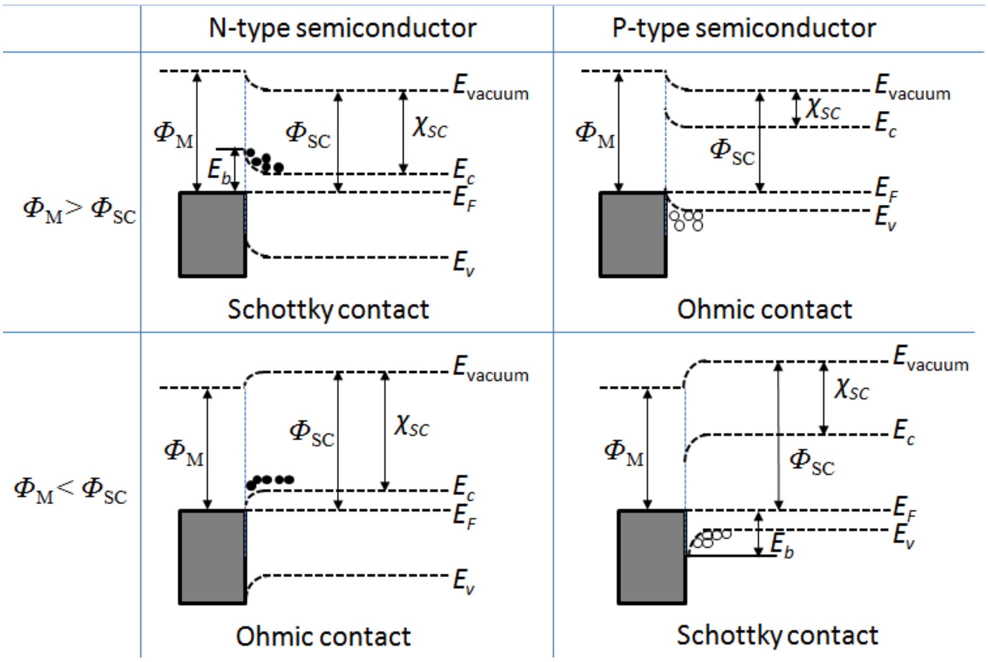

Figure 1. 14 Schematic of metal-semiconductor contacts. Note that the black dots at the metal-semiconductor interface represent electrons and circles represent holes; E_v is the energy level of the top of the valance band and E_c is the energy level of the bottom of the conduction band; E_{vacuum} is the energy level of vacuum while E_F is the Fermi level.

In ohmic contact, there is no potential barrier for charges to travel across the contact; while for Schottky contact, there is a potential barrier E_b (given by Equation 1. 2) at the interface (Figure 1. 14):

$$E_b = \Phi_M - \chi_{SC} \qquad \text{Equation 1. 2}$$

If highly doped, the semiconductors will have a narrow space-charge region width and a narrow Schottky barrier E_b. When the barrier is sufficiently narrow, the electrons can tunnel from the metal to the semiconductor and from the semiconductor to the metal [50]. In this case, the Schottky contact becomes ohmic due to tunneling.

In the organic semiconductors, the metal-semiconductor contact is complex due to factors such as interfacial charge-density redistributions, geometry modifications, and/or chemical reactions occur at the interface. These factors significantly affect the charge collection efficiency [40,51].

1.3.5. Architectures of organic solar cells

1.3.5.1. General architecture of organic solar cells

In general, the organic solar cells are composed of several thin layers (Figure 1. 15).

- The substrate can be typically a thin glass or a flexible and transparent substrate such as Polyethylene terephthalate (PET).
- The anode should be transparent since it locates before the active layer. Typically it is indium tin oxide (ITO) or fluorine doped tin oxide (FTO). ITO has bandgap of 3.7 eV, thus most photons can travel through it. For visible light the transmittance of commercial ITO is higher than 80% [52]. The back electrode does not need to be transparent and is typically a layer of aluminum or silver or gold.
- Generally speaking, a hole extraction layer (HEL) is inserted between the anode and the active layer. This layer is also thin and highly transparent. It typically has a work function very close to the ionization potential of the donor component in the active layer to facilitate hole extraction. The most common material for HEL is Poly(3,4-ethylenedioxythiophene):Polystyrene sulfonate (PEDOT:PSS). Similarly, there is an electron extraction layer (EEL) inserted between the active layer and cathode. Calcium and lithium fluoride are frequently used for this layer.
- The active layer is deposited onto the HEL layer. It is the layer responsible to absorb photons and it is the main part of the solar cell. It normally consists of a donor material and an acceptor material.

Depending on the variations within the active layer, there are four common architectures which will be described below.

1.3.5.2. Single layer cells

The active layer consists of just one semiconductor material. This layer forms a Schottky contact with an electrode. Due to the energy band bending of the Schottky contact excitons generated in the active layer will be spitted into electrons and holes and transported to the corresponding contact electrode. The drawback in such device structure lies in the serious charge recombination during transport.

1.3.5.3. Planar heterojunction cells

This structure is typically composed of two layers: one from the donor material and the other from the acceptor material. The excitons are transported to the donor/acceptor interface and then dissociated there. Solar cells with this device structure is limited by the small D/A interface since only a limited portion of excitons can reach the D/A interface and dissociate there.

1.3.5.4. Bulk heterojunction cells

In this structure, the donor and acceptor materials are well mixed in solution first. They are then deposited onto a substrate resulting in the formation of a number of small domains allowing a large interfacial area (Figure 1. 8). Due to the enlarged interfacial area, more excitons can reach the donor/acceptor (D/A) interface in organic solar cells. The morphology of active layer therefore affects the charge separation significantly. We used this architecture in this thesis and more details will give in the following Section 1.4.

1.3.5.5. Tandem solar cells

Because most organic materials have a limited absorption window, tandem architecture is introduced to combine solar cells based on different active materials to boost photon harvest efficiency. In such device structure two or more organic solar cells are deposited on each other to form a system in series. The component cells have different absorption window and the combination of them can thus achieve higher photon absorption efficiency. The short circuit current in a tandem cell is limited by the cell which has the lower/lowest short circuit current.

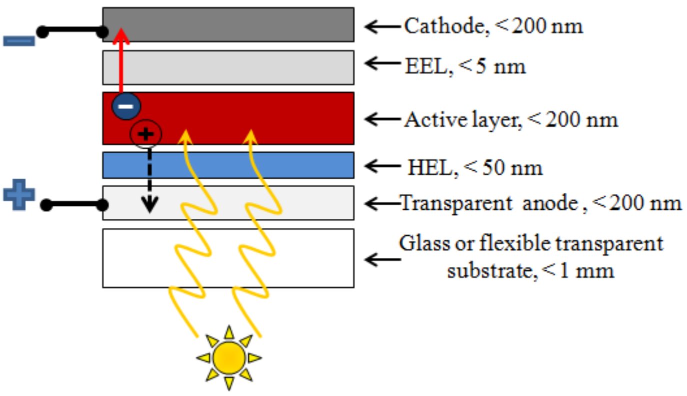

Figure 1. 15 General architecture of organic solar cell: HEL denotes the hole extraction layer, and EEL the electron extraction layer.

In addition, some new architectures for organic solar cells are currently being developed based on the above-mentioned four device structures. Examples of these structures include optical fiber based architecture and folded reflective architecture [30].

1.4. Organic bulk heterojunction solar cells using polymers and small molecules

The organic bulk heterojunction solar cells (OSCs) using PEDOT:PSS as anodic buffer layer are used in this thesis. Thus the PEDOT:PSS and the photoactive layer for OSCs are introduced in this section.

1.4.1. Hole extraction layer: PEDOT:PSS

The poly(3,4-ethylenedioxythiophene) (PEDOT) is an intrinsically conducting polymer built from 3,4-ethylenedioxythiophene (EDOT) monomers. PEDOT is insoluble in many common solvents and unstable in air in its neutral state. These disadvantages limit its industrial applications. Fortunately, these problems can be solved by incorporating oxidant sodium peroxodisulfate ($Na_2S_2O_8$) and modifiable proportion of poly(styrene sulfonic acid) (PSS) into the solution and resulting in an aqueous dispersion of PEDOT:PSS. In such solution PEDOT is in an oxidized state (Figure 1. 16) and it shows high stability when oxidized [53,54]. PSS is water soluble and acts as a template polymer in the dispersion and thus forms a PEDOT-PSS complex. It has two functions in the complex: (1) PSS acts as a charge balancing dopant which supplies counter ions and thus, accompanied with sodium peroxodisulfate ($Na_2S_2O_8$), keeps the PEDOT in an oxidized state [55]; (2) PSS can make the PEDOT segments (oligomers with about 6 to 18 repeating units) forming PEDOT-PSS complex and thus keep them dispersed in the aqueous solution (Figure 1. 17) [55–58]. The PEDOT to PSS ratio can affect the film conductivity significantly, and to some extent, the conductivity decreases with increasing PSS content [56].

PEDOT:PSS is commonly used as the buffer layer of anodic electrode in OSCs [59–61]. Generally speaking, the work function of PEDOT:PSS (4.7-5.4 eV [62]) is normally higher than ITO (4-5 eV [63]) and thus leading to efficient hole extraction. In addition, the spin-coated PEDOT:PSS film can smoothen the rough ITO surface and reduces the chance of short-circuits [64,65]. The PEDOT:PSS layer located between the ITO and photoactive layer may also help to prevent oxygen diffusing into the photoactive layer. The migration of oxygen will oxidize the polymer like P3HT which is believed to be one of the device performance degradation mechanisms of OSCs [66,67].

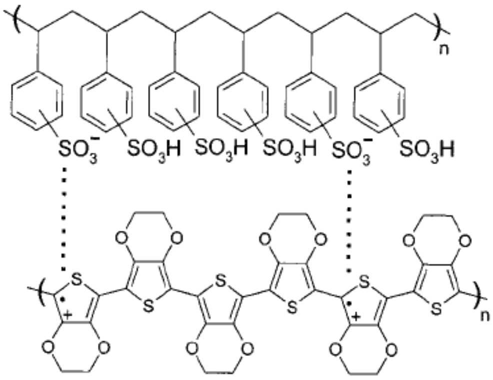

Figure 1. 16 Structures of PEDOT and PSS, adopted from reference [53]

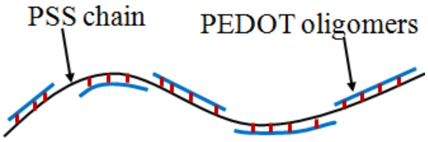

Figure 1. 17 Schematic of PEDOT:PSS complex, adopted from reference [55]

In PEDOT:PSS films, the PEDOT grains are surrounded by the excess PSS after spin-coating. Upon drying, a solid film will be obtained and the film is comprised of horizontal layers of flattened PEDOT-rich grains embedded in quasi-continuous PSS lamellas, forming a granular structure [56–58,68]. The average diameter of such grains is in the range of 20–80 nm [57,58]. The thickness of the PSS shells has been found to be about 35±5 Å [69–71]. Since PEDOT is a conducting component while PSS has only a weak conductivity, the PEDOT-rich core has a higher conductivity than the PEDOT-depleted PSS shell. Therefore, charges can transport more efficiently along the backbone in the grains than between them due to the charge transport barrier induced by the insulating PSS shell [56]. Hence in such a granular structure, the electrical conductivity is controlled by the hole transport in the PEDOT oligomers, the hopping between PEDOT oligomers and between the PEDOT-rich gains with a PSS barrier [56,58]. Consequently, the conductivity of PEDOT:PSS film is rather low. For instance, pristine Clevios™ P – Heraeus PEDOT:PSS used in this work has the maximum conductivity of ~ 1 S/cm [72].

Many techniques have been applied to enhance the conductivity of PEDOT:PSS, such as applying post-deposition thermal annealing [73,74], adding high boiling solvents (e.g., glycerol or sorbitol [75–77]), modifying synthetic conditions [78,79], improving the wetting of ITO surface (e.g., silanes [80]), adding polar solvent (e.g., dimethylsulfoxide [81]), and varying the PEDOT to PSS ratio [80,82]. In this thesis we mainly apply the thermal annealing and high boiling additives to improve the conductivity of PEDOT:PSS films.

In addition, the thickness of PEDOT:PSS used in OSCs is typically in the scale of several tens of nanometers [45,83–85]. A PEDOT:PSS layer thicker than such thickness will reduce the transmission significantly [72] despite a decreased sheet resistance decreases [86].

1.4.2. Bulk heterojunction

As mentioned in Section 1.3.1, various organic polymers and small molecules have been investigated for their application in organic solar cells. In particular, the conjugated polymer poly(3-hexylthiophene-2,5-diyl) (P3HT) and the small molecule derivatives of fullerene, [6,6]-Phenyl C61 butyric acid methyl ester (PCBM), form one of the most popular organic solar cell active layer components. Here, P3HT is used as a donor material while the PCBM are as the acceptor materials. During the device fabrication process, P3HT and PCBM are dissolved in an organic solvent, such as chlorobenzene and di-chlorobenzene. They blend of them is deposited as the active layer with a controlled morphology, in order to reach the highest device performance.

1.4.2.1. Donor material: P3HT

The polythiophene is a conjugated polymer made of thiophene monomers. P3HT is one derivative of polythiophene and it has hexyl groups attached at the position No. 3 of polythiophene (Figure 1. 18).

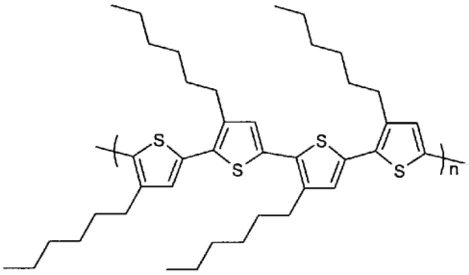

Figure 1. 18 Chemical structures of poly(3-hexylthiophene-2,5-diyl)

1.4.2.1.1. Regioregularity

When polymerizing 3-hexylthiophene monomers to synthesize P3HT, there are three possible asymmetric couplings, they are (Figure 1. 19):

1) 2, 5', or head-tail (HT) coupling.
2) 2, 2', or head-head (HH) coupling.
3) 5, 5', or tail-tail (TT) coupling.

As a result, the term regioregularity is used to describing repetition degree of couplings in a polymer. For example, 98% head-tail regioregular P3HT means that the ratio between the number of HT coupling and the sum of all these three types of couplings is 98%.

It is reported that regiorandom P3HT has low charge mobility due to the random sequence of HT, HH and TT building blocks and the resultant poor intermolecular orbital overlap [87–89]. Highly regioregular P3HT has a highly planar conformation [90] which favors a close intermolecular π-stacking in lamella fashion (Figure 1. 20) [89,91–94] and improves the charge mobility. It has been reported that, with a lamella packing, the mobility of P3HT can reach as high as 0.1 cm^{2} V^{-1} s^{-1} [91,95,96].

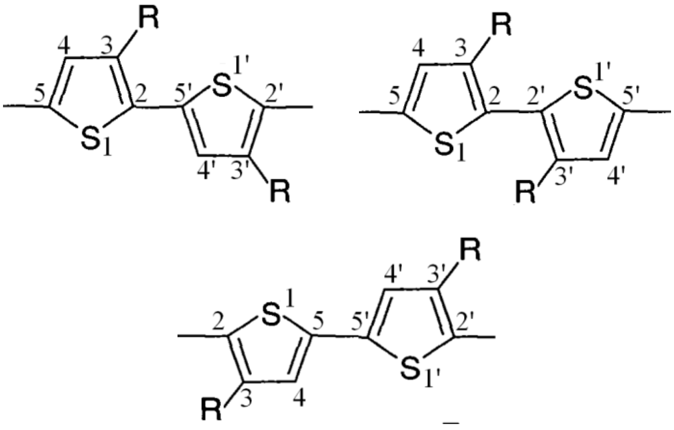

Figure 1. 19 Possible couplings of two 3-hexylthiophene monomers for P3HT

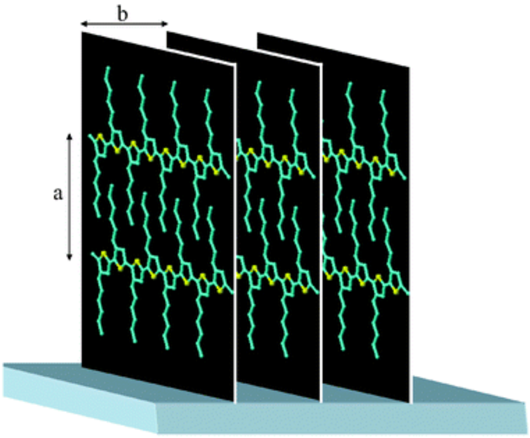

Figure 1. 20 Intermolecular interactions of side-chains of lamellar structures of regioregular P3HT: a and b are the lattice constants and a-axis is perpendicular to substrate while b-axis parallel to substrate (Reprinted from reference [93])

1.4.2.1.2. Molecular weight

The molecular weight of P3HT also plays an important role in the morphology of the active layer. Molecules with long chains do not tend to form highly packed stacking while shorter chains are much easier to self-assemble into crystalline fibrous domains [96]. However, the mobility of relatively high molecular weight molecules is higher than expected; conversely the film made of low molecular weight molecules has a low mobility. This is due to the existence of abundant grain boundaries formed between crystalline fibers assembled by short chains. Such boundaries form more transport barriers and charge traps which are disadvantageous for charge transport (Figure 1. 21 (a) and (c)). While the gain boundaries of polymer films with a larger molecular weight are typically smoother with domains tightly connected to each other. This explains why in some case charge transport can be facilitated throughout a larger area despite an overall lower crystallinity (Figure 1. 21 (b) and (d)) [96,97].

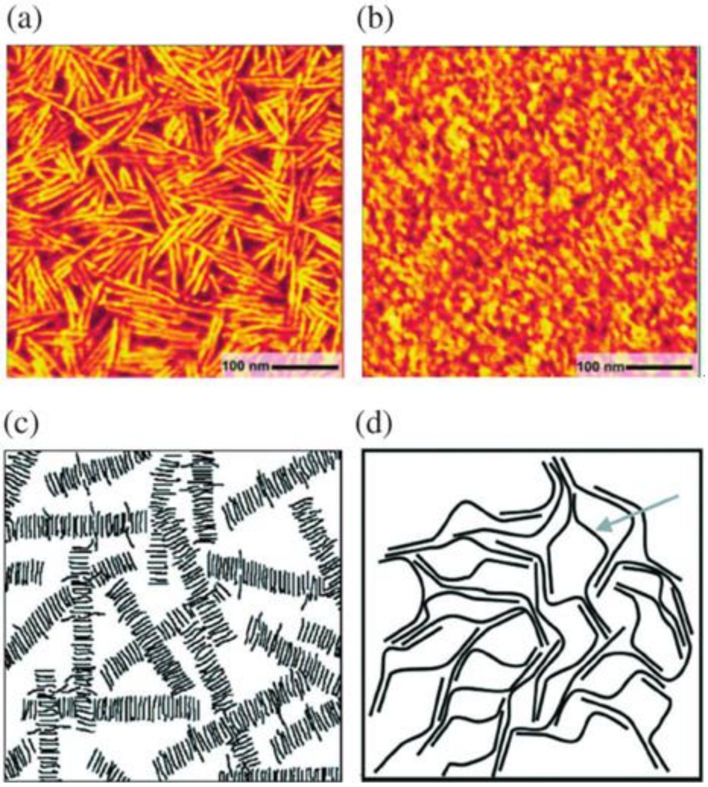

Figure 1. 21 AFM images of (a) crystalline rod-like morphology of low Mn P3HT (3.2 kDa) and (b) nodule structure for high Mn P3HT film (31 kDa). (c) schematic of badly connected rod-like crystalline for low Mn P3HT and (d) increased networking between crystalline domains for high Mn P3HT film (reprinted from [96] with permission of The Royal Society of Chemistry)

In summary, regioregular P3HT with appropriate molecular weight represent a good donor material choice for organic solar cells due to the following properties:

- A good solubility in organic solvents such as chlorobenzene and di-chlorobenzene;
- An adequate bandgap (~ 2.1 eV) and a high absorption coefficient(10^5 cm^{-1}) allowing a relatively good match with the solar spectrum and efficient absorption within a thin film;
- The ability to form close intermolecular π-stacking by interactions of side-chains;
- A relatively high hole mobility (10^{-3} to 10^{-1} cm^2 V^{-1} s^{-1}) tunable from their morphologies.

1.4.2.2. Acceptor material: PCBM

The PCBM is a type of fullerene (C60) derivatives. It has a high election affinity and thus commonly used as an acceptor material in organic solar cells. C60 is a rather insoluble material [3] but it can become soluble after chemical modifications. For example, its derivative [6,6]-Phenyl C61 butyric acid methyl ester ($PC_{60}BM$) (Figure 1. 22) has a high solubility in chlorobenzene and dichlorobenzene. There are also other types of PCBMs, e.g., $PC_{70}BM$ and $PC_{84}BM$ (Figure 1. 22). $PC_{70}BM$ and $PC_{84}BM$ have enhanced optical absorption abilities than $PC_{60}BM$. Such enhanced absorption can possibly improve the photovoltaic efficiency in organic solar cells [98].

The following properties of PCBMs enable them to be an ideal acceptor material to be combined with P3HT:

- Sufficient solubility in common organic solvents;
- Ultrafast electron transfer, on the scale of several hundred femto-seconds or less, has been identified from P3HT to PCBM with an efficiency approaching 100% [99,100];
- An adequate dielectric constant (~ 4.4);
- Good electron mobility ($> 10^{-3}$ cm^2 V^{-1} s^{-1});
- Isotropic electron accepting ability owing to the symmetry of fullerene;
- A LUMO level of about 3.7 ~ 4.4 eV and a HOMO level of about 6.1 eV, allowing the formation of a type-II heterojunction interface with P3HT.

1.4.2.3. P3HT:PCBM film

In the bulk heterojunction solar cells (Figure 1. 8), the donor and acceptor materials are mixed in solution and deposited on a substrate to form a thin film with many micro-domains. The properties of this active layer affect the device performance significantly. As mentioned above, well-controlled morphology of the active layer enhances both the charge mobility and exciton dissociation. In practice, the active layer morphology of active layer depends on the material molecular weight [96,97,101], regioregularity [87–89,101], the weight ratio between P3HT and PCBM [101–104], the solution concentration [101], the types of (co-) solvents used [59,101,104,105], the properties of side chains [23,24], additives [104,106], film deposition method and process [101,107], and post-deposition annealing processes involving solvent vapor [104,108] and thermal annealing [104,109,110], etc. The optimization of these factors will enhance the charge separation and transport properties and thus improving the device performance.

Besides the morphology, thickness is also an important parameter. Due to the modest transport mobility in polymer materials, the charge carrier diffusion length is typically no more than 100 ~ 200 nm. The correlation between the P3HT:PCBM thickness and the device efficiency is shown in Figure 1. 23. There are two peak values appear when the thickness of the active layer is around 100 nm and 200 nm, corresponding to optical interference effects in the thin-film stack. These two thicknesses have been confirmed by simulation and experiments [111,112].

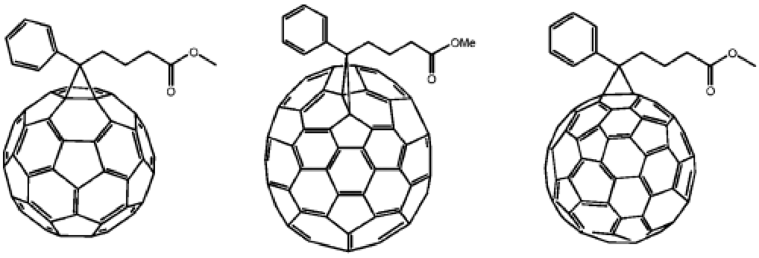

Figure 1. 22 Structures of fullerene derivatives, from left to right: $PC_{60}BM$, $PC_{70}BM$ and $PC_{84}BM$ [98,113]

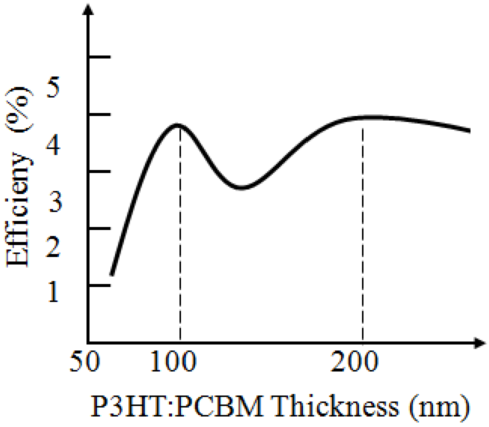

Figure 1. 23 P3HT:PCBM thickness-dependent power conversion efficiency [111,112]

1.4.3. Photovoltaic Characteristics of organic solar cells

1.4.3.1. Current-voltage response and efficiency

The common way to study the performance of a solar cell is to measure the current-voltage response (*J-V* curve) in the dark and under illumination (Figure 1. 24) (The measurement method will be introduced in Chapter II).

Solar cells behave as simple diodes in the dark. Under reverse bias, the dark current is very small and hardly measureable. Under forward bias the dark current increases rapidly following the Shockley equation if the diode is ideal. Under illumination, photocurrent is generated and its sum with the dark current leads to the *J-V* curve shifting down at all potential by the magnitude of short circuit current J_{sc}.

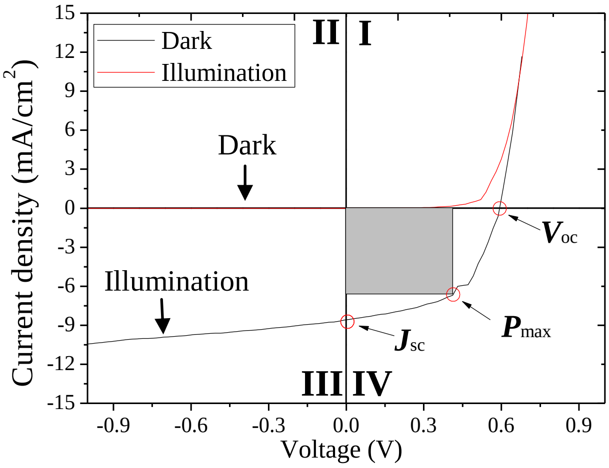

Figure 1. 24 Current versus applied voltage of a solar cell: the red curve is obtained for measurement in the dark and the black curve is the result of measurement under illumination

As shown in Figure 1. 24, in the first quadrant where V > 0 and J > 0, the devices acts as a light emitting diode since the injected current is more than photogenerated current; in the third quadrant, the device works as a photodiode; only in the fourth quadrant, the device acts as a photovoltaic device. The power conversion efficiency (*PCE*) of a solar cell is defined by Equation 1. 3:

$$PCE = \frac{J_{sc}V_{oc}FF}{P_i} \qquad \text{Equation 1. 3}$$

Where

- J_{sc} is short circuit current density (the current density in the circuit when the applied bias is zero), in the unit of mA/cm^2;
- V_{oc} is open circuit voltage (the applied bias when the current is zero in the circuit), in the unit of V;
- P_i is the incident light power, in the unit of W/m^2;
- *FF* is the fill factor (defined below in Equation 1. 4, unitless).

All these parameters are extracted under AM 1.5 simulated illumination (Figure 1. 9). *FF* is defined as the ratio between P_{max} and product of J_{sc} and V_{oc} (Equation 1. 4):

$$FF = \frac{P_{\max}}{J_{sc} \times V_{oc}} = \frac{(J \times V)_{\max}}{J_{sc} \times V_{oc}} \qquad \text{Equation 1. 4}$$

where P_{max} is maximum power that could be extracted from the solar cell, its value equals to the maximum product of current density and applied bias voltage of the solar cell (Figure 1. 9).

We often use another parameter, quantum efficiency, to estimate the spectral responsivity of a solar cell. There are external and internal quantum efficiencies.

The external quantum efficiency (*EQE*) is the ratio of the charge carriers ($\boldsymbol{N}_e(\lambda)$) collected by the solar cell to the flux of photons ($\boldsymbol{N}_{ph}(\lambda)$) of a given energy incident on the solar cell from outside. It can be calculated according to the following equation:

$$EQE(\lambda) = \frac{N_e(\lambda)}{N_{ph}(\lambda)} \qquad \text{Equation 1. 5}$$

The internal quantum efficiency (*IQE*) is defined by the ratio of the charge carriers collected by the solar cell to the number of photons of a given energy aborbed by the cell.

The *EQE* and *IQE* has the following relationship:

$$EQE(\lambda) = IQE(\lambda) \times \eta_A(\lambda) \qquad \text{Equation 1. 6}$$

where η_A is the light absorption efficiency defined by the ratio of the number of incident photons that are absorbed to the number of incident photons. The *IQE* can be used to evaluate the intrinsic quality of the device after absorption.

1.4.3.2. Performance-limiting factors

There are a number of factors significantly affecting the final performance of BHJ OSCs through influencing the J_{sc}, V_{oc} and *FF*.

1.4.3.2.1. Short circuit current

First, under the standard condition (AM 1.5 spectrum and 25 ℃), J_{sc} is related to the photon absorption, the charge mobility, and the charge separation capability of organic semiconductors, as well as the morphology of the active layer [114]:

1) For photon absorption, it depends on the bandgap of the absorbing material. Theoretical simulation results show that, the ideal bandgap to obtain the highest photon absorption efficiency is around 1.3 eV [33]. For P3HT, its bandgap is approxiamtely 2.1 eV, leading to an absorption cutoff wavelength at around 660 nm (Figure 1. 9) and a capability of absorbing about 22% of the available solar photons.

2) For the charge mobility, it mainly depends on the intrinsic properties of the semiconductor and the molecular packing, while the molecular packing is related to the material regioregularity and the molecular weight, as well as the morphology (intermolecular

π-stacking and connectivity of domains) of the active layer (Section 1.4.2). In addition, the mobility could be modified by altering the fullerene content in the blend [114].

3) The charge separation is affected by the LUMO levels offset of donor and acceptor, and similarly, the morphology of the active layer since the small domains create a large D/A interface area, and also enable to improve the possibility of excitons transport to the D/A interface.

1.4.3.2.2. Open circuit voltage

Second, regarding V_{oc}, due to the simplest Metal-Insulator-Metal (MIM) model, it is determined by the difference in the work functions of the two metal electrodes [115]. It has been reported that for many organic solar cells, the V_{oc} can be increased by utilizing electrodes with higher difference in work function [116]. For example, Frohne *et al*. [59] reported that, the electrochemical potential of the PEDOT:PSS (HEL), which is varied by altering doping level, can influence the V_{oc}. Moreover, the work function of ITO can be effectively improved by oxygen plasma treatment due to surface carbon removal, Fermi level shift, creation of surface dipoles and change in ratio of surface constituents (Sn, In, O), as well as decrease in series resistance and change of the ITO surface roughness [117,118].

In practice, in OSCs, the V_{oc} is also affected by many other paramters, such as dark current, Fermi level pinning and chemical potential gradients [119]. For example, the V_{oc} obtained from the solar cell using gold as cathode is higher than expected, which can not be explained by MIM model but Fermi level pinning [120]. Many reports have been demonstrated that the V_{oc} has a correlation with the acceptor strength of the fullerenes, while it is not sensitive to the variations of workfunction of cathode material. They assign this phenomenon to the Fermi level pinning which pins the cathode to the LUMO of acceptor in conjugated polymer fullerene solar cells [114,120–122]. The fermi level pinning is owning to surface states of the fullerenes at the fullerene/metal contact and/or formation of strong dipoles owning to partial charge transfer between the cathode and fullerene [121,123]. In addition, the fullerene content can also affect the V_{oc}. This was explained by the varying coverage area of cathode by fullerene which is related to the concentration of fullerene in the active blend [102].

Reseaschers have also investigated the correlation of the energy levels of the donor–acceptor blend and the V_{oc} and given a statistical formula for conjugated polymer-PCBM solar cells as follows [33,120,124,125]:

$$V_{oc} = \frac{1}{e}\left|E_{HOMO}^{Donor} - E_{LUMO}^{Acceptor}\right| - \mathrm{C}$$ Equation 4. 1

Where e is the elementary charge, C is the empirical voltage loss in BHJ conjugated polymer-PCBM solar cells. The typical value of C is 0.3 and normally in the range of 0.225 - 0.435 V [125]. The difference between the V_{oc} and V_{BI} (HOMO of donor minus LUMO of the acceptor) can be minimized by optimizing materials, the active-layer thickness, and the charge-carrier mobility [33]. Moreover, the charge carrier recombination also affects the V_{oc} of BHJ OSCs [126].

1.4.3.2.3. Fill factor

The *FF* depends on the transport, recombination and as well as resistance [114,116,119,127–129]. The series resistance (R_s) and shunt resistance (R_{sh}) dramtically affect the *FF* through altering J_{sc} and V_{oc}. The R_s and R_{sh} can be simply derived by taking the inverse slopes from the *J*-*V* curve obtained under illumination [130,131]:

$$R_s \approx \left[\frac{dI}{dV}\right]^{-1}_{V=V_{\mathrm{oc}},J=0}$$ Equation 1. 7

$$R_{sh} \approx \left[\frac{dI}{dV}\right]^{-1}_{V=0,J=J_{sc}}$$ Equation 1. 8

In priciple, and the R_s is related to mobilities of the layers involved in charge transport and also affected by the thickness of transport layers, as thicker layers have lower conductivities. Thus, the R_s is sensitive to the morphology, thickness and intrinsic resistance of semiconductor blend layer, and the quality of semiconductor/electrode interfaces. While R_{sh} is related to the charge recombination caused by impurities and defects in the active organic semiconductor layer [116,119]. Typically, R_{sh} ($> 10^3\ \Omega$) is much lager than R_s (on the scale of $10^0 \sim 10^1\Omega$) in OSCs.

The effects of R_s and R_{sh} on the parameters of a solar cell are shown in Figure 1. 25. As shown in the figure, high R_s can diminish the J_{sc}, whereas low R_{sh} decreases V_{oc}, both leading to a decrease in *FF* [132].

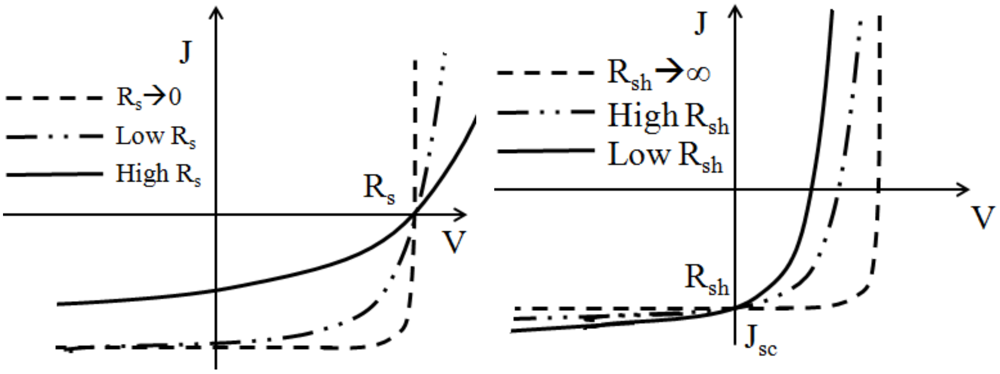

Figure 1. 25 Effects of R_s and R_{sh} on fill factor, J_{sc} and V_{oc} [116].

Moreover, *FF* can be affected by the balance between the hole and electron mobility [129]. If the mobilities are not balanced, the slower charge carrier will accumulate near one of the electrode resulting in a built-up internal field, consequently space charge effects, leading to a reduction in *FF* [129].

The quality of polymer-cathode interfaces also affects the *FF*. Gupta *et al*. [129] reported that a partial metal coverage or a chemically modified cathode could decrease the *FF* significantly. In addition, they demonstrated that a fine-deposited metallic cathode closely packed to the active polymer layer could improve the *FF*; while a thin layer of aluminum oxide can introduce a charge transport barrier since it can facilitate electron injection from cathode owning to holes accumulation at the Al_2O_3–polymer interface.

In summary, the device performance of OSC is predominantly affected by the choice of the photo-absorbing materials, the thickness and morphology of active layer, electrode materials and the quality of their contact with polymer.

1.5. Plasmonic organic solar cells

Many strategies have been applied in organic solar cells to boost their efficiencies. Developing new materials with a bandgap approaching to the optimum 1.3 eV [33] is a promising solution. For example, PTB7 has a bandgap of 1.8 eV and this make it more attractive photovoltaic component than P3HT (bandgap ~2.1 eV). Controlling the morphology of the blend represents another approach which can remarkably enhance the solar cell performance. Some photonic methods to enhance the light absorption in the active layer are proposed through an optimization of the electromagnetic field distribution in solar cells [30]. These methods involve the use of either photonic crystals [133], quantum dots [134] or plasmonic structures [135,136]. There are also some other new architectures developed such as the optical fiber based architecture and folded reflective architecture [30]. In this thesis, we focus on the plasmonic solar cells built from nanostructures.

Nanoparticles based on noble metals display collective electron oscillations on theirs surfaces, termed localized surface plasmon resonance (LSPR). This resonance creates opportunities for designing and controlling the propagation of light in matter. Human has taken advantage of plasmonic effects since a long time ago. For example, the Roman Lycurgus Cup (4th century AD, now at the British Museum, London) and the gothic stained glass rose window of Notre-Dame de Paris show unique features of changing color or multiple colors due the plasmonic effects induced by the gold or silver nanoparticles.

In modern time, noble metal nanoparticles have found a lot of experimental and industrial applications in many fields, such as chemical and biological sensing [137], optical switching and limiting devices [138], organic light emitting diodes [139], and solar cells [140,141].

In this section, the bulk plasmons, surface plasmons, LSPR and the application of LSPR in solar cells are introduced.

1.5.1. Plasmons

In physics, a plasmon is a quantum of plasma oscillation arisen from the free electron "gas" in conducting material. Similar to polarons in organic semiconductors, the combination of plasmon and the lattice distortion creates a new quasiparticle termed a plasmon polariton [142].

In general, there are three types of plasmons, bulk plasmon (located in a bulk conducting material), surface plasmon (located at planar metal-dielectric interfaces) and localized surface plasmon (highly confined on a small surface, e.g., on the surface of a nanoparticle).

1.5.1.1. Bulk plasmons

In an infinite solid (e.g., metal), the bulk plasmons are longitudinal waves [143]. Due to the fact that light waves are transverse, the wave vector mismatch makes the bulk plasmons incapable to be excited from direct irradiation. However, the bulk plasmons can rise from other perturbation of free electrons, e.g., the optical emission from irradiated metallic foils [144]. According the Drude model, the frequency of a bulk plasmon ω_p in a metal is given by Equation 1. 9 [145]:

$$\omega_p = \sqrt{\frac{ne^2}{m^* \varepsilon_0}}$$ Equation 1. 9

Where n is the conduction electron density, e is the elementary charge, m^* is the effective mass of an electron and ε_0 is the vacuum permittivity.

Hence, if the frequency of an incident electromagnetic wave is higher than bulk plasmon frequency, the metal becomes transparent for this wave. On the other hand the light with lower frequencies will be reflected [146]. The bulk plasmon frequencies of most metals are in the ultraviolet region, associating energies within 5-15 eV, thus enables most metals highly reflective for visible light. But for some metals, e.g., noble metals (copper, silver and gold), they have filled d-shells: Copper has the electronic configuration $3d^{10}4s^1$, and Silver $4d^{10}5s^1$ and Gold $4f^{14}5d^{10}6s^1$. According to the Drude-Lorentz-Sommerfeld model [147], these d-electron bands have lower energies than the Fermi level of the conduction band and thus allowing new narrow transitions (see Table 1. 1 and Figure 1. 26) close to or in visible region [148].

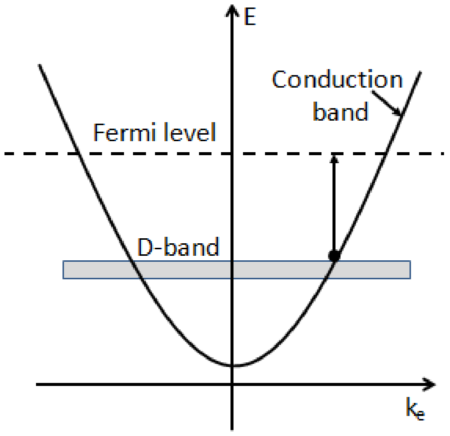

Figure 1. 26 Schematic band diagram for the noble metals [148]: inter-band transition between d-band and conduction band; intra-band transition within conduction band)

Metal	Ag	Au	Cu	Al
Energy (eV)	3.9	2.4	2.1	1.5
Wavelength (nm)	318	521	590	827

Table 1. 1 Interband transition regions for Ag, Au, Cu and Al (adopted from [147,149])

1.5.1.2. Surface plasmons on planar metal-dielectric interfaces

Surface plasmons are plasmons at the metal-dielectric interfaces and tightly bound to the interfaces (Figure 1. 27). Since their wave-vector is larger than light waves, the surface plasmon cannot be directly excited by illumination. Instead, the surface plasmon wave can be generated under special geometries, e.g., Kretschmann-Raether coupler [150], Otto configuration [150,151] and gratings [152], where the dielectric constants of metal and the surrounding dielectric material have the same value but opposite signs. The surface plasmon thus has a frequency related to the bulk plasmon frequency ω_p, given by Equation 1. 10:

$$\omega_{SP} = \frac{\omega_p}{\sqrt{1+\varepsilon_1}} \qquad \text{Equation 1. 10}$$

Where ω_{sp} is the surface plasmon frequency, ε_1 is the permittivity of the dielectric material coupled to the metal material.

The surface plasmon propagates along the dielectric/metal interface and it has a highly concentrated electric field near the interface (z = 0). This electric field exponentially decays away from the surface. The decay rate is much higher in metal than in dielectric. Besides, the surface plasmons are always accompanied with a transverse magnetic (TM) field.

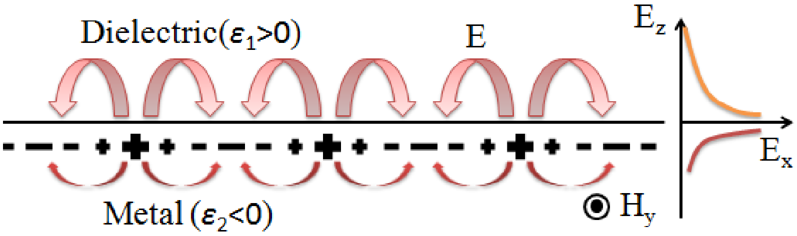

Figure 1. 27 Schematic of charge distribution and electromagnetic field of surface plasmons

1.5.1.3. Localized surface plasmons in metallic nanoparticles

Localized surface plasmons (LSPs) excited in metallic nanoparticles are non-propagating plasmon excitations. Due to the tiny sizes of nanoparticles, they show unique optical and electrical properties.

A simple model of LSPs is shown in Figure 1. 28. Since the size of a metallic nanoparticle is on the same scale of the penetration depth of electromagnetic waves in metals (e.g., 20 ~ 30 nm for Ag and gold [153]), the external field can penetrate the whole particles and shift the conduction elections with respect to the rigid ion lattice. Thus the charges are separated and this charge separation results in a restoring force and then an oscillation. Take the spherical metallic nanoparticle for granted, the polarizability α of a metal particle surrounded by the dielectric material is given by Equation 1. 11 [153,154]:

$$\alpha = \varepsilon_0 3V \frac{\varepsilon_2 - \varepsilon_1}{\varepsilon_2 + 2\varepsilon_1} \quad \text{(Clausius–Mossotti relation)} \qquad \text{Equation 1. 11}$$

Where ε_1 is the permittivity of the dielectric and ε_2 is the dielectric function of the metal, ε_0 is the vacuum permittivity, and V is the particle volume. When $\varepsilon_2 = -2\varepsilon_1$, the polarizability becomes very large suggesting a localized surface plasmon. The oscillation frequency is given by Equation 1. 12 according the Mie theory [154]:

$$\omega_{LSP} = \frac{\omega_p}{\sqrt{1 + 2\varepsilon_1}} \qquad \text{Equation 1. 12}$$

Then the scattering cross-section σ_{scat} and the absorption cross-section σ_{abs} of a spherical metallic nanoparticle are given by Equation 1. 13 and Equation 1. 14 [154]:

$$\sigma_{scat} = \frac{k^4}{6\pi}\left|\frac{\alpha}{\varepsilon_0}\right|^2 = \frac{8\pi}{3}k^4 r^6 \left|\frac{\varepsilon_2 - \varepsilon_1}{\varepsilon_2 + 2\varepsilon_1}\right| \qquad \text{Equation 1. 13}$$

$$\sigma_{abs} = k \operatorname{Im}\left(\frac{\alpha}{\varepsilon_0}\right) = 4\pi k r^3 \operatorname{Im}\left(\frac{\varepsilon_2 - \varepsilon_1}{\varepsilon_2 + 2\varepsilon_1}\right) \qquad \text{Equation 1. 14}$$

Where $k = 2\pi/\lambda$, r is the diameter of the nanoparticle and Im denotes the imaginary part.

It is important to note that, for very small nanoparticles ($r << \lambda$), the scattering cross-section decreases rapidly (due to the $\propto r^6$ relationship), while the absorption decreases less rapidly (due to $\propto r^3$ relation). Hence large particles dramatically scatter light whereas the small particles absorb light significantly, resulting in the various colors of nanoparticles.

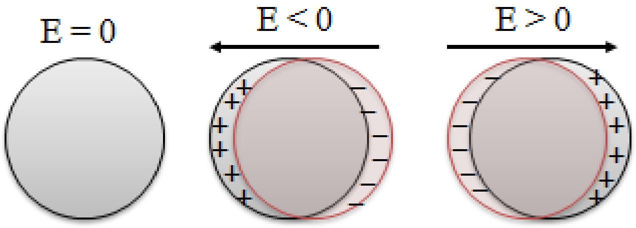

Figure 1. 28 Localized surface plasmons in a metallic nanoparticle

As we can see, the oscillation frequency is mainly related to effective electron mass, charge density and geometry of the particle, as well as the properties of the surrounding medium. The amplitude of the induced electromagnetic field is much stronger than exciting fields (over 10 times) and the magnitude of the resonance is only related to the radiative and non-radiative damping involved. As a result, the properties of localized surface plasmons in noble metallic nanoparticles can be tuned by the composition, size, shape and their environment [155–160].

1.5.1.3.1. Nanoparticle composition

As seen in Equation 1. 9, the bulk plasmon frequency is related to the density and effective mass of electrons in the metal. As a result, the bulk plasmon frequency is significantly affected by the composition of the nanoparticles.

For noble metals, it is more complicated due to the inter-band transition between d-band and conduction band and the intra-band transition within conduction band. The bulk plasmon frequency of noble metals is given by Equation 1. 15:

$$\omega_{sp} = \sqrt{\frac{ne^2}{m^* \varepsilon_0 \left(\varepsilon_\infty + 2\varepsilon_1\right)}} \qquad \text{Equation 1. 15}$$

Where ε_∞ is the additional part of dielectric function and it depends on the metal d-electrons (e.g., response of 5d electrons for gold) [161,162]. Here, the real part of the permittivity determines the frequency while the imaginary part is related to the damping processes.

In general, the composition of the nanoparticles is one of the key factors determining the properties of plasmons.

1.5.1.3.2. Nanoparticle size

The size of nanoparticles is another important factor affecting the plasmon properties. For example, according to Equation 1. 13 and Equation 1. 14, the absorption and scattering cross-sections of nanoparticles increase with increasing particle size. Another size-induced effect (the size should be large enough to make the electric field retarded across the particle surface) is the high-order plasmons, which have higher oscillation frequencies than the first order plasmons. This leads to the broadening of plasmon resonance due to a reduction in phase coherence [162,163].

With the increasing nanoparticle size, the radiation damping (which inverts the plasmons into photons [153,164] and leads to scattering) will increase and it is proportional to the particle volume [164,165]. As a result, the increasing damping leads to a redshift of plasmonic resonance and a shortening of the dephasing time T_2 (and a broadening of linewidth since homogeneous linewidth $\Gamma = 2\hbar/T_2$ [164]) [147,162,164,165]. The increasing radiation damping also results in a decrease of magnitude of plasmonic resonance [166,167]. In addition, as the size increases (> 10 nm for gold [147]), the increased electromagnetic retardation from dynamic depolarization can also lead to a redshift of plasmon resonance [147,162–164,166].

For very small nanoparticles (< 2-3 nm), quantum size effects become important, and the treatments used above are no longer valid [162].

1.5.1.3.3. Nanoparticle shape

Essentially, the plasmons are dipoles or high order resonance modes arisen from collective free electron (conduction electron cloud) oscillations within the rigid positive metallic lattice. This charge separation forms a restoring force in response to the incoming light polarization. Compared to a sphere, in nanoparticles with sharper surface curvatures along the light polarization direction there is weaker restoring force leading to a lower plasmon resonance frequency (redshift) [162]. The polarizability α of a nanoparticle of arbitrary shapes is given by Equation 1. 16 [154,162]:

$$\alpha = \frac{\varepsilon_0 V}{L}\left(\frac{\varepsilon_2 - \varepsilon_1}{\varepsilon_2 + \left(\frac{1-L}{L}\right)\varepsilon_1}\right) \qquad \text{Equation 1. 16}$$

Where L is the depolarization factor which depends on the shape. For nanospheres, L is 1/3.

Haes *et al*. [168] demonstrated by simulations that Ag nanoparticles with different shapes but the same volume have significant different optical properties (Figure 1. 29). The main in-plane plasmonic resonance position is red-shifted when the number of sharp tip or edges are increased or when the shape is altered. This is consistent with the reference [162], which found that Ag nanoparticles of sharper shapes have lower resonance frequencies. This is also demonstrated by simulation of tip-truncated (or snipped) triangular nanoparticles [169]: The resonant position is blue-shifted by the introduction of tip truncations (Figure 1. 30). This simulation prediction is confirmed by the experimental results of Zhang *et al*. [170]: blue-shift occurred when an oxidation process rounded the tips of Ag nano-triangles.

Similar simulation results [171] further show that the increase of edge length or the decrease of thickness leads to a redshift in the main in-plane resonance while the quadrupole plasmon modes are not sensitive to tip-snipping. The different sensitivities to tip shape change is due to that: the main in-plane dipole has strong localization of electric field around the triangle tips and thus is sensitive to change in the shape of the tips, while the in-plane quadrupole has localization of electric field at the sides of the triangle and thus is not sensitive to the shape variation of the tips (Figure 1. 31).

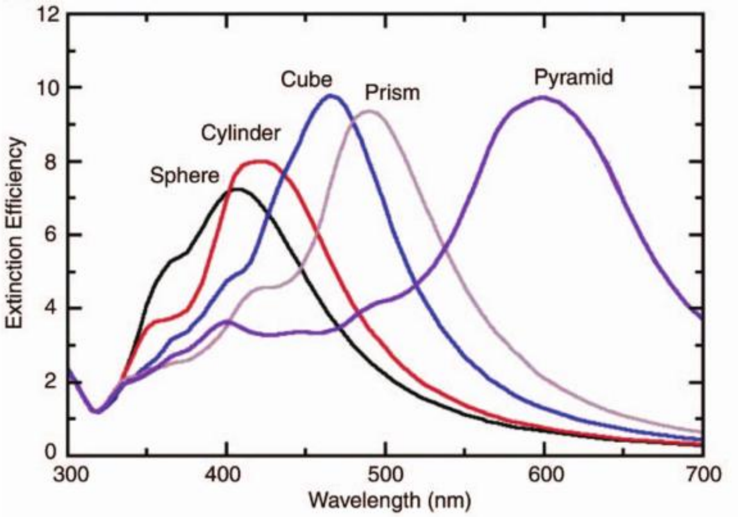

Figure 1. 29 Finite-difference time-domain (FDTD) extinction simulations of Ag nanoparticles with identical volume, taken to be that of a sphere with a radius of 50 nm (reprinted from [168], Materials Research Society, MRS Bulletin)

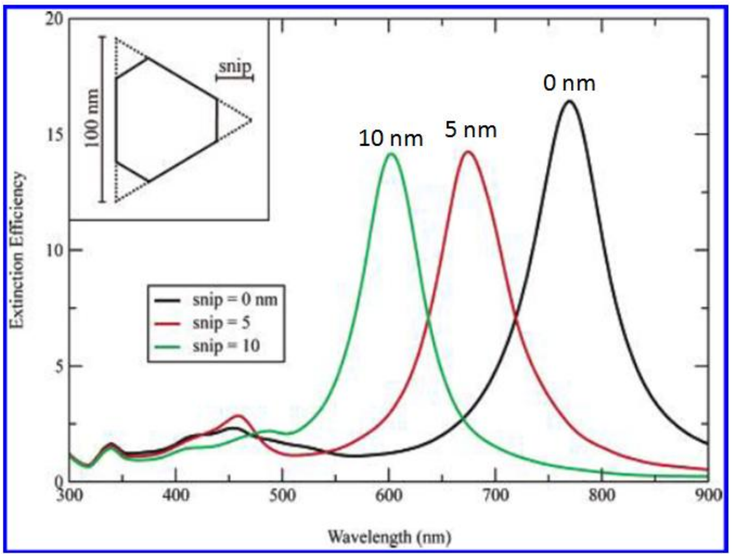

Figure 1. 30 DDA extinction simulations of tip truncated triangular prisms. Inset: the shape of a snipped prism. The prism thickness is 16 nm. (reprinted from [169], American chemistry society, the Journal of Physical Chemistry B).

Nanorods, representing the simplest example of anisotropic nanoparticles, have two distinct transverse and longitudinal localized surface plasmons. Generally speaking, the long-axis resonance takes the dominant place in the optical response of nanorods. It red-shifts linearly as the aspect-ratio (ratio of length to diameter) increases from 1 to 5 for a constant nanocrystal volume [160,172]. This is due to that the increasing aspect-ratio leads to a reduction of the storing force for longitudinal resonance and thus lowers its frequency. On the other hand, the short-axis resonance is only weakly affected by the particle aspect-ratio [172]. Results from theoretical and experimental measurements have confirmed this relationship [156]. Moreover, the end-cap of nanorods has an effect on the longitudinal resonance position as well: The resonance peak red-shifts when the end-cap is approaching a flat surface [160,173].

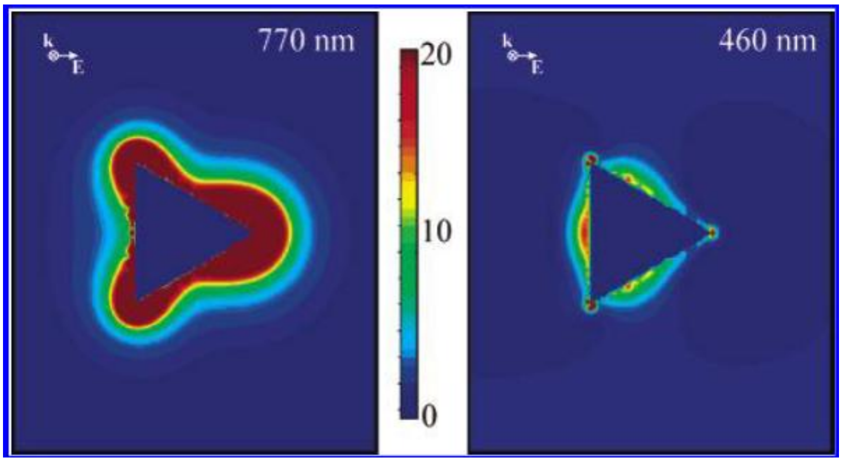

Figure 1. 31 Simulations of electric-field enhancement contours external to the Ag triangular prism, left is in-plane main dipole and the right is in-plane quadrupole (reprinted from [169], American chemistry society, the Journal of Physical Chemistry B)

Moreover, the nanoscale surface roughness could also affect the plasmon resonance peak position. It has been reported that the increased surface roughness of Au nanoshells could result in a red-shift in the resonant position [174].

Finally, as mentioned in the previous section, the radiation damping in nanoparticles is proportional to the volume the particle [164,165]; for a given resonance energy, nanoparticles with different shapes have different particle volumes (e.g., volume $V_{rod} < V_{sphere}$) [164]. Therefore, the radiation damping is significantly affected by the shapes of nanoparticles.

1.5.1.3.4. Environmental medium

As seen in Equation 1. 12 and Equation 1. 15, the increase in the dielectric constant of surrounding medium will lead to a decrease in the plasmonic frequency. This is because the polarization of the embedding medium (with high dielectric constant) will lower the restoring force of the plasmon by the shielding of the surface charges and thus lower the plasmon frequency [162]. As it is proportional to the dielectric constant ($n = (\varepsilon/\varepsilon_0)^{1/2}$), the refractive index has the same effect on the optical properties of plasmons: mediums with high refractive indexes lead to a red-shift in the plasmonic resonance. This has been demonstrated by experimental results [135] and simulations [160,169]. As a result, the plasmon resonance frequency can be modulated by varying the refractive index of the surrounding medium through altering the solvents or substrates [135,169,175]. Another effect of the refractive index on the optical properties of plasmons is that light is preferentially scattered by plasmons into the high-index substrate [135,136].

Defects, surface ligands and adsorbates can also influence the optical properties of nanoparticle plasmonic resonance through damping due to a perturbation of the conduction electron density [176–179].

1.5.1.3.5. Inter-particle coupling

Besides the composition, size, shape and environmental medium, the interparticle couplings can also affect the optical properties of plasmonic resonance.

There are two kinds of couplings: near field coupling and far field coupling. Near field coupling occurs when the interparticle spacing is smaller or comparable to the particle size. Far field coupling is generated from nanoparticle arrays with periodic structures at larger spacing.

For near field coupling, results shows that near field interparticle coupling results in a red-shift of plasmonic resonance compared to an isolated nanoparticle. With decreasing spacing, the plasmonic peak red-shifts further to longer wavelength ranges. Within the gap between two nanoparticles, the electric field is dramatically enhanced [180,181].

For periodically arranged nanoparticles, the interaction between the scattered photons (scattered by the periodical nanoparticles) results in a change in the plasmonic resonance spectrum. The grating period and the incident light polarization both play important roles to modulate the optical properties of nanoparticles. Results [182] show that with incident light polarization direction parallel to the long nanoparticle pair axis, decreasing the interparticle spacing will lead to stronger red-shift of the plasmonic resonance. If the incident light polarization direction is orthogonal to the long nanoparticle pair axis, a stronger blue-shift will be obtained with decreasing interparticle distance (Figure 1. 32).

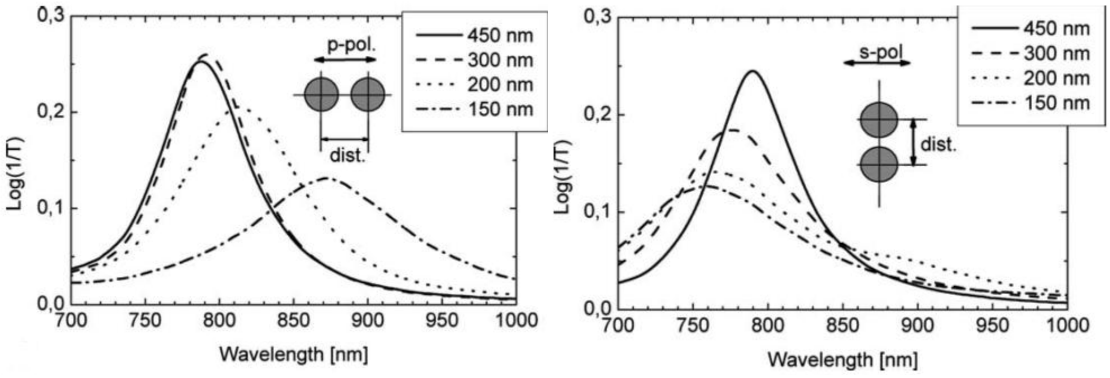

Figure 1. 32 Extinction spectra of a 2D array of the Au nanoparticle pairs with the interparticle center-to-center spacing as the parameter [182]

1.5.2. Organic solar cells utilizing localized surface plasmons

Localized surface plasmons have a wide range of application in many fields owing to their scattering and absorption characteristics. For example, light-scattering imaging [183], refractive index sensing [184], surface enhanced Raman scattering spectroscopy [185] and laser nanostructuring [186]. In this these, we focus on the application of localize surface plasmons in OSCs.

1.5.2.1. Mechanisms of light absorption enhanced by localized surface plasmons

In recent years solar cells utilizing localized surface plasmons have attracted many attentions [39,187,188]. In general, there are two common ways to take advantage of the localized surface plasmons to enhance the light absorption in plasmonic solar cells in order to enhance their efficiency: light scattering and light concentration (Figure 1. 33) [136].

1.5.2.1.1. Light concentration

For the metallic nanoparticles of diameters much smaller than the incident light wavelength (5 – 20 nm), the absorption of nanoparticles is dominant compared to scattering. If a semiconductor is close enough to couple with the near field of a metallic nanoparticle which is enhanced by localized surface plasmons, the effective absorption cross-section of the semiconductor will increase [136,188,189]. Due to this phenomenon, in such situation more excitons can be generated without modifying the illumination nor the active semiconductor layer of the solar cells [189].

This effect suggests that the incorporation of the metallic nanoparticles inside the active layer can be a tool to improve the light absorption and the solar cell efficiency. While it is important to note that the recombination of charge carriers at the metal/semiconductor interface can be a negative issue and the ohmic damping can convert the absorbed energy into heat [136].

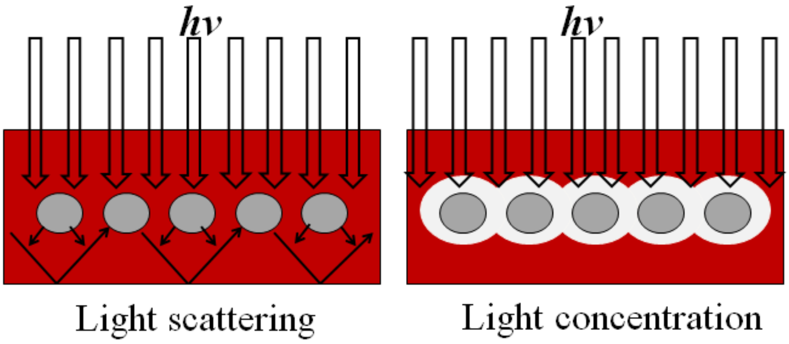

Figure 1. 33 Different light trapping mechanisms: light scattering from large diameter (>50 nm) metal NPs into high angles within the photoactive layer, causing elongated optical path lengths; light concentration induced by localized surface plasmon resonance from small diameter (5–20 nm) metal particles.

1.5.2.1.2. Light scattering

For nanoparticles with a relatively large diameter (> 50 nm), the light scattering is dominant compared to absorption. Due to the localized surface plasmon resonance, the scattering cross-section of a nanoparticle is much larger than its geometric cross-section [154]. A 100-nm-diameter Ag nanoparticle has an albedo (reflection coefficient, the ratio of reflected radiation from the surface to incident radiation upon it) over 0.9 [135].

In addition, light is preferentially scattered by plasmons into adjacent high-index layers [135,136], e.g., organic semiconductors. The scattered light has an angular spread in organic semiconductors [135] and thus the effective optical path is elongated by scattering or reemitting in different directions within the device (and resulting an over 10-fold increase) (Figure 1. 33) [136,188,190]. The absorption then can be improved by the increase of the effective optical path.

1.5.2.2. Plasmonic organic solar cells

Depending on the position of nanoparticles in the solar cells, plasmonic solar cells have three major device configurations: nanoparticles inserted in the photoactive layer, in the buffer layer and between these layers (Figure 1. 34) [190].

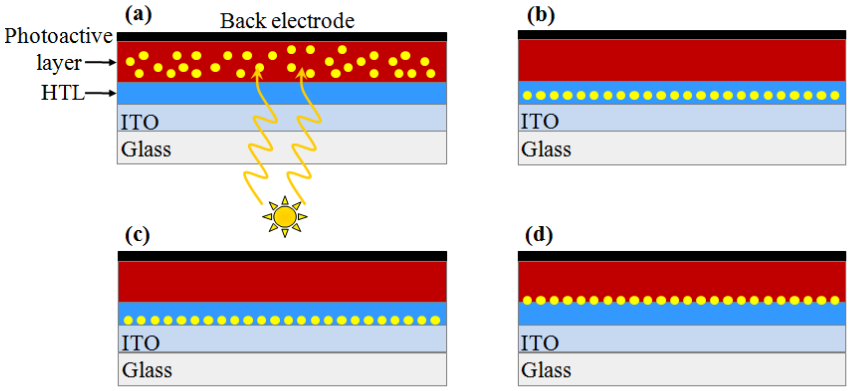

Figure 1. 34 Schematic of different configurations of OSCs incorporated with nanoparticles (NPs) at different position. (a) NPs in photoactive layer, (b) NPs in hole transport layer (HTL), (c) NPs at ITO/HTL interface and (d) NPs at HTL/photoactive layer interface.

1.5.2.2.1. Nanoparticles in the photoactive layer

This type of architecture takes advantage of both light scattering and concentration. By tuning the nanoparticle material composition, shape and size, organic solar cells with enhanced performance can be obtained. However, because of the surfactants or ligand coatings of nanoparticles, excitons may be quenched at the nanoparticle/photoactive layer interface, leading to a decrease in device performance [190–192]. It is also reported that the incorporation of nanoparticles (e.g., Ag nanoparticles) can increase the charge mobility due to the higher conductivity of metallic materials, although a decreased device performance has been found owing carrier recombination [193]. By comparison, an insulating inorganic layer over the nanoparticle can be used to prevent surface recombination. But this will dramatically decrease the absorption enhancement depending on the thickness of the insulating layer [194]. Spyropoulos *et al* [189] investigated the case of surfactant-free Au nanoparticles embedded in the active layer. With incorporating 6% gold nanoparticle inside the active layer, an increase of efficiency by a factor of 1.34 has been achieved in P3HT:PCBM bulk heterojunction solar cells.

1.5.2.2.2. Nanoparticles in hole transport layer

This type of architecture takes advantage mainly of light scattering. Solar cells having this structure also benefit from hole collection improvement and exciton quenching reduction [190]. The improved hole collection is contributed to increased area of the interface between the buffer layer and active layer which is induced by incorporation of nanoparticles in buffer layer [195]. A reduction of resistance induced by the incorporation of nanoparticles is also reported [196]. Some examples of this concept have been successfully achieved to obtain enhanced efficiencies. For instance, with the incorporation of 60-nm-diameter Ag nanoparticles in PEDOT:PSS layer, an efficiency enhancement of more than 20% has been obtained for tandem organic solar cells by Yang *et al* [190,197].

1.5.2.2.3. Nanoparticles between different layers

There are two possible configurations to insert nanoparticles between the different layers of an organic solar cell. They can possibly located between the ITO and the PEDOT:PSS layer or between the PEDOT:PSS and the photoactive layer (Figure 1. 34). These configurations can be realized by different deposition techniques, such as vacuum evaporation assisted with thermal annealing [198] or with template [199], self-assembly using silanes [200], spin-coating from nanoparticle solution [201,202].

For the configuration of having nanoparticles at the ITO/PEDOT:PSS interfaces, the solar cells may only take advantage of light scattering due to the localized surface electric field which only reaches to a few tens of nanometers around the nanoparticle [188]. As the thickness of PEDOT:PSS layer is typically 40 – 50 nm, the enhanced surface electric field can hardly extend into the active layer. In contrast to placing nanoparticles within photoactive layer, this configuration can avoid exciton quenching at the nanoparticle/photoactive layer interface. The nanoparticles may also excite the surface plasmon polaritons along the ITO surface helping charge carriers collection [190].

For the device configuration with nanoparticles inserted at the PEDOT:PSS/photoactive layer interfaces, it is similar to the case of placing nanoparticles in the active layer. In this case the solar cells can benefit from both the light scattering and absorption even though exciton quenching can also potentially happen at this interface. Ligand-capped nanoparticles located at this interface have been reported to lead to a decrease of efficiency [202]. This decrease is due to the carrier recombination owning to the existence of nanoparticles. It has also been reported that ligand-free Ag and Au nanoparticles located at this interface leads to an efficiency enhancement of 20% [203].

1.6. Conclusions

This chapter has presented the background knowledge about the OPVs, plasmons and the plasmonic OPVs.

First of all, a state-of-art of PVs, especially OSCs, was introduced. After that, the basic knowledge of organic semiconductors was presented, including their development and electronic structure, as well as the excitons and polarons in them. Particularly, the photo-conversion process was detailed introduced, including the photon absorption, exciton generation, exciton diffusion, dissociation of excitons at the donor/acceptor interface, charge transport to electrodes and charge collection at the electrodes. The general and specific architectures of OSCs were also introduced. Among them, the bulk heterojunction OSCs using P3HT:PCBM was highlighted, including the properties of the buffer layer (PEDOT:PSS), P3HT, PCBM and P3HT:PCBM blend. In addition, the general photovoltaic characteristics of OSCs and particularly the performance limiting factors were introduced.

In the second part, the bulk plasmon, the surface plasmon on planar metal-dielectric interface and the localized surface plasmon resonance (LSPR) on the metallic nanoparticles (MNPs) were introduced. Particularly, the factors that affect the LSPR on MNPs (size, shape, surrounding medium and inter-particle couplings) were highlighted. The mechanisms that could enhance the efficiency of OSCs using MNPs were subsequently presented, including light scattering and concentration. After that, we introduced various plasmonic OSC configurations and samples with MNPs incorporated at different locations in them.

Chapter II

Experimental methods and techniques

This chapter introduces the experimental methods and the main characterization techniques used throughout this thesis.

2.1. Materials

The main materials used in this thesis are listed in Table 2. 1 and Table 2. 2, for the synthesis of silver nanoparticles and for the fabrication of components related to organic solar cells, respectively.

Table 2. 1 lists the main materials used to synthesize Ag nanoparticles. All the materials are used as received without further purification. De-ionized (DI) water is used throughout for all solutions during the Ag synthesis if no otherwise specified. The Ag nanoparticles synthesis and characterization will be shown in Chapter III.

The PEDOT:PSS solution used in this thesis was a product of Heraeus Group (named “Clevios^{TM} P”) [72]. The PEDOT-to-PSS ratio by weight is 1:2.5 [204]. The structure of PEDOT:PSS is shown in Figure 1. 16.

Material name	Chemical formula	Average M_W	Assay/Quality level	Provider
Silver nitrate	$AgNO_3$	-	99.9999% trace metals basis	ALDRICH
Trisodium citrate dehydrate	$HOC(COONa)(CH_2COONa)_2 \cdot 2H_2O$	-	Premium, meets USP testing specifications	SIGMA-ALDRICH
poly(sodium styrenesulphonate) (PSS)	$[C_8H_7NaO_3S]_n$	1000000	-	ALDRICH
Sodium borohydrate	$NaBH_4$	-	for the determination of hydride formers by AAS, ≥99%	FLUKA
L-ascorbic acid	$C_6H_8O_6$	-	ACS reagent, reag. ISO, reag. Ph. Eur.	SIGMA-ALDRICH

Table 2. 1 Materials used to synthesize silver nanoparticles

A polymer-fullerene blend of regioregular poly(3-hexylthiophene) (P3HT) and [6, 6]-phenyl-C61-butyric acid methyl ester (PCBM) was used to fabricate organic solar cell samples in this thesis. The chemical structures of P3HT and PCBM are shown in Figure 1. 18

and Figure 1. 22. P3HT is a semiconducting polymer. It is used as a donor material and PCBM acts as an electron acceptor in bulk heterojunction photovoltaic devices.

IUPAC name	Abbreviation	Average M_W	Orbital energy
poly(3,4-ethylenedioxythiophene): poly(styrenesulfonate)	PEDOT: PSS	-	Work function: -5.2 eV
poly(3-hexyl thiophene)	P3HT	45,000-65,000	LUMO: -3 eV HOMO: -5 eV
1-(3-methoxycarbonyl)-propyl-1-phenyl-[6,6] C61	PCBM	-	HOMO: -6.5 eV LUMO: -4.3 eV [205]

Table 2. 2 Main polymer materials used in this thesis

In this thesis, the P3HT was a product of Plextronics Inc. named “Plexcore OS 2100”, and PCBM was supplied by Solaris-Chem Inc. named “SOL5061”. The P3HT and PCBM were supplied at a high degree of purity and thus were used as received without further purification. These two materials have excellent solubility in common organic solvents, including chloroform (CF), chlorobenzene (CB) and 1,2-dichlorobenzene (DCB). CB and DCB were chosen as solvents in this thesis.

2.2. Film and photovoltaic device preparation

2.2.1. General preparation technique for thin films: Spin-coating

Films were realized by spin-coating in this thesis. Spin-coating is a standard technique to make uniform thin polymer films on substrates. The spin-coating procedure is carried out as follows: Typically, a small amount of diluted polymer solution is applied by a pipette on the center of the substrate which is held on a chuck by vacuum. The substrate then is rotated at high speed (typically over 1000 rpm) to spread the coating materials to, eventually off, the edges of the substrate by centrifugal force, leaving a very thin polymer film on the substrate surface. During this process, the excess solvent is spun off the substrate or evaporated. In principle, the thickness depends on two factors: (1) the spin speed and time, (2) the viscosity and concentration of the solution. In principle, thin films will be obtained if high spin speed and long spin time, or low viscosity and concentration of the solution. Therefore, an appropriate spin speed and time must be set to get a desired film thickness. The correlation between film thickness and spin speed and time is shown in Figure 2. 1. In general, the film thickness is proportional to the inverse of the square root of the spin speed as in Equation 2. 1 [206,207]:

$$h = k\frac{1}{\sqrt{\omega}} \qquad \text{Equation 2. 1}$$

Where h is the film thickness, ω is the angular velocity, k is a constant. For each sample solution, k is varied with the variation of solution viscosity, density and concentration, etc. For spin duration, if the spin time is longer than a certain time, t_0, the film thickness will not change any more since the solvent is completely evaporated (Figure 2. 1). But within this time, the film thickness decreases very fast with increasing spin time. For common solvents, such as water and Toluene, t_0 is shorter than 30 s, and for dichlorobenzene, longer spin time is needed [206]. Typically, we can obtain ultrathin films, e.g., tens of nanometers, by using this method at a very high spin speed.

In this work, for PEDOT:PSS films, the spin coating was always carried out in air in a clean room. For P3HT:PCBM solution, the spin coating was always performed in nitrogen-filled glovebox under air-free and water-free conditions.

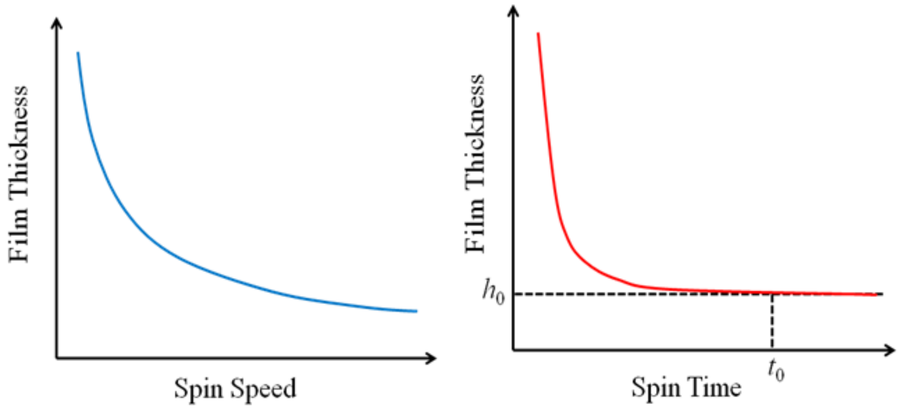

Figure 2. 1 Film thickness as a function of spin speed and spin time [208]

2.2.2. Preparation of films and photovoltaic device samples

2.2.2.1. General preparation procedure for films on glass substrate or ITO-coated substrate and for photovoltaic devices

For films prepared on glass substrates and ITO-coated glass substrates, the glass and ITO-coated glass substrates must be cleaned prior to use. For photovoltaic devices, they were realized using conjugated P3HT as the donor material, PCBM as the acceptor material and regular device architecture: Glass / indium tin oxide (ITO) / PEDOT:PSS / P3HT:PCM / Al cathode (Figure 2. 2).

Unless stated otherwise, the films and organic solar cells (OSCs) used in this thesis were prepared following the general preparation procedure as follows:

1) **Substrate cleaning**: Usually, The ITO-coated substrate is protected by a photoresist layer and this layer can be removed by cleaning. Firstly, we used acetone to rinse the ITO-coated substrate to remove the photoresist layer. To ensure this removal, a cotton bud dipped with methanol was used to gently wipe the ITO surface. To further clean the ITO-coated substrate, four sequential ultrasonic baths (40 kHz) in diluted detergent (Thermo Scientific PCC-54 Detergent Concentrate, Thermo Fisher Scientific Inc.; 2 vol% in de-ionized water), de-ionized (DI) water, acetone and isopropyl alcohol were performed (respectively 15 minutes in each solvent). They were then further cleaned by RF oxygen plasma (using SPI Plasma-Prep II Plasma Etcher Cleaner and Asher, supplied by SPI Supplies) for 10 minutes to decompose any organic contaminants remained after ultrasonic baths. The glass substrates were cleaned using the same procedures as the cleaning of ITO-coated glass substrates.

2) **Spin-coating of PEDOT:PSS thin films**: A layer of PEDOT:PSS (Clevios P) was spin-coated over the cleaned ITO-coated substrates. In this thesis, the thickness of PEDOT:PSS was kept to be about 40 nm, which is the optimal thickness we found for organic solar cells. The resulting PEDOT:PSS films were then annealed at 230 ^{o}C for 30 minutes on a hotplate in a nitrogen-filled glovebox to avoid oxygen and moisture. Before spin-coating, the pristine PEDOT:PSS was filtered by a polyvinylidene difluoride (PVDF) syringe filter with a pore size of 0.45 μm.

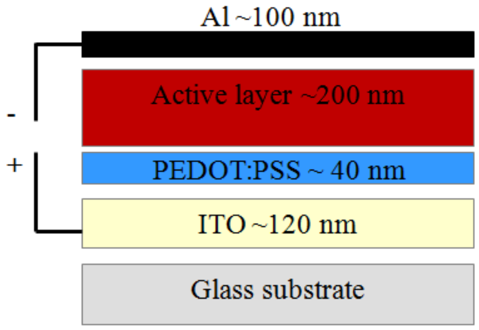

Figure 2. 2 Typically regular architecture of a bulk heterojunction organic solar cell

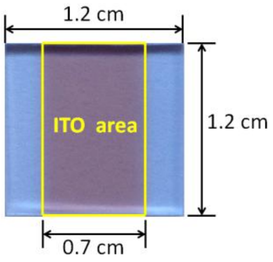

Figure 2. 3 Photograph and dimensions of ITO-coated glass substrate

3) **Spin-coating of photoactive layer:** The P3HT:PCBM blend was dissolved in 1,2-dichlorobenzene (DCB). The weight ratio between P3HT and PCBM is 1:1, and the concentration of P3HT in DCB is 20 mg/mL. The solution firstly was heated at 90 ^{o}C for at least 10 minutes and then kept at 50 ^{o}C over-night. Vigorous stirring was applied throughout all this procedure. The P3HT:PCBM photoactive layer was then directly spin coated on top of PEDOT:PSS layer at 1000 rpm for 80 s. The thickness of the P3HT:PCBM photoactive layer was about 200 nm.

4) **Back electrodes deposition:** Over the photoactive layer, a 100 nm-thick aluminum layer was deposited under vacuum using a shadow mask. Aluminum was used here as cathode due to the close alignment between its work function (4.28 eV [209]) and the LUMO of PCBM (4.30 eV). In our case, the surface area of each cell is 0.0426 cm^{2}. For deposition, the vacuum pressure was in the order of 10^{-6} mbar, and the evaporation rate and thickness were monitored by a quartz crystal oscillator. To avoid any potential damage in the photoactive layer, the evaporation rate was limited to 0.1 nm/s for the initial 10 nm to 20 nm before being increased to 0.5 nm/s for the rest of 90 nm. The evaporator was located outside the N_2-filled glove box so care must be taken to shorten the time of exposing devices to air and light. To manage this, a container integrated with a manual vacuum pump in the lid was used.

5) **Post-annealing, making contacts and encapsulation:** The devices were then transferred into the glovebox for post-annealing and encapsulation. First, in order to make contact, part of the resulting layers (PEDOT:PSS and photoactive layer) close to one of the edges of the devices where there is no Al was gently scratched off to expose the ITO coating. The devices were then annealed on a hotplate in the glovebox for 10 minutes. After that, by adding lead frames with zero insertion force (ZIF) sockets, devices can be inserted into a prototyping box allowing electrical connection to sample cells for characterizations. Finally, a drop of resin was placed on the Al electrode which was further covered by a glass slide. The resin was gently pressed by the glass to spread over the entire area under the glass slide. Care was taken in order to eliminate any air bubbles. The encapsulated devices were kept horizontal in glovebox over night to solidify the resin, then the devices were ready for use.

2.2.2.2. *Preparation of sample PEDOT:PSS films and OSCs for optimization of PEDOT:PSS layer by post-deposition thermal annealing*

2.2.2.2.1. *PEDOT:PSS films*

In literature, the annealing temperature typically varies from 100 ℃ to 250 ℃ to investigate its effects on the properties of PEDOT:PSS films, or even higher than 250 ℃ to study the degradation mechanism of PEDOT:PSS. In this thesis, to obtain the optimal PEDOT:PSS annealing temperature for applications, we annealed the PEDOT:PSS films (40nm-thick) for 30 minutes at 150 ℃, 200 ℃, 230 ℃, 240 ℃, 250 ℃, respectively.

2.2.2.2.2. *Organic solar cells*

The PEDOT:PSS films were annealed for 30 minutes at 150 ℃, 200 ℃, 230 ℃, 240 ℃, 250 ℃, respectively; the P3HT:PCBM blend (the P3HT:PCBM ratio was 1:0.8 in weight and the total blend concentration was 22.5 mg/mL in chlorobenzene) thickness was 120 nm, and the OSCs were annealed at 150 ℃ for 10 minutes.

2.2.2.3. *Preparation of sample PEDOT:PSS films and OSCs for optimization of PEDOT:PSS layer by adding glycerol*

2.2.2.3.1. *PEDOT:PSS films*

Different volume percentages including 2.5%, 5.0%, 7.5% and 10.0% of glycerol were added into the PEDOT:PSS solutions, respectively. In order to be well dispersed, the mixed PEDOT:PSS solutions were vigorously stirred for 30 minutes at 1300 rpm. For comparison a pristine PEDOT:PSS dispersion was also prepared. The PEDOT:PSS films (with 0%, 2.5%, 5.0%, 7.5% and 10.0% of glycerol) were annealed in glovebox at 230 ℃ for 30 minutes.

2.2.2.3.2. *Organic solar cells*

A control sample OSC using pristine PEDOT:PSS and an OSC using 7.5 vol.% glycerol modified PEDOT:PSS (denoted as G-OSC) were also prepared. In these two OSCs, the PEDOT:PSS layer were also annealed at 230 ℃ for 30 minutes; The P3HT:PCBM blend (the P3HT:PCBM ratio was 1:0.8 in weight and the total blend concentration was 22.5 mg/mL in chlorobenzene) thickness was 120 nm, and the OSCs were annealed at 150 ℃ for 10 minutes.

2.2.2.4. *Sample preparation for optimization of photoactive layer*

2.2.2.4.1. *Organic solar cell samples using thermal annealing*

In order to obtain the optimum annealing parameters for active layer, we fabricated devices following the general fabrication procedure mentioned in Section 2.2.2.1 and we tested different post-deposition annealing temperatures (devices annealed after electrode deposition): 130 ℃, 140 ℃, 150 ℃, 160 ℃ and 170 ℃, all for 10 minutes.

2.2.2.4.2. Organic solar cell samples using solvent annealing and addition of additive

In order to enhance the efficiency of P3HT:PCBM cells, both the solvent annealing and additive (n-hexane) were applied. The fabrication conditions of sample devices were listed in Table 2. 3. The photoactive layer of OSC no.2 was spin-coated at 1000 rpm for 60 s. After spin-coating for 60s, the film was still wet. This wet film was then put inside a covered glass petri dish until completely dried (judging by color change when the film becomes solid from liquid phase). For sample OSC no.3, 0.2 mL of n-hexane were slowly added into a 1 mL well-dissolved P3HT:PCBM dispersion in DCB with magnetic stirring. Except for this all other fabrication parameters were the same to sample no.2. OSC no.1 is the "control sample" and it was spin-coated at 1000 rpm for 80 s so that the film was completely dried after spin-coating. All these three samples were annealed at 150 ℃ for 10 minutes after Al electrode deposition.

Sample no.	Additive (hexane)	Slow solvent annealing	Thermal annealing	Note
1	No	No	150 ℃ 10 minutes	Control sample
2	No	Yes		Solvent annealing
3	Yes	Yes		Additive (hexane) + solvent annealing

Table 2. 3 Fabrication conditions of control OSC and OSCs using solvent annealing and additive

2.2.2.5. Sample preparation for plasmonic OSCs using Ag NPSMs in PEDOT:PSS layer

The sample devices are fabricated following the general fabrication procedure described in Section 2.2.2.1. The conditions applied to achieve hybrid PEDOT:PSS was the same as those presented in section 3.3.1. For clarity important fabrication conditions are listed in Table 2. 4.

Sample no.	1 (control sample)	2	3	4
PEDOT:PSS (40 nm-thick)	Pristine	0.6 mg/mL Ag NPSMs	1.6 mg/mL Ag NPSMs	2.6 mg/mL Ag NPSMs
	Annealed at 230 ℃ for 30 minutes in a N_2-filled glovebox.			
Active layer (200 nm-thick)	Spin-coated at 1000 rpm for 60 s, dried in glass petri dishes; Annealed at 150 ℃ for 10 minutes in a N_2-filled glovebox.			

Table 2. 4 Fabrication conditions of plasmonic solar cells

2.2.2.6. Sample preparation for plasmonic OSCs using Ag NPSMs and glycerol in PEDOT:PSS layer

In this part, we used the glycerol, an solvent additive, to dramatically reduce the sheet resistance of hybrid Ag NPSM-PEDOT:PSS films. The general fabrication process of plasmonic solar cells is identical to the process described in the Section 2.2.2.5. In addition to this general process, various volumes of glycerol were added into the resulting hybrid PEDOT:PSS-Ag NPSM solution followed by stirring and ultra-sonication. These solution were then used in spin-coating to achieve hybrid PEDOT:PSS-Ag films (40 nm-thick).

The important fabrication parameters of the control sample and the glycerol modified plasmonic OSCs (denoted as G-plasmonic OSCs) were listed in Table 2. 5, whereas other preparation steps are identical to those used in Section 2.2.2.5.

Sample no.	PEDOT:PSS
1 (control)	Pristine
2	0.6 mg/mL Ag NPSM + 1.0 vol% glycerol
3	0.6 mg/mL Ag NPSM + 2.0 vol% glycerol

Table 2. 5 Fabrication parameters of G-plasmonic OSCs

2.3. Characterization Methods

2.3.1. Characterization technique for Ag nanoparticles and solutions

2.3.1.1. UV-visible absorption for solutions

UV-Vis absorbance was performed using a Varian Cary 5E UV-Visible-NIR spectrometer. It has an operating range of 200 - 3300 nm with a resolution of 0.5 nm using a deuterium arc lamp as a source of UV radiations and a tungsten halogen lamp as the source of VIS-NIR radiations.

When carrying out the measurement, it contains four steps: Firstly, collect the "blank" spectrum without any sample loaded. Second, collect the "black" spectrum by blocking the beam completely; third, load a reference sample and then collect the absorption baseline; finally, load the sample and collect the absorption spectrum.

The UV-Vis absorbance of the solution, referred to as optical density (OD) can be determined by the Beer-Lambert absorption law using Equation 2. 2:

$$\mathrm{OD} = -\log_{10}\left(\frac{T_S - T_0}{T_R - T_0}\right) \qquad \text{Equation 2. 2}$$

Where T_0 is the background noise signals of the system, T_R is the transmission of the reference and T_s the transmission of the sample solution. In fact, this is automatically calculated by supplementary software and we will directly obtain the absorbance spectra at the end of the measurement.

2.3.1.2. X-ray Diffraction

X-ray diffraction (XRD) is a chief technique to identify the atomic and molecular structure of a crystal. In this technique, the atomic planes in a crystal cause a beam of incident X-rays to interfere with one another when they leave the crystal in many specific directions. The angles (θ) and intensities of these diffracted X-ray beams can be used to identify different crystal structures. We can use Bragg's Law (Equation 2. 3) to describe this relation of the angle and the spacing between atomic layers:

$$\mathrm{n}\lambda = 2d\sin\theta \qquad \text{Equation 2. 3}$$

Where the variable *d* is the distance between atomic layers in a crystal, and the variable lambda λ is the wavelength of the incident X-ray beam; n is an integer.

Moreover, XRD is a nondestructive technique. Therefore, by using XRD technique, we can identify crystalline phases and orientations; determine structural properties such as lattice parameters, grain size, phase composition, internal stress of small crystalline regions, thermal expansion; measure thickness of thin films and multi-layers, etc.

In our case, the XRD pattern was collected using Philips X'PERT MPD with software of X'Pert Data collector by exposing powder samples on silicon substrate to Cu-K_α X-ray radiation. The X-rays have a characteristic wavelength of 1.5406 Å and were generated from a Cu anode supplied with 40 kV and a current of 40 mA.

2.3.1.3. Transmission electron microscopy

The transmission election microscopy (TEM) is a microscopy technique using an electron beam as light source. When shinning an electron beam onto a matter, various signals will be arisen since the electron-matter interaction. These signals offer unique possibilities to gain insights into structure, topology, morphology, and composition of a material. For example, the electron-matter interaction produces characteristic x-rays and these x-rays can be detected by electron microprobe to analyze the elemental composition of a material; it also produces Auger electrons, and Auger electrons can be collected by Auger electron spectroscopy to determine the surface morphology and composition, etc.

If the target is an ultra-thin specimen, some portion of the electrons is transmitted through the specimen and can be collected by a fluorescent screen or a CCD camera. This results in an image of the specimen with its different parts displayed in varied darkness according its density, crystalline phase and orientation, crystal defects, etc. [210]. The TEM thus allows recording significantly high resolution (less than 0.1 nm) images because of the very small De Broglie wavelength [211] of the electrons.

The TEM has many applications providing information on element and compound structure, such as identification of crystalline phase and orientation, determination of crystalline state and structure, quasicrystal structure and orientation, crystal defects, and nanoparticle morphology and size [210,212], thus the TEM is widely used in many fields such as materials science, nanotechnology [165,213].

In this thesis, TEM and high resolution TEM were undertaken using a JEOL 2010 field-emission gun microscope operating at 200kV with a lattice resolution of 0.1 nm.

2.3.2. Characterization techniques for films

2.3.2.1. Thickness determination

A KLA-Tencor P11 surface profilometer was used to measure the resulting polymer films thickness. The profilometer has low force measurement micro-head with a sharp probe tip (2 μm radius, 60 degree's). When carrying out measurement, the profilometer allows tracking the probe tip over the polymer surface and obtaining a height profile. In the case of thickness measurement, a score was made on the film before the measurement. The probe tip scanned over this score to gain the height difference and this difference is the film thickness. Since the inhomogeneity of the film, the accuracy of this measurement is typically ± 5 nm.

2.3.2.2. Integrating sphere photometer for films

Integrating sphere is an instrument which can allow measuring the global photometric coefficients of film samples like transmittance ($\boldsymbol{T}(\lambda)$), total reflectance ($\boldsymbol{R}(\lambda)$, sum of specular and diffuse reflectance). If necessary, diffuse reflectance only is also possible to be measured. In this thesis, the integrating sphere was used to study the optical properties of thin films.

Figure 2. 4 shows the configuration of a typical integrating sphere. The interior of an integrating sphere is covered with a diffuse white reflective coating, barium sulfate ($BaSO_4$) in our case, which has a usefully flat and high reflectance over the visible spectrum, taking advantage of its uniform scattering or diffusing effect (for an ideal integrating sphere, it should be lambertian surface).

An incandescent lamp is used as the light source, which contains the spectral range from about 200 nm to 1700 nm. In addition, the input light beam can be tuned by a diaphragm adjusting to the dimension of the sample.

Several ports are made at the equator of the sphere for light entrance and exit (Figure 2. 4). Port 1 is the light entrance and port 2 and 3 are exits. There is still one more port which is used to trap the specular reflection beam during measurement of diffuse reflectance. In normal measurement, to obtain the total reflectance and transmittance, this port is covered with an object which has the same coating as the interior of the integrating sphere. For reflection measurement, there is an angle of 8 ° between the direction of the incident light beam and the normal direction of the sample surface. In this way, we can avoid the exclusion of the specular reflection beam and measure the total reflectance. An optical fiber connected to the spectrometer at the back side of the sphere is used, allowing detection of the light inside the sphere and the spectrometer is connected to a PC which has a special acquisition software. In principle, a baffle located between the fiber and port 1 is used to prevent light directly traveling from port 1 onto the fiber. In our system, two spectrometers are used for near UV and near infrared and the resolution is 0.1 nm.

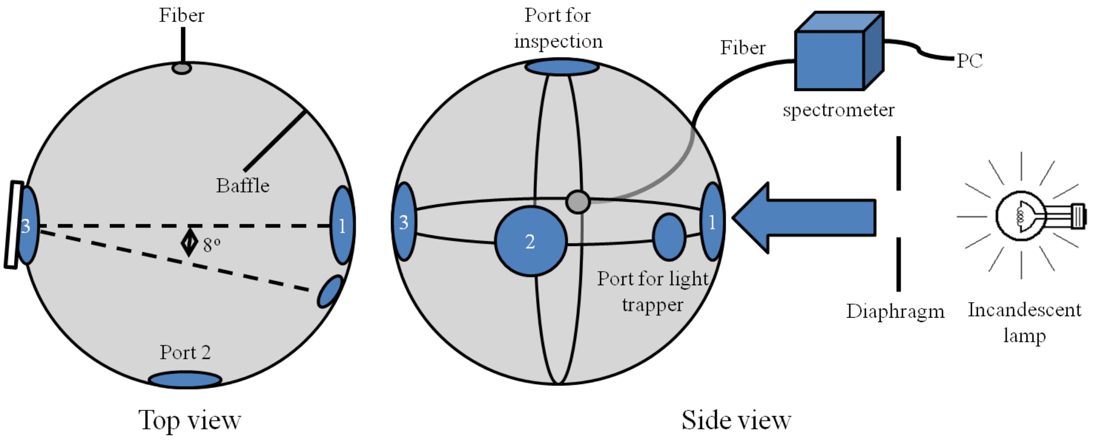

Figure 2. 4 Schematic of an integrating sphere

For the measurement of $\boldsymbol{T}(\lambda)$ and $\boldsymbol{R}(\lambda)$, it contains several steps as follows. First, we measure the noise background signal ($\boldsymbol{I}_0$) which is always observed during the measurement. During this step, the port 1 and 3 are open allowing the exclusion of incident light. Port 2 is covered with an object (the reference, normally has a lambertian surface) which has the same coating as the interior of the sphere. Second step, port 1 is open but port 3 is covered with the reference. Port 2 is covered with the sample. In this way, we obtain the reference result $\boldsymbol{I}_1$. In the third step, for total $\boldsymbol{R}(\lambda)$, port 1 is open, port 2 is covered by the reference, and port 3 is covered with the sample; for $\boldsymbol{T}(\lambda)$, port 2 is open, port 3 is covered with the reference but the sample is placed before the port 1. During this step, we obtain the result from sample ($\boldsymbol{I}_2$). Especially, for diffuse $\boldsymbol{R}(\lambda)$, we should replace the cover of the port by a light trapper to remove the specular refection beam, while the measurement procedure is same as the measurement of total ***R***(*λ*). Finally, we calculate the global photometric coefficients, ***T***(*λ*)) and ***R***(*λ*) as follows:

$$R_{\text{total,diffuse}}(\lambda), T(\lambda) = \frac{I_2(\lambda) - I_0(\lambda)}{I_1(\lambda) - I_0(\lambda)} \qquad \text{Equation 2. 4}$$

Particularly, all the resulting signals are proportional to the intensity of the incident light. They are all in percentage unit. For specular ***R***(*λ*), it is calculated as follows:

$$R_{\text{specular}}(\lambda) = R_{total}(\lambda) - R_{diffuse}(\lambda) \qquad \text{Equation 2. 5}$$

We can also calculate the Absorptance of the sample as follows (the intensity of incident light is normalized to 1):

$$A(\lambda) = 1 - R_{total}(\lambda) - T(\lambda) \qquad \text{Equation 2. 6}$$

In summary, by using integrating sphere, we can obtain the global photometric coefficients of a sample such as Transmittance (***T***(***λ***)), Reflectance (***R***(***λ***)), and then the Absorptance (***A***(***λ***)). These coefficients are useful to study the optical properties of thin films.

In this thesis, a Labsphere RT-060 and an AvaSpec-ULS3648 high-resolution spectrometer for near UV and visible range (200 nm ~ 1100nm) were used to collect signals. The spectrometer was connected to a computer with USB2. Together with acquisition software Avasoft 7.5, we can subsequently obtain the Transmittance (***T***(***λ***)), Reflectance (***R***(***λ***)) spectra.

2.3.2.3. Goniophotometry

Goniophotometry (or goniometric optical scatter measurement) is a technique for measuring the angular intensity distribution of back-scattering and forward-scattering light from diffusive samples (or specular surface) and this distribution is possibly wavelength-dependent. This technique requires an instrument, Goniophotometer, allowing measuring light scattered in the visible and in the near infrared range. Figure 2. 5 shows the Goniophotometer used in this thesis, Reflet 90, provided by STIL Company in France.

The major component of a Goniophotometer consists of an optical bench, a darkroom (not shown), a light box (not shown), an electronic cabinet and a computer with dedicated boards and software (Figure 2. 7). The optical bench is comprised of an illumination system and a detection system which observes at the same point of the sample surface. Two diaphragms in the illumination module allow tuning the incident light spot size and intensity. The incidence angle can also be tuned by rotation of a motorized 1-axis goniometer (Figure 2. 6, rotation angle =θ_i, 0° ≤ θ_i ≤ 90°). The detection system has a motorized 2-axis goniometer (rotation angles = θ_d and φ_d, -90° ≤ θ_d ≤ +90°, -105° ≤ φ_d ≤ +105°), allowing symmetric rotating in two axes (Figure 2. 6). For the goniometer, the angular resolution is 0.1 °and positioning precision is 0.5 °. The optical bench is mounted inside a darkroom to prevent light from surrounding environment. Light source is supplied by a tungsten halogen lamp mounted in a light box. The electronic cabinet is used to control the motion of the optical bench and for power supply. The REFLET operating software installed in a computer is used for data acquisition.

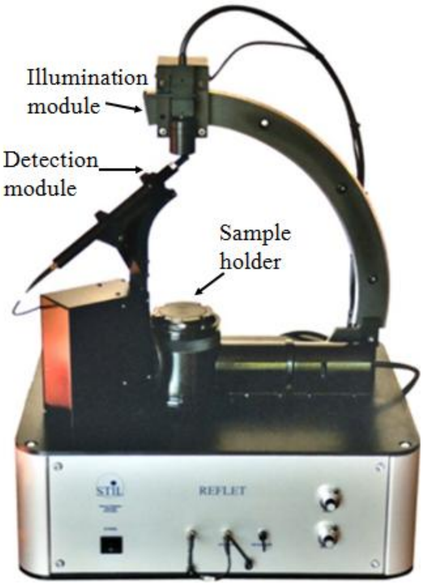

Figure 2. 5 Photogragh of optical bench and electronic cabinet of Reflet 90

The raw result data are proportional to the incident light intensity. This result is relative to some standard. To obtain an absolute measurement, a lambertian standard is used. Then we use the Bidirectional Reflectance Distribution Function (BRDF) to study quantitatively the reflectance behavior of the non-lambertian sample surface by the variation of direction of view. BRDF can be derived from the raw result data obtained from Goniophotometer. The BRDF is defined by the CIE (Commission Internationale de l'Eclairage) as follows:

$$BRDF(\theta_d,\varphi_d,\theta_i,\varphi_i) = L(\theta_d,\varphi_d)/E_0(\theta_i,\varphi_i) \qquad \text{Equation 2. 7}$$

where $\boldsymbol{L}(\theta_d, \varphi_d)$ is the sample luminance in the direction (θ_d, φ_d), $\boldsymbol{E}(\theta_i, \varphi_i)$ is the illuminance on the sample surface in the direction (θ_i, φ_i). The units of $\boldsymbol{L}(\theta_d, \varphi_d)$, $\boldsymbol{E}(\theta_i, \varphi_i)$ and BRDF are, respectively: candela/m^2, lux, sr^{-1}.

In our case, the φ_i is zero and θ_i is set to be 8 °, and the BRDFs are obtained from a lambertian normalization mode using the REFLET operating software (Figure 2. 7): we first choose

“BRDF” measurement type in the “Tools” window, the “File” for “signal source”, and the “Lambertian” for “normalization type”. We then enter the data file obtained from sample and lambertian standard, finally calculate and save the resulting BRDF data.

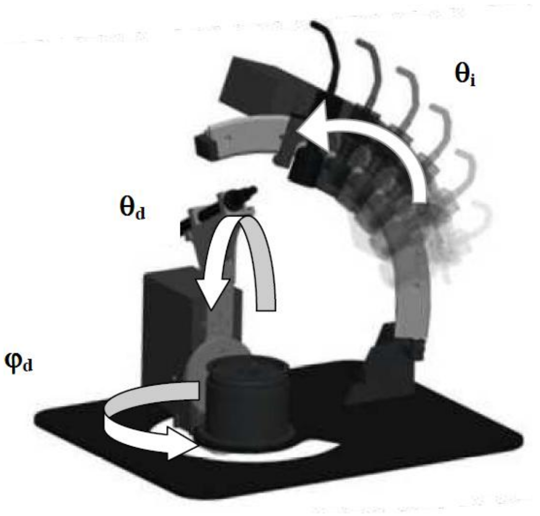

Figure 2. 6 Rotation axes of Goniophotometer (θ_d = zenith detection angle, φ_d = azimuth detection angle, θ_i = illumination zenith angle).

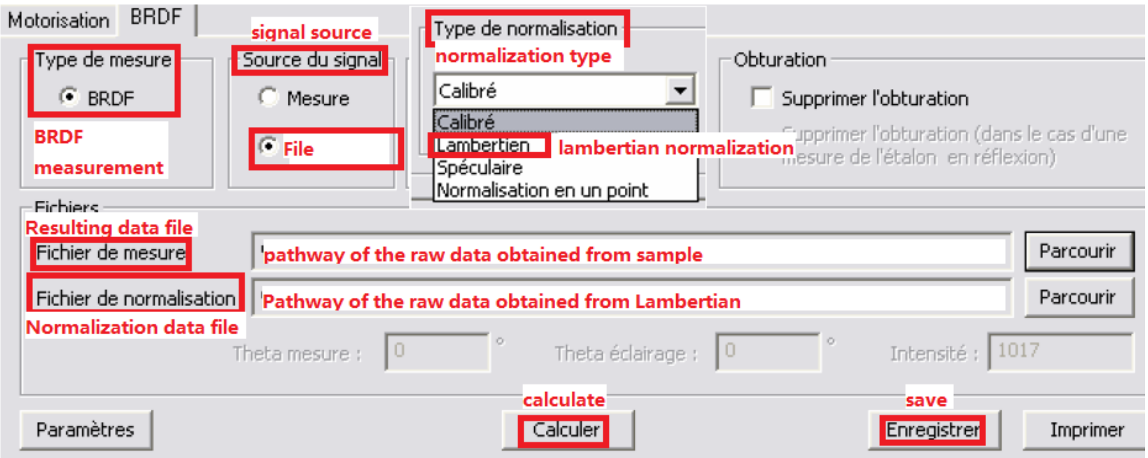

Type de mesure
● BRDF

Source du signal
○ Mesure
● File

Type de normalisation
Calibré
Calibré
Lambertien
Spéculaire
Normalisation en un point

Obturation
☐ Supprimer l'obturation
Supprimer l'obturation (dans le cas d'une mesure de l'étalon en réflexion)

Fichiers
Fichier de mesure: 'pathway of the raw data obtained from sample
Fichier de normalisation: 'Pathway of the raw data obtained from Lambertian
Theta mesure : 0 °
Theta éclairage : 0 °
Intensité : 1017

Figure 2. 7 BRDF page of REFLET operating software

2.3.2.4. *Atomic Force Microscopy and conductive Atomic Force Microscopy*

Atomic force microscopy (AFM) is a common technique to investigate surface morphologies. Figure 2. 8 shows the general components of the AFM. The AFM consists of a cantilever and a sharp tip attached to the end of the cantilever. This tip is scanned across a sample during the measurement. The tip has a radius of curvature on the order of nanometers. A laser and photodiode are used to monitor the deflection variation of the cantilever caused by the forces developed between the tip and the sample. For the AFM measurement, there are 3 primary imaging modes, according to the nature of the tip motion: contact mode, tapping mode, and non-contact mode. In this thesis, the tapping mode is chosen to study the polymer film surfaces.

In the tapping mode, the cantilever is oscillated at its resonant frequency and the oscillation amplitude is maintained constant using a feedback loop. When the tip comes closer to the sample surface, the tip-surface interaction results in a decrease in the amplitude. In order to keep the amplitude a constant, the feedback mechanism adjusts the cantilever height as the cantilever is scanned over the sample. The movement of the cantilever is detected by the laser beam and photodiode detection system and a high-resolution height profile image is obtained.

In order to study the effect of surface morphology on the electrical property of thin films, on the same sample region we also performed condutive AFM (C-AFM) characterizations. The C-AFM usally uses contact mode and a conductive tip together with a cantilever to measure the conductivity of a sample [214–217]. The C-AFM image is associated with the surface profile of the same sample region allowing studying the correlation of the topography and electrical conductivity.

The AFM and C-AFM images in this thesis were obtained by CSI Nano-Observer AFM from the company ScienTec. For the C-AFM, a Resiscope II electrical module was attached to the CSI Nano-Observer AFM and a DC bias was applied between the sample and a conductive AFM probe (tip at virtual ground). The contact mode was used. The resistance range of Resiscope II electrical module is between $10^2\ \Omega$ and $10^{12}\ \Omega$, and current range is between 100 fA and 1 mA.

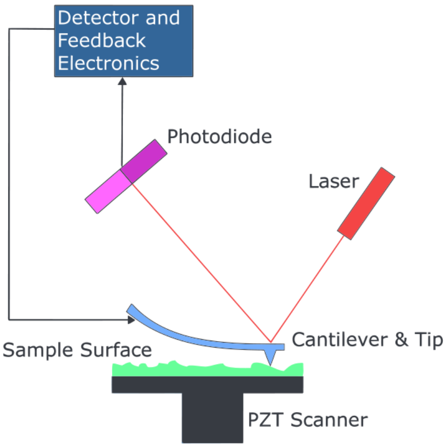

Figure 2. 8 Block diagram of atomic force microscope using beam deflection detection [218].

2.3.2.5. Four point probe measurement

A four point probe is a very simple setup allowing easy and quick measurement of the surface resistance of thin semiconductor film specimens. The operating principle is presented below (Figure 2. 9).

For a very thin and quasi-infinite film (thickness ***t*** << ***s***), by applying a current through two outer probes, we get current rings rather than spheres. Hence, for the area $A = 2\pi xt$, the deviation of expression of resistance is as follows:

$$R = \int_{x_1}^{x_2} \rho \frac{\mathrm{d}x}{2\pi xt} = \int_{s}^{2s} \frac{\rho}{2\pi t} \frac{\mathrm{d}x}{x} = \frac{\rho}{2\pi t} \ln 2 \qquad \text{Equation 2. 8}$$

Where ***R*** is the resistance, ***ρ*** is the resistivity, ***s*** is the probe spacing, ***t*** is the film thickness. Due to the superposition of current at the outer two tips, $R = V/2I$, the resistivity is:

$$\rho = \frac{\pi t}{\ln 2} (\frac{V}{I}) \qquad \text{Equation 2. 9}$$

where the ***I*** is the current applied through the outer probes and the ***V*** is voltage through the inner probes which are measured by instruments. Finally, the sheet resistivity $R_{sheet} = \rho/t$ for the semi-infinite thin film can be expressed as:

$$R_{sheet} = \frac{\pi}{\ln 2} (\frac{V}{I}) = 4.53 (\frac{V}{I}) \qquad \text{Equation 2. 10}$$

In this thesis, sheet resistance (Ω/square) was obtained from Cascade 4-point probe (CASCADE MICROTECH C4S-67 PROBE) together with a Keithley 238 source measurement unit and a Keithley 199 system digital multimeter scanner (for measuring the voltage).

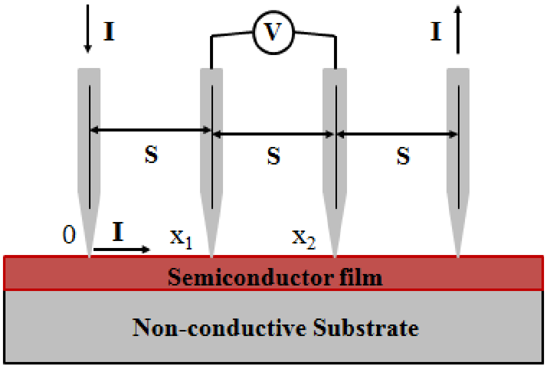

Figure 2. 9 Schematic of 4-point probe configuration, s = 1 mm for CASCADE MICROTECH C4S-67 PROBE

2.3.3. Characterization techniques for solar cells

In order to evaluate the performance of solar cells, the current-voltage and external quantum efficiency characterization were performed.

2.3.3.1. Current-Voltage Characterization

This technique allows measuring the current as a function of input voltage by applying a bias to the solar cell. Figure 2. 10 shows the equivalent circuit diagram of a solar cell. When a solar cell is connected to an external voltage source (in the red color) which applies a bias voltage, we can obtain the correlation between the current and bias voltage, both in dark and under illumination.

In this thesis, we used a solar simulator to generate an illumination in the condition of AM1.5 (1000 W/m^2, see Figure 1. 9), a Keithley 2700 to measure the current and Keithley 2000 to measure electric tension. The external voltage was supplied by an Agilent 3640A programmable DC power supplies. The measurements were carried out in an ambient enviroment at 27 ℃. As a result, we would obtain the figures of current as a function of bias voltage like Figure 1. 24.

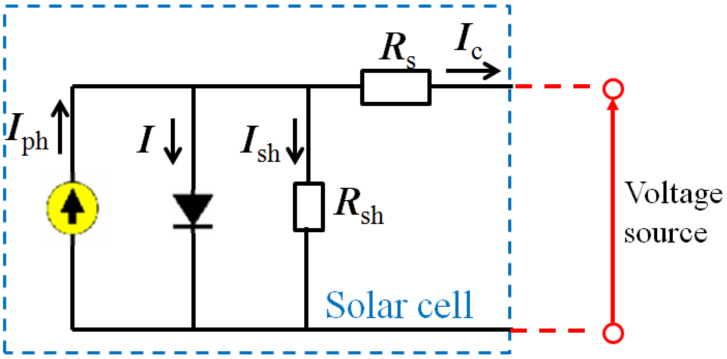

Figure 2. 10 The equivalent circuit diagram of a solar cell (the part inside the blue dash line)

2.3.3.2. External quantum efficiency

The external quantum efficiency (*EQE*) is the ratio between the number of charge carriers ($\boldsymbol{N_e}(\lambda)$) collected by the solar cell to the number of photons ($\boldsymbol{N_{ph}}(\lambda)$) of a given energy incident on the solar cell (Equation 1. 5). While the number of charge carriers ($\boldsymbol{N_e}(\lambda)$) collected by the solar cell is given by Equation 2. 11:

$$N_e(\lambda) = \frac{J_{sc}(\lambda)}{e} \qquad \text{Equation 2. 11}$$

and the number of photons ($\boldsymbol{N_{ph}}(\lambda)$) of a given energy incident on the solar cell:

$$N_{ph}(\lambda)=\frac{P_i(\lambda)}{E_{ph}(\lambda)}=\frac{\lambda P_i}{hc}$$ Equation 2. 12

Then we get

$$EQE(\lambda)=\frac{hc}{\lambda e}\frac{J_{sc}(\lambda)}{P_i(\lambda)}$$ Equation 2. 13

Where the $\boldsymbol{J}_{\mathrm{sc}}(\lambda)$ is the current collected from a testing device and $\boldsymbol{P}_{\mathrm{i}}(\lambda)$ is the incident power, $\boldsymbol{E}_{\mathrm{ph}}(\lambda)$ is the energy of a photon, λ is the wavelength, ***h*** is Planck constant, ***c*** is the speed of light in vacuum, ***e*** is the elementary charge. In practice, A silicon photodiode which has spectral response ($\boldsymbol{S}^{ref}(\lambda)$, in unit of A/W, Equation 2. 14) is uswd as a reference.

$$S^{ref}(\lambda)=\frac{J_{sc}^{ref}(\lambda)}{P_i(\lambda)}$$ Equation 2. 14

Finally we get

$$EQE(\lambda)=\frac{hc}{\lambda e}\frac{S^{ref}(\lambda)}{J_{sc}^{ref}(\lambda)}J_{sc}(\lambda)$$ Equation 2. 15

Where $S^{ref}(\lambda)$ and $J_{sc}^{ref}(\lambda)$ can be obtained from a reference photodiode, $J_{\mathrm{sc}}(\lambda)$ is obtained from the sample.

The setup used in this thesis for external EQE measurement is shown in Figure 2. 11. We used an ASB-XE-175 Xenon Fiber Optic Light Source to generate a spectrum from UV to near infrared (200 nm ~ 1180 nm). A monochromatic spectrum was obtained behind a DK240 1/4 meter monochromator (provided by Spectral Products) and then modulated by a chopper. A filter for visible spectrum (400 nm~ 750 nm) was used to avoid UV and near infrared light. A low-noise current preamplifier (Model SR570, provided by Stanford Research Systems, Inc.) was used to amplify and covert the small current signal into a voltage signal. This signal is then measured by a lock-in amplifier (Model SR810 DSP lock-in amplifier, provided by Stanford Research Systems, Inc.) locked to the frequency of the chopper.

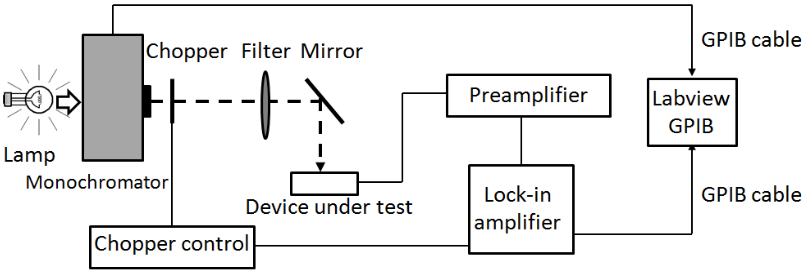

Figure 2. 11 Schematic of external quantum efficiency measurement

2.4. Conclusion

In this chapter, we introduced the main materials used in this thesis, for Ag nanoparticles synthesis and for solar cell fabrication.

We also presented the methods used to prepare polymer thin films and organic solar cells. We use spin coating method to obtain ultrathin and uniform polymer films. The spin coating method was also applied in the solar cell fabrication. The fabrication process of films and organic solar cells was introduced in details.

Characterization techniques of UV-visible absorption spectroscopy, x-ray diffraction and TEM for Ag nanoparticles solution and the Ag nanoparticles themselves were presented as well. By using these techniques, we can study the localized surface plasmon resonance of the Ag nanoparticles in solution and characterize the shape, size and crystalline structure Ag nanoparticles.

Characterization techniques for thin films were highlighted in this chapter, such as integrating sphere, goniophotometry, AFM and C-AFM, and four-point-probe measurement. These techniques allow us to investigate the structural, optical and electrical properties of thin films.

In the end, we introduced two characterization techniques for organic solar cells: current-voltage and external quantum efficiency characterizations. These two techniques allow us to evaluate the performance of solar cells and as well as the solar cells’ spectral response.

Chapter III

Structural, optical and electrical properties of PEDOT:PSS thin films doped with silver nanoprisms

3.1. Introduction

Over the last two decades, metal-polymer nanocomposites, metallic nanoparticles embedded in conducting polymer matrix, have attracted much attention due to their tunable magnetic, mechanical, electrical or optical properties [219–221]. These promising properties enable them to be applied in many applications such as sensors [222], light emitting diodes [223], capacitors [224] and particularly in solar cells [225]. Among various metal-polymer nanocomposites, there is significant interest in recent years on the properties of poly(3,4-ethylenedioxythiophene):poly(styrenesulfonate) (PEDOT:PSS) and their mixture with silver nanoparticles. PEDOT:PSS is a conductive polymer. Due to its suitable work function and beneficial effects in surface roughness [86,226], it is commonly used as a buffer layer between the anodic electrode and the organic photoactive layer in the fabrication of organic solar cells [59–61]. Instead of inserting sub-wavelength-dimension Ag nanoparticles (Ag NPs) inside the photoactive layer [227,228], their incorporation into PEDOT:PSS films has been found to enhance the absorption of the composite in the visible spectrum due to localized surface plasmon resonance (LSPR) [188,229,230]. In addition to absorption, light scattering [61,230] in this case was also found to increase which can be beneficial for light-trapping in the photoactive layer. It has been also reported that the incorporation of Ag NPs in PEDOT:PSS can effectively improve the conductivity of PEDOT:PSS [196,231,232] and increase the surface roughness [61,225]. Combining all these beneficial effects in optical, electrical, and structural properties, hybrid Ag-nanoparticle-PEDOT:PSS thin films are of high potentials for organic solar cells towards better photovoltaic performance [61,83,225,233,234].

In order to explore the implications of the localized surface plasmon resonance of noble metal nanoparticles in applications such as organic solar cells, in this chapter, we synthesized colloidal Ag nanoprisms (NPSMs) and fabricated a series of hybrid Ag-NPSM-PEDOT:PSS films containing various amount of Ag NPSMs. While compared to spherical Ag nanoparticles (NPs), Ag NPSMs exhibit LSPR with a wider wavelength tunability window from the visible to the near-IR regions [235]; Despite this attractive LSPR tunability, the incorporation of Ag NPSMs in PEDOT:PSS has not been explored so far. After that, a series of structural, optical, and electrical characterizations were performed on Ag NPSMs and Ag-NPSM-PEDOT:PSS hybrid thin films by various techniques including transmission electron microscopy (TEM), optical absorption measurement, goniophotometry, regular and conductive atomic force microscopy (C-AFM), and four-point-probe resistance measurements. In particular, goniophotometry allows quantitative surface reflectance studies and the calculation of Bidirectional Reflectance Distribution Functions (BRDF) of sample surfaces, which are likely to be non-Lambertian diffuse surfaces [236]. Through analyzing the BRDF results of different hybrid films, we compared among different hybrid films the proportions of light being reflected and absorbed over various reflected angles.

Comparing the results from these characterization techniques, we study how the structural, optical and electrical properties of these hybrid films are modified by different concentrations of Ag NPSMs, shedding light on their perspectives in organic solar cells towards enhanced photovoltaic performance.

3.2. Ag NPSM synthesis and characterizations

There many methods and techniques to synthesize silver and gold nanoparticles, such as chemical reductions through $AgNO_3$ reduced by heating PEG (Polyethylene glycol) [237] or EG (ethylene glycol) [238] or by $NaBH_4$ [239] and Hydrazine [240], sonochemical deposition [241,242] or through nanostructured templates [243,244], gas condensation [245,246], laser irradiation [196,247], and as well as photochemical methods [248,249]. Moreover, the synthesis can achieve a variety of shapes, including spheres [237,250], rods [251,252], wires [137,253,254], disks [255–257], cubes [258,259], shells [260], and prisms [165,261] with varying optical properties. Among these structures, the nanoprisms have attracted much attention from scientists because they display LSPR with a wider wavelength tunability window from the visible to the near-IR regions. In addition, they can be synthesized with high yield and can be easily functionalized with sulfur-containing adsorbates [165,235,262].

To achieve nanoparticles of nanoprism morphology, in general, there are two routes: thermal (chemical reduction) and photochemical routes. In the photochemical approach, Ag nanospheres are initially formed. Then they anisotropically grow into nanoprisms by the assistance of surface plasmon excitations induced by laser irradiation. The surface plasmon excitations lead to a redistribution of charges on the surface which further results in the ligand dissociation and face-selective Ag^+ reduction at the sites where there is plasmonic-enhanced electric field. As a result, this face-selective reduction leads to the face-selective growth of nanoprisms [37,53]. This synthesis approach is reliable and efficient offering good tunability of the aspect-ratio (the ratio of edge length to thickness) depending on the irradiation wavelength. However, this photo-mediated growth method is time-consuming, typically taking 50 ~ 70 hours [37,53]. On the other hand, some thermal approaches are also efficient ways to synthesize Ag NPSMs. Thermal approaches allow modest control over particle size but they are relatively rapid (within several tens of minutes) and reproducible [165,239]. Generally speaking, in these syntheses, Ag NPSMs are produced under mild conditions, *i.e.* at room temperature and using water as the solvent.

3.2.1. Ag NPSMs synthesis

The Ag NPSMs used in this work were prepared using a thermal approach, following the seeded growth method from Aherne *et al* [165].

In this synthesizing recipe, there are two steps: seed production and nanoprism growth. First, the seeds were synthesized by adding an aqueous silver nitrate solution ($AgNO_3$, 5 mL, 0.5 mM; 2 mL/min) into a freshly prepared mixture of trisodium citrate ($Na_3C_6H_5O_7 \cdot 2H_2O$, 5mL, 2.5mM), poly(sodium styrenesulphonate) (PSS, 1,000 kDa, 0.25mL) and sodium borohydride (NaBH4, 0.3 mL, 10 mM; reducing agent) under vigorous stirring. The chemical equation for this reduction process could be expressed as follows [263]:

$$AgNO_3 + NaBH_4 \rightarrow Ag^0 + \frac{1}{2}H_2 + \frac{1}{2}B_2H_6 + NaNO_3$$

Second, the Ag NPSMs were produced by slowly adding $AgNO_3$ (5 mL, 0.5 mM; 1 mL/min) into a mixed solution containing de-ionized water (5 mL), ascorbic acid ($C_6H_6O_6$, 75 µL, 10 mM; reducing agent) and different quantities of the seed solution: 500 µL, 650µL, 1000µL and 2000µL, respectively. The mechanism of this reduction reaction is [264,265]:

$$2AgNO_3 + C_6H_8O_6 \rightarrow 2Ag^0 + C_6H_6O_6 + 2HNO_3$$

Finally, another aqueous trisodium citrate solution (0.5 mL, 25 mM) was added into the above solution to stabilize Ag NPSMs. De-ionized (DI) water instead of distilled water was used throughout the entire preparation.

Here PSS plays a complex role in the direction-selective growth through preferential adsorption onto certain Ag facets and through influencing the defect structures [165]. Citrate cannot only stabilize the nanoparticles but also direct the anisotropic growth of nanoprisms [165,239]. Normally, nanoparticles have large interfacial energy (γ) and many dangling bonds due to their small dimensions. This leads to aggregation of nanoparticles. Such aggregation can possibly be prevented by the addition of stabilizers. For citrate, it can form two Ag-O bonds with the Ag(110) surface or four Ag-O bonds with the Ag(111) surface [266]. Therefore, when citrate is attached on the surface of nanoparticles it acts as a stabilizer to prevent agglomeration. Moreover, the binding energy of Ag-O bond for Ag(111) surface is higher than that for Ag(100) surface [266]. This leads to the growth of nanoparticles along <111> directions. With the combination of PSS and citrate, anisotropic nanoparticles were prepared.

Ag nanospheres were also synthesized by the reduction of $AgNO_3$ by PEG (Polyethylene glycol) under heating [237]. Experimental details by this method are listed in the Appendix I. In addition, Ag NPSMs were also produced by the one-step thermal reduction method [239]. This is a simplified method but the nanoprism aspect-ratio cannot be easily controlled. Experimental details by this method are listed in Appendix II.

3.2.2. Characterizations of Ag NPSMs

Figure 3. 1 shows the TEM images of the resulting Ag seeds and Ag NPSMs synthesized using different volumes of seed solution, 2000 μL, 1000μL, 650μL and 500μL, respectively. The seeds show an average diameter of 3 ~ 4 nm. The nanoparticles prepared by using 2000μL seed solution display various shapes. When the volume of seed solution decreases, we obtained nanoprisms of increased dimension (characterized by TEM). The Ag NPSMs obtained from 500μL seed solution have an average edge length of about 20 nm with some spherical Ag particles remaining. The average thickness of Ag NPSMs is estimated to be around 5 nm (Figure 3. 2).

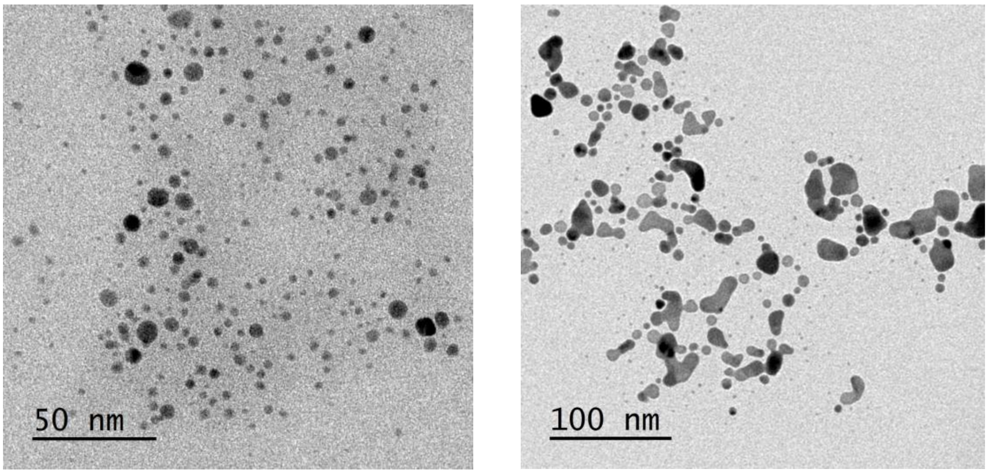

a) Seed

b) 2000 μL

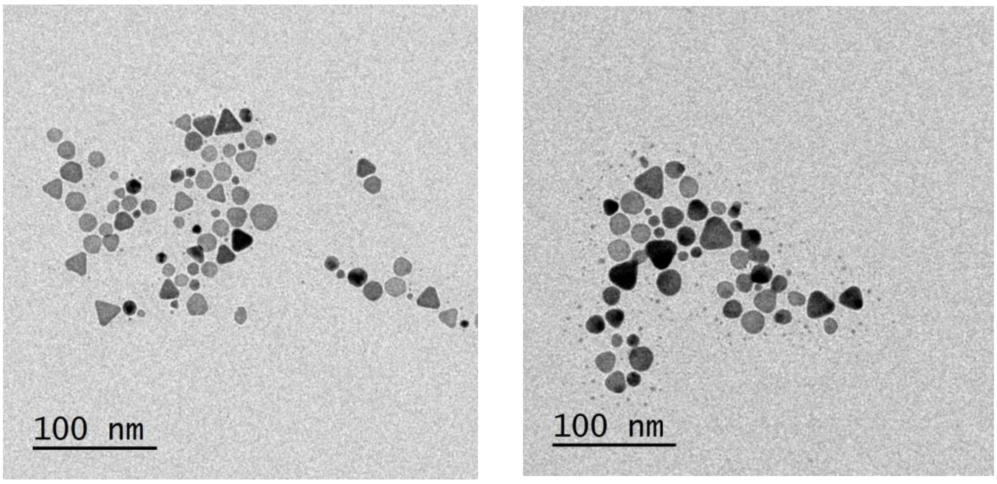

c) 1000 μL

d) 650 μL

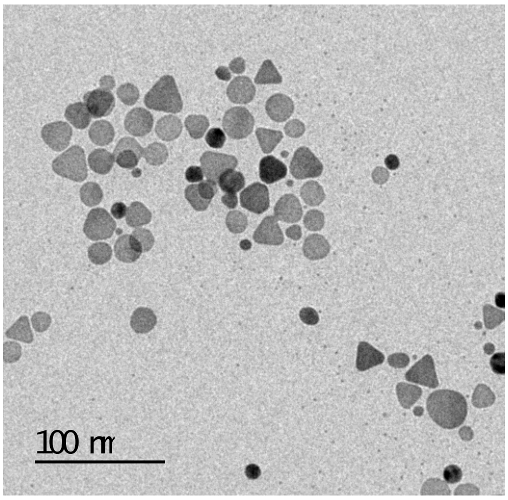

e) 500 μL

Figure 3. 1 TEM images of Ag NPSMs synthesized from different volumes of seed solution

Figure 3. 3 shows the XRD diffraction pattern of silver nanoprisms. To apply X-ray diffraction on silver nanoprisms, some drops of silver nanoprisms solution were cast on a silicon wafer. The instrument Philips X'PERT MPD was used to obtain XRD patterns. As shown in Figure 3. 3, there are three peaks at around 38°, 44° and 66° (2θ), which are assigned to the (111), (200) and (220) reflections of FCC silver (JCPDC card No 04-0783) according to their positions and intensities. The strong (111) reflection suggests that metallic silver particles, crystallized in FCC structure, were successfully synthesized.

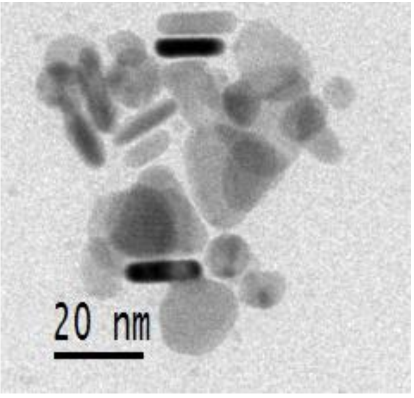

Figure 3. 2 TEM image of Ag NPSMs synthesized from 650 μL seed solution by the same procedure. There are nanoprisms standing vertically on their edges by which we measured the thickness to be 4 ~ 5 nm.

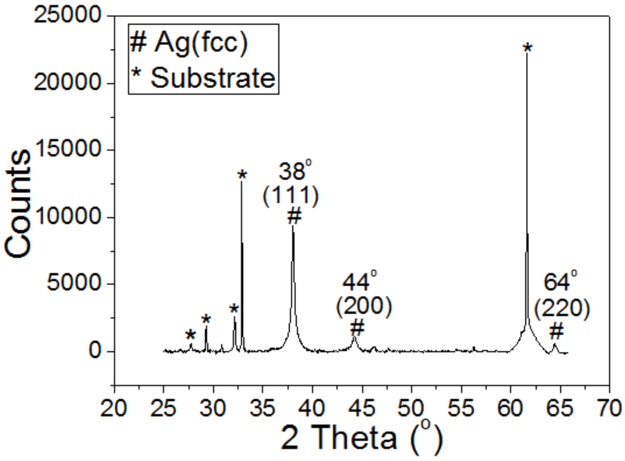

Figure 3. 3 XRD pattern of silver nanoprism, showing strong Bragg reflections corresponding to FCC metallic silver

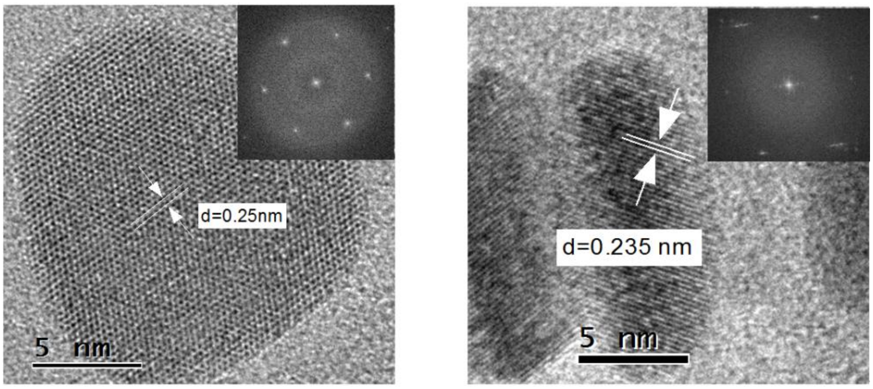

Figure 3. 4 Left figure: High resolution TEM image of a flat-lying Ag NPSM. Right figure: High resolution TEM image of Ag NPSMs standing on their edges. Insets: the corresponding fast Fourier transform of the image.

Figure 3. 4 shows the high resolution TEM images of a flat-lying Ag NPSM (left figure) and a few Ag NPSMs standing on their edges (right figure). A spacing of 0.235 nm can be measured in the right figure of Figure 3. 4 which corresponds to the periodicity of the {111} planes in FCC silver. Besides this lattice spacing, the thickness of the Ag NPSMs was measured to be abound 5 nm (see Figure 3. 2 and Figure 3. 4). The left figure exhibits a spacing of 0.250 nm which can corresponds to the periodicity observed along <111> directions. This spacing has been associated with the formation of stacking faults according to previous studies [165].

To obtain the basic optical properties of Ag NPSMs, a series of UV-Vis absorbance spectra were performed on as-synthesized Ag NPSM solutions (Figure 3. 5). Different batches of Ag NPSMs were obtained with the use of different amounts of seed solution during synthesis. While the thickness of Ag NPSMs is not sensitive to the amount of seed solution used, their final edge lengths increase as the amount of seed solution decreases. All spectra exhibit three characteristic absorbance peaks: The first two are located at 340 nm and 400 nm, corresponding to the out-of-plane quadrupole and dipole LSPR bands, respectively [233]. These two peaks remain unchanged when the edge-length of Ag NPSM increases, suggesting unchangeable in thickness. In addition, there are main LSPR absorbance peaks due to in-plane dipole resonance [165,233] which is increasingly red-shifted (from 400 nm to 560 nm) as the aspect-ratio (between the edge-length and the thickness) increases. These optical properties are coherent with those published on similar Ag NPSMs [165,239]. However, the intensity of the peak at 400 nm decreases with the increasing red-shifted in-plane LSPR. This decrease could be attributed to the decreasing amount of Ag nanospheres (seeds), which have also a peak at 400 nm [267], in Ag NPSM solutions, as seen in Figure 3. 1. The inset of Figure 3. 5 shows the TEM image of a flat-lying Ag NPSM which has an in-plane LSPR band located at 560 nm.

Despite some polydispersity existing on their dimensions, the majority of them show an edge-length of about 20 nm.

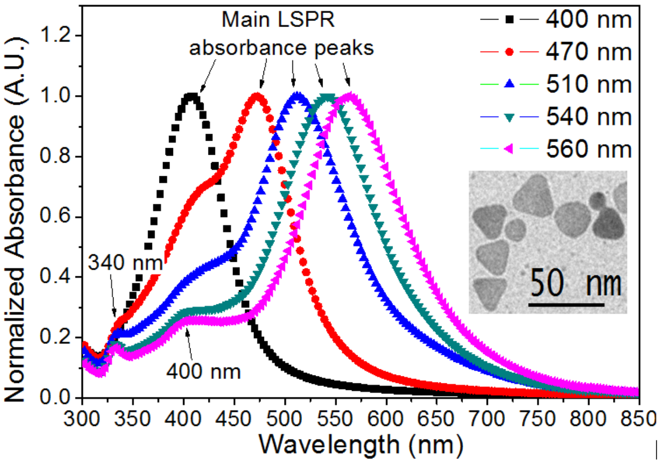

Figure 3. 5 Normalized solution UV-Vis absorbance spectra of Ag NPSMs synthesized from different volumes of seed solution: black square- seeds only; red circle- 2 mL; blue up triangle - 1mL; dark cyan down triangle - 650 μL; pink left triangle - 500 μL. The use of different amount of seed solution leads to different batches of Ag NPSMs of different edge-length/thickness aspect-ratios. Inset: TEM image of flat-lying Ag NPSMs which have an in-plane LSPR band at 560 nm.

In brief summary, we synthesized a series of Ag NPSMs of similar thickness but of different edge length. By tuning the aspect-ratio between the edge length and the thickness, these different batches of Ag NPSMs exhibit a main in-plane LSPR peak at different wavelength in the visible spectrum.

3.3. Hybrid PEDOT:PSS-Ag NPSM solutions and films

3.3.1. Preparation of hybrid PEDOT:PSS-Ag NPSM solutions and films

The Ag NPSM solution (10 mL) was centrifuged at 6,000 rpm for 15 minutes by using tetrahydrofuran (THF, about 35 mL) as the non-solvent (the Ag NPSMs have low solubility in THF). A pellet of Ag NPSM precipitate was obtained at the bottom of the centrifuge tube and the supernatant was removed. The pellets were re-dissolved in 0.5 mL DI water and then mixed with 0.5 mL PEDOT:PSS solution (Heraeus CleviosTM P) by ultrasonic bath (40 kHz for 40 minutes). We then obtained a series of hybrid PEDOT:PSS-Ag NPSM solutions of different Ag NPSM concentration: 0.6 mg/mL (with 4 pellets of Ag NPSM precipitate), 1.6 mg/mL (10 pellets) and 2.6 mg/mL (16 pellets).

Glass substrates (VWR Microscope slides, 2.5 cm by 2.5 cm) and ITO-coated glass substrates (1.2 cm by 0.7 cm, for conductive AFM measurement) were cleaned following the substrate cleaning procedures introduced in Section 2.2.2.1. A series of pristine and hybrid PEDOT:PSS thin films with a thickness of about 40 nm was obtained by spin-coating. After spin-coating, all films were subsequently annealed inside a N_2-filled glovebox at 230 ℃ for 30 minutes (the annealing temperature and duration was the optimization result of Section 4.1.2.1 in Chapter IV).

3.3.2. Characterizations of hybrid PEDOT:PSS films

To study the optical properties of hybrid Ag NPSM-PEDOT:PSS thin films, their Absorptance and Bidirectional Reflectance Distribution Functions (BRDF) were investigated.

3.3.2.1. Absorptance

We selected the batch of Ag NPSMs which exhibit a main solution LSPR band at 560 nm and we applied these NPSMs to fabricated hybrid Ag-PEDOT:PSS films. NPSM solution of different concentrations of 0.6 mg/mL, 1.6 mg/mL and 2.6 mg/mL were respectively used to formulate different hybrid films containing different amount of Ag NPSMs. Figure 3. 6 shows the Absorptance spectra of these hybrid films. Compared to the solution absorbance spectra shown in Figure 3. 5, the thin film Absorptance of Ag NPSMs exhibited significant LSPR band broadening and blue-shift which likely originates from NPSM aggregation as well as the shortening of edge length due to PSS etching [268,269]. Compared to pristine PEDOT:PSS films, there are new absorption bumps in hybrid films in the wavelength range between 450 nm and 600 nm which are associated with the addition of Ag NPSMs. This figure also shows that the overall Absorptance of hybrid films increases with larger amount of Ag NPSMs used.

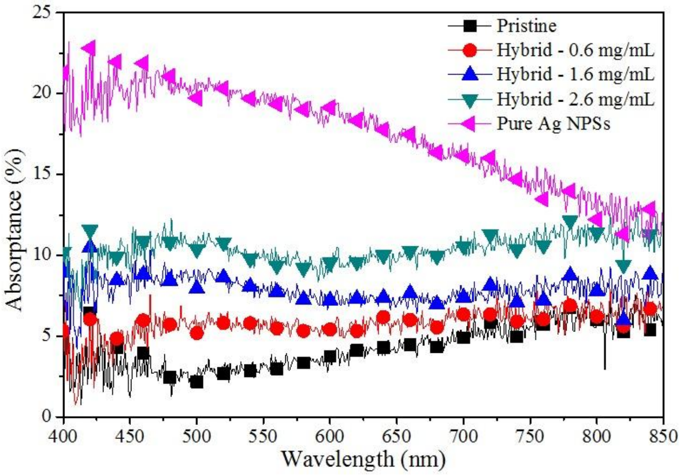

Figure 3. 6 Absorption spectra of pure Ag NPSM film, pristine and hybrid PEDOT:PSS films fabricated using different Ag NPSM concentrations. The pure Ag NPSM film was prepared using the method reported in the reference [270].

3.3.2.2. Bidirectional Reflectance Distribution Function (BRDF)

BRDF can describe quantitatively the reflectance behavior of a non-lambertian surface by the variation of direction of view. In this work, BRDF is used to study the optical scattering properties of hybrid Ag NPSM-PEDOT:PSS thin films.

Figure 3. 7 shows the difference of BRDF (ΔBRDF) between different hybrid Ag NPSM-PEDOT:PSS films and the pristine PEDOT:PSS film in both the in-plane (the incident light plane) and the out-of-plane directions. As shown in the in-plane ΔBRDF (left figure of Figure 3. 7), at 8 ° which is the specular reflection direction, the specular reflection dominates and the intensity increases with increasing Ag NPSM concentration. Except for the specular reflection feature, there is a remarkable resemblance between the in-plane and the out-of-plane *ΔBRDF* for each hybrid film suggesting film uniformity. In low-angle regions such as (-14 ° to 3 °) and (13 ° to 30 °) for the in-plane configuration and (-20 ° to 20 °) for the out-of-plane configuration, due to the constant amount of total incoming light, lower *ΔBRDF* values are observed on samples where more light is reflected or scattered at other angles. For pure Ag NPSM films, Ag absorption dominates in this angular region while for hybrid films their *ΔBRDF*s contain the compromise between Ag absorption and scattering. In high angle regions, such as (-90 ° to -14 °) and (30 ° to 90 °) for the in-plane configuration and (-90 ° to -20 °) and (20 ° to 90 °) for the out-of-plane configuration, the portion of light scattered by Ag NPSMs becomes larger and larger as the angle increases and this becomes the dominant feature of the spectra. Comparing hybrid films of different NPSM concentrations, the greater the Ag NPSM concentration is, the higher the ΔBRDF increasing rate towards high angles. Such increased scattering is believed to be beneficial for the light harvesting in organic solar cells.

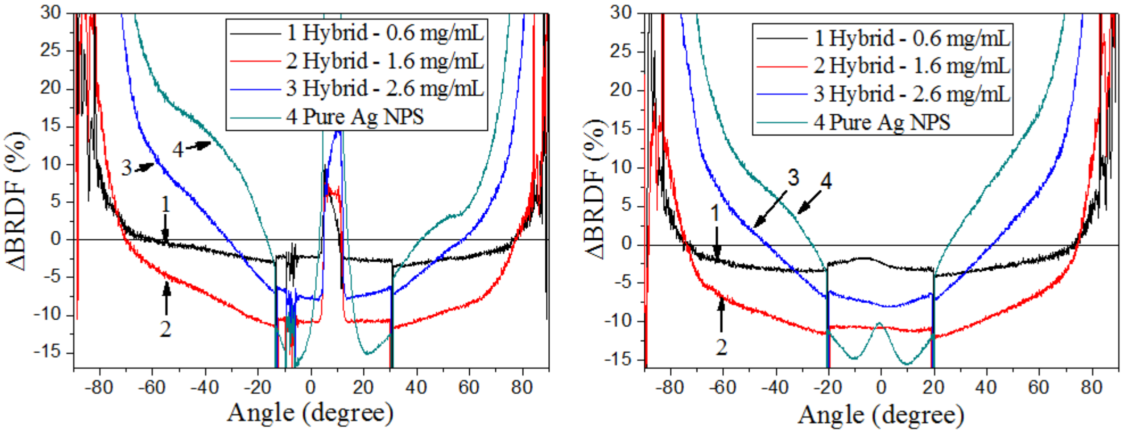

Figure 3. 7 In-plane (in the incident light plane, named as in-plane) ΔBRDF (left) and out-of-plane (in the plane perpendicular to the incident plane) ΔBRDF (right) obtained from hybrid PEDOT:PSS films with various Ag NPSM concentrations.

3.3.2.3. Surface profile and electrical conductivity

In order to study the surface morphology and electrical properties, we performed AFM and conductive AFM characterizations (CSI Nano-Observer AFM with Resiscope II electrical module) and four-point-probe resistance measurements on hybrid PEDOT:PSS films containing different Ag NPSM concentrations.

AFM height images (Figure 3. 8) show increased film roughness associated with the increased Ag NPSM concentration in PEDOT:PSS. On these images there are visible bright spots of various dimensions corresponding to individual Ag NPSM and agglomerates of multiple NPSMs. The formation of agglomerates is difficult to prevent in the method we used to produce these hybrid films [221]. Such nanoparticle agglomeration leads to areas of larger heights compared to the average thickness of the film and increased film roughness.

On the same sample region we also performed C-AFM characterizations (Figure 3. 8). For each hybrid film the bright spots appeared in AFM correspond well to regions of low local resistance observed in C-AFM. The observed local resistance reduction is believed to originate from the metallic nature of Ag NPSMs and their agglomerates or from regions where Ag NPSMs forming chemical bonds with the sulfur atoms of PEDOT:PSS [196]. Such bonding formation can lead to a replacement of the insulating PSS by Ag NPSMs and thus reduce the local resistance [196]. Except for these local low-resistance regions, increased global resistance is however observed when the concentration of NPSM increases in other regions possibly corresponding to the organic matrix. As a result, the overall film resistance becomes higher and higher as the amount of NPSM increases.

This is consistent with our sheet resistance measurements on these pristine and hybrid films by the 4-point-probe technique (Figure 3. 9): the sheet resistance of hybrid PEDOT:PSS films increases with increasing Ag NPSM concentration. This may originate from the insulating PSS polymers contained in Ag NPSM solutions since excess amount of PSS was used as stabilizers during the synthesis. Indeed, upon increasing the number of post-synthesis NPSM purification which involves particle precipitation and their re-dissolution in DI-water to eliminate excess organic stabilizers, we observed a significant decrease of sheet resistance in the hybrid films for a fixed concentration of Ag NPSMs to a resistance value comparable to pristine PEDOT:PSS films (Figure 3. 9).

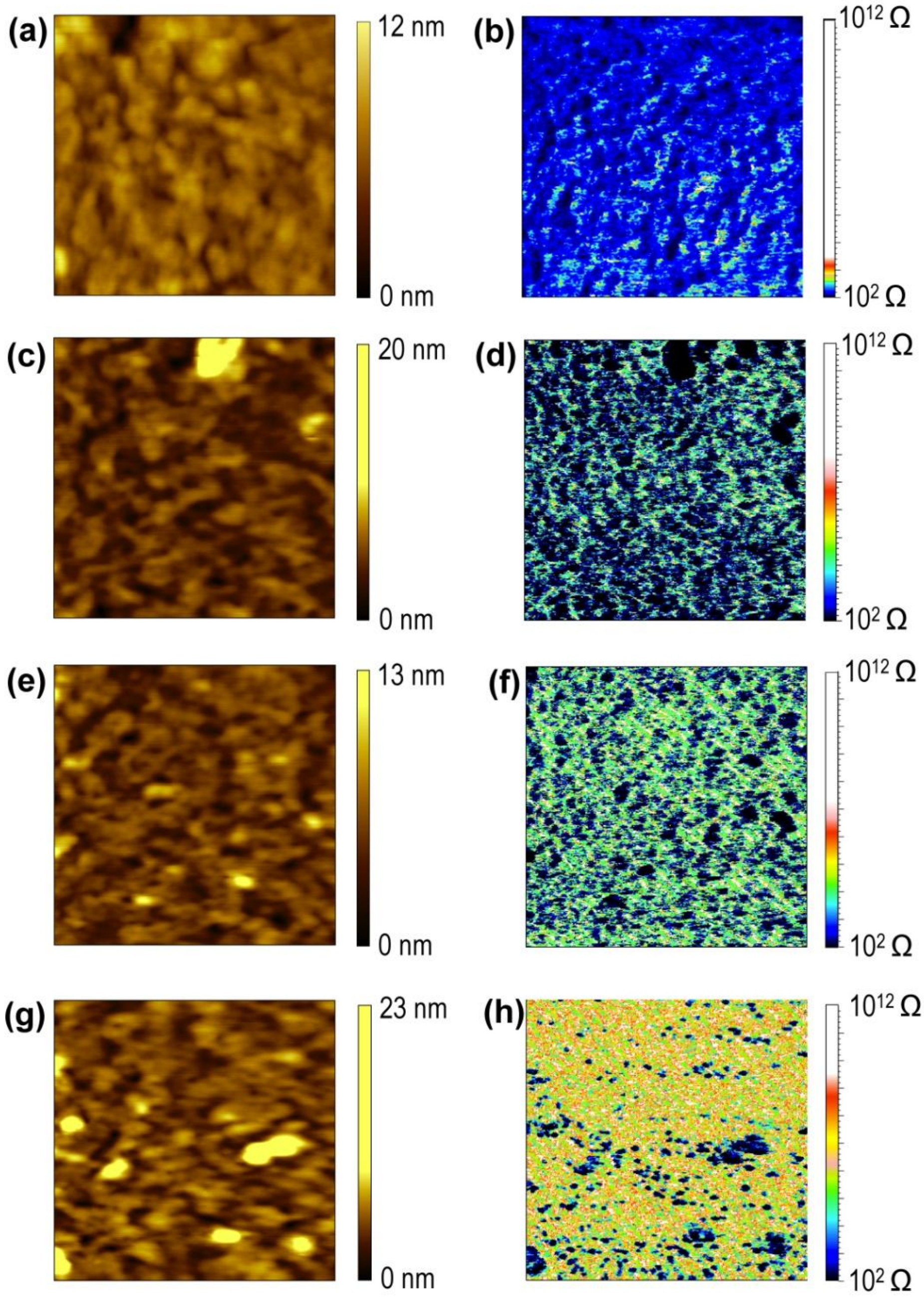

Figure 3. 8 AFM height images (a, c, d, e) and C-AFM resistance signal images (b, d, f, h) for different Ag NPSM concentrations in PEDOT:PSS: (a, b) 0 mg/mL; (c, d) 0.6 mg/mL; (e, f) 1.6 mg/mL; and (g, h) 2.6 mg/mL. All images have a lateral scale of 2 by 2 microns.

The possibility of reducing the global sheet resistance of hybrid Ag NPSM-PEDOT:PSS films through nanoparticle purification is important for their applications in organic solar cells because high sheet resistance of the hybrid layer can lead to high series resistance and poor fill-factor of the solar cell. Besides post-synthesis purification, it is also possible to use organic solvent additives [271,272] to reduce the sheet resistance of the hybrid films. In this second approach the addition of a small volume percentage of organic solvent additives such as dimethyl sulfoxide, ethylene glycol, and glycerol was found highly effective in reducing the resistance of PEDOT:PSS films possibly through inducing a conformational change of the PEDOT chains [86,273]. In this work 5 % (v/v) of glycerol was added into the hybrid Ag NPSM-PEDOT:PSS solution before fabricating hybrid thin films by spin-coating. The use of glycerol additive led to a dramatic reduction of sheet resistance (Figure 3. 9, blue triangle, corresponding to 0.06 MOhm/sq) to a value even smaller than those observed in pristine PEDOT:PSS films. These results show that there are multiple approaches available, such as nanoparticle purification and organic solvent additives, to partially or completely remove the disadvantage of increased sheet resistance observed in hybrid Ag NPSM-PEDOT:PSS films compared to pristine PEDOT:PSS films.

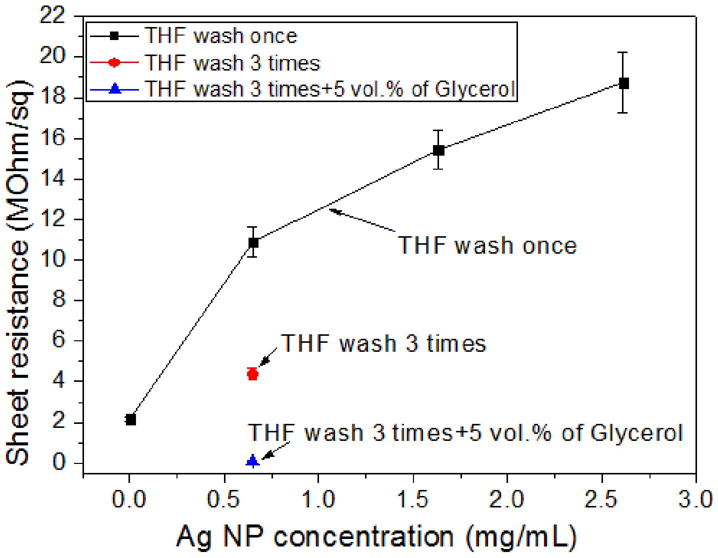

Figure 3. 9 Sheet resistance of hybrid Ag NPSM-PEDOT:PSS films as a function of Ag NPSM concentration.

3.4. Conclusions

The structural, optical and electrical properties of hybrid PEDOT:PSS thin films doped with different amounts of Ag NPSMs are investigated by various characterization techniques including transmission electron microscopy, regular and conductive atomic force microscopy, optical absorption, goniophotometry, and four-point probe resistance measurement.

The addition of Ag NPSMs has a strong effect on the optical properties of the PEDOT:PSS films: (1) Increased optical absorption was found as the amount of Ag NPSM increased; and (2) more light is scattered in high angles associated with the addition of Ag NPSMs. The increased light scattering in hybrid films can possibly lead to more efficient light harvest in organic solar cells.

The addition of Ag NPSMs also modified the structural and electrical properties of the PEDOT:PSS films: (1) Increased surface roughness was observed upon adding of Ag NPSMs which is likely due to the formation of Ag agglomerates; and (2) the global sheet resistance of the hybrid films was found to increase as the concentration of Ag nanoprism increases, despite the formation of local low resistance regions from Ag NPSMs. While the increased surface roughness in hybrid films can be potentially improved by future advances on colloidal surface chemistry, we showed that the sheet resistance in hybrid films can be reduced to a resistance value comparable to or lower than those in pristine films by either increasing the extent of NPSM post-synthesis purification or applying organic solvent additives.

Chapter IV

Plasmonic organic solar cells using silver nanoprisms

This chapter presents the optimization of regular P3HT:PCBM bulk heterojunction solar cells and the studies of organic solar cells with silver nanoprisms incorporated into the PEDOT:PSS layer of regular P3HT:PCBM bulk heterojunction solar cells.

4.1. Optimization of regular P3HT:PCBM solar cells

4.1.1. Introduction

As described in chapter I, there are many factors affecting the final performance of bulk heterojunction (BHJ) organic solar cells (OSCs). However, the device performance of OSCs is predominantly affected by the choice of the photo-absorbing materials, the thickness and morphology of active layer, electrode materials and the quality of their contact with polymer.

In this section, we studied the effects of thermal annealing, solvent addtives on the properties of PEDOT:PSS films and the resulting solar cell characteristics, as well as the effects of the controlling of nanoscale morphology of photoactive layer on the solar cell characteristics.

4.1.2. Optimization of PEDOT:PSS layer

Since the pristine Clevios™ P – Heraeus PEDOT:PSS used in this work has the maximum conductivity of ~ 1 S/cm [72] which is very low, techniques such as post-deposition thermal annealing and adding high boiling solvents (in our case, glycerol) were applied to improve the conductivity of PEDOT:PSS films.

4.1.2.1. Thermal annealing of PEDOT:PSS films

Post-deposition thermal annealing at appropriate temperature can enhance the conductivity of PEDOT:PSS film by modifying its morphology, since the carrier (hole polarons) transport in PEDOT:PSS is determined by its nano-morphology [56,58,274].

1) Sheet resistance of thermal-annealed PEDOT:PSS films

Figure 4. 1 shows the effects of thermal annealing on the sheet resistance of the PEDOT:PSS films which were thermally annealed for 30 minutes at 150 ℃, 200 ℃, 230 ℃, 240 ℃, 250 ℃, respectively. As shown in the figure, the sheet resistance decreases dramatically with increasing annealing temperature from 150 ℃ to 230 ℃. This is probably due to the evaporation of water upon annealing [74]. The decrease of the interparticle water content can reduce the hopping barrier of charge transport. Moreover, upon increasing the annealing temperature, the size of PEDOT-rich grains increase by a coalescence of PEDOT:PSS particles. Such an increase lead to a higher degree of crystallinity and also a reduction of hopping barriers and thus an increase in conductivity [275]. Vitoratos, *et al.* [58] reported that the PSS could be slightly reduced by thermal annealing leading to a lower charge transport barrier. The above-mentioned factors offer possible explanations for the observed sheet resistance reduction of PEDOT:PSS films upon annealing.

When the annealing temperature was increased to 250 ℃, the sheet resistance of PEDOT:PSS films did not show a significant reduction (Figure 4. 1). While increasing the annealing temperature, a lower conductivity may be obtained, since over 250 ℃, the over-oxidation and degradation of PEDOT:PSS by the loss of the sulfuric acid groups from PSS could happen during thermal annealing at 250 ℃ [74,276].

General speaking, the dependence of conductivity of PEDOT:PSS films on thermal annealing temperature could possibly be explained by a competition between the enhanced crystallization and the onset of the material degradation [274]. The thermal annealing could evaporate the residue water, increase the crystallinity of PEDOT, and improve the size and connectivity of PEDOT-rich grains, thus could lower the number and/or height of the hole transport barriers, leading to high conductivity in PEDOT:PSS films [274]. But in other hand, the doped PEDOT could continuously degrade when the annealing temperature is over 150 ℃ [277]. So increasing the annealing temperature, this degradation could become severe. If the annealing temperature is over 250 ℃, the degradation of PEDOT:PSS will become apparent (maybe due to degradation of PSS [74,276]) and leading to an decrease in conductivity [74,274,276,278]. In addition, thermal degradation of PEDOT:PSS can also reduce the size of PEDOT grains and consequently enhance their distance leading to an equivalently increasing potential barrier for carrier transport [58].

In this thesis, we found that an annealing temperature in the range of 230 ℃ and 250 ℃ led to PEDOT:PSS films of relatively low sheet resistance.

The optical transmittance of annealed PEDOT:PSS films at different temperatures was also investigated in this thesis (Figure 4. 2). With increasing annealing temperature from 150 ℃ to 230 ℃, the optical transmittance was found to increase, suggesting a probable reduction of the surface roughness of PEDOT:PSS films or a reduction of material mass. This is likely due to the thermal degradation of PEDOT:PSS [274,278] and the resultant reduction of PEDOT grain size [58]. Our result is coherent with the results previously observed by AFM measurement [278]. Despite some variations exist on the optical transmittance of PEDOT:PSS by different annealing temperatures, the transmittance can be typically maintained between 80% and 85% allowing a high transparency for their application in OSCs.

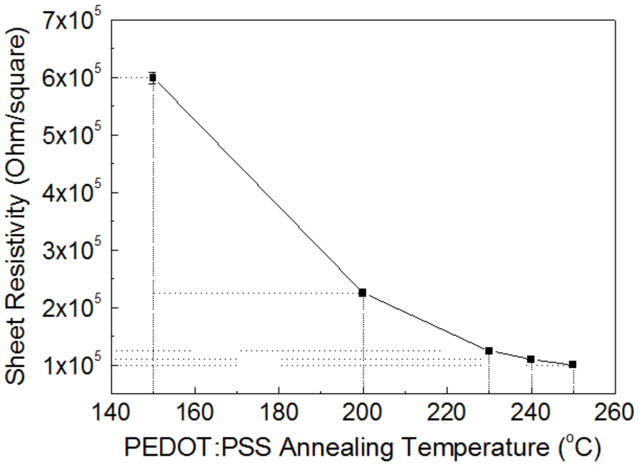

Figure 4. 1 Sheet resistance of PEDOT:PSS films as a function of annealing temperature

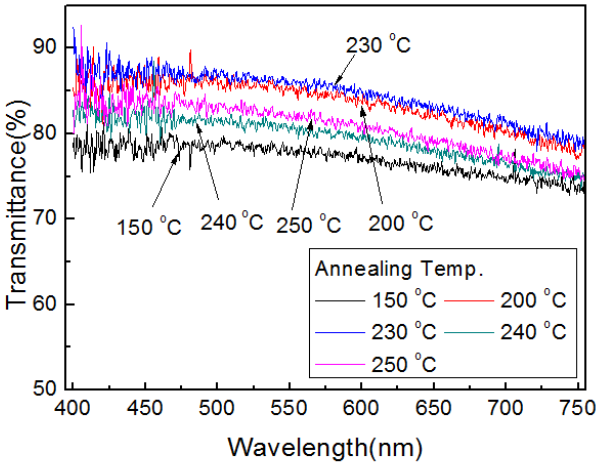

Figure 4. 2 Transmittance as s function of PEDOT:PSS Annealing Temperature

2) Photovoltaic characteristics of OSCs using thermal-annealed PEDOT:PSS films

Figure 4. 3 shows the current density-voltage (*J*-*V*) characteristics and Figure 4. 4 displays the effects of various thermal annealing temperatures of PEDOT:PSS films on the different

photovoltaic parameters including power conversion efficiency (*PCE*), J_{SC}, V_{OC}, and *FF* in P3HT:PCBM OSCs. Note that the R_s and R_{sh} were derived by taking the inverse slopes of the *J*-*V* curve obtained under AM 1.5 simulated illumination.

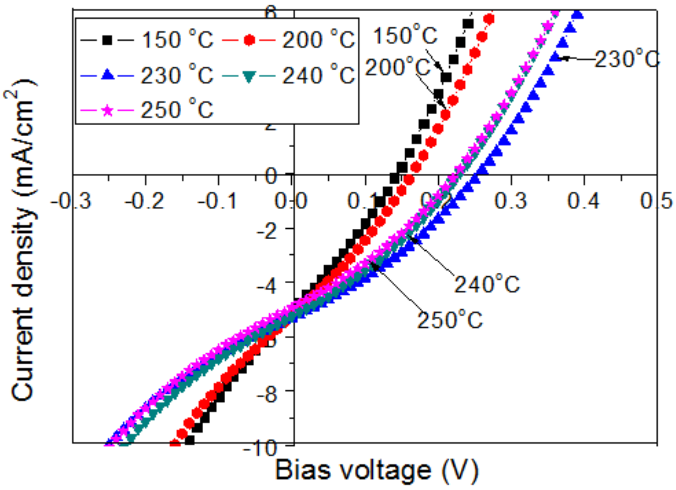

Figure 4. 3 Photovoltaic *J*-*V* curves measured from OSCs using PEDOT:PSS films annealed at different temperatures under illumination

As shown in the Figure 4. 3, these *J*-*V* curves exhibit a characteristic “S-shape”. Such an “S-shape” indicates that the devices are limited by space-charge effects, high series resistance [46] or a contact-driven process [15]. Typically, R_s is in the scale of $10^0 \sim 10^1$ ohms in polymer-fullerene solar cell. As shown in Figure 4. 4 (e), R_s is in the scale of a few hundreds of ohms ($R_s/R_{sh} > 0.38$) which leads to a low *FF* (maximum at around 30 %, Figure 4. 4). Such high R_s value possibly originated from the non-optimal active layer morphology or the surface defects (e.g., contaminants) induced by the non-optimized fabrication conditions. Note that in this thesis, the top contacts (Al electrodes) were thermally deposited by a thermal evaporator outside the glovebox. Before this evaporation the devices need to be transferred outside the glovebox in order to be loaded in this evaporator. As the devices under study were fabricated under identical conditions, despite the non-optimized fabrication process, we can still study the thermal annealing effects of PEDOT:PSS films on these devices.

As seen from Figure 4. 4 (e), R_{sh} showed a peak value at 230 ℃. This suggests minimum recombination in the active layer and near the electrodes, possibly owning to the smooth PEDOT:PSS surface formed by at this annealing temperature.

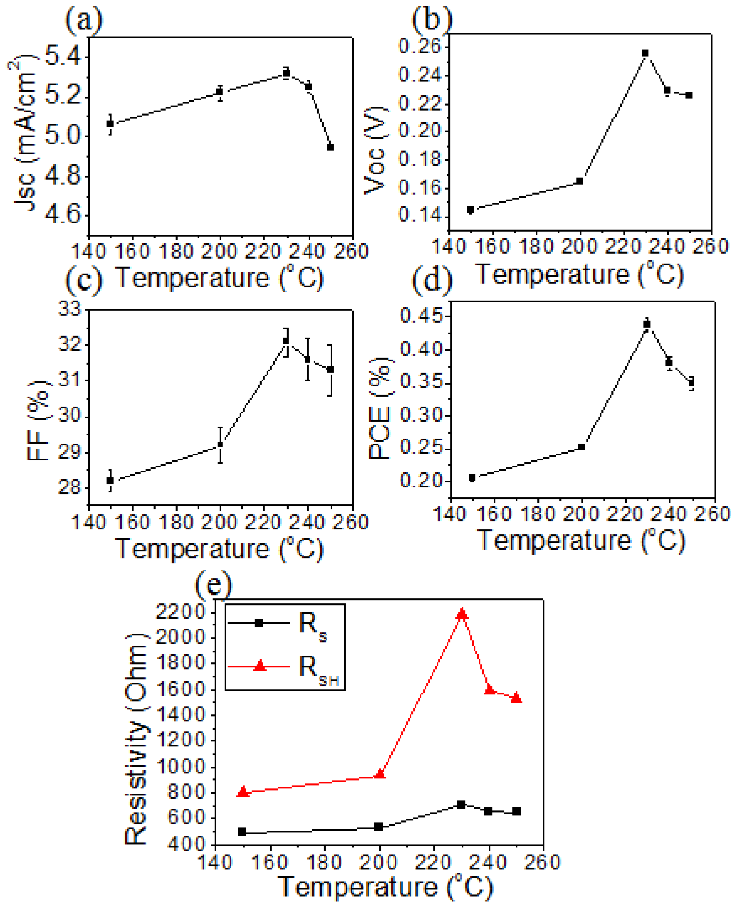

Figure 4. 4 Power conversion efficiency (*PCE*), J_{SC}, V_{OC}, *FF* and sheet resistances as a function of different PEDOT:PSS annealing temperatures in P3HT:PCBM BHJ solar cells.

With regards to J_{sc}: J_{sc} exhibits a peak value when the annealing temperature reaches 230 ℃. This peak value can possibly be attributed to the slightly higher optical transmission. When the annealing temperature further increased over 230 ℃, the PEDOT:PSS degradation appears which results in a reduction of its conductivity [279] and a decreased J_{sc}. With regards to V_{oc}, in principle, the V_{oc} is determined by energy level mismatch of the donor and acceptor materials. Practically, this can be affected by the experimental conditions of the active layer such as the D/A ratio, thickness and morphology (see Section 1.4.3.2.2 for more details). Other factors including the interfaces between the active layer and the electrodes, the blend morpholgy in the immediate vicinity of the electrodes [280], the chemical structure, surface energy, and the roughness of the PEDOT:PSS surface [74], can also play an important role in modifiying the V_{oc} in devices. In our experiments, the V_{oc} is rather small compared to the maximum value (> 0.5 V) achieved in the literature with similar active layer [281,282]. The small V_{oc} achieved in this study may come from the non-optimal active layer conditions and the poor contact between the active layer and the electrodes [126]. Nevertheless, as samples were fabricated under identical condition, these devices can enable us to study the thermal annealing effect of PEDOT:PSS in OSCs. Probably due to the increased shunt resistance, highest V_{oc} was obtained at 230 ℃. When the annealing temperature was increased further, V_{oc} in these devices start to drop possibly due to PEDOT:PSS degradations [74].

We have characterized the external quantum efficiency (*EQE*) of these devices (Figure 4. 5). Overall it shows a similar trend as J_{sc}, a peak *EQE* was found when the annealing temperature was set at 230 ℃.

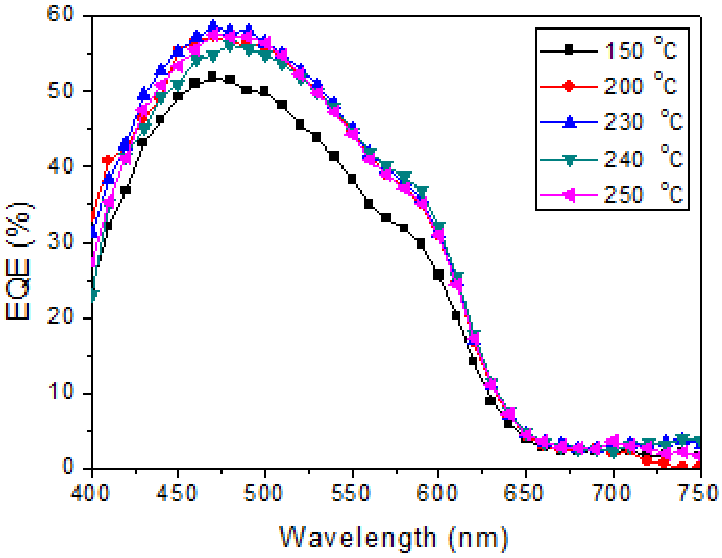

Figure 4. 5 EQE versus the PEDOT:PSS annealing temperature

In summary, we found that the optimal annealing temperature of PEDOT:PSS film to be 230 ℃. This temperature was used in all subsequent studies unless stated otherwise.

4.1.2.2. Glycerol modified PEDOT:PSS

As mentioned above, the devices fabricated using the optimal annealing temperature of PEDOT:PSS still showed an overall high series resistance. To improve the device performance we sought methods to lower the sheet resistance of PEDOT:PSS films. From the literature the addition of high boiling solvents (e.g., glycerol, sorbitol) [75–77] with multiple polar groups into PEDOT:PSS has been reported to be an effective way. Inspired from the literature we experimented the addition of glycerol to enhance the conductivity of PEDOT:PSS films.

Different volume percentages including 2.5%, 5.0%, 7.5% and 10.0% of glycerol were added into the PEDOT:PSS solution, respectively. The resulting conductivities of PEDOT:PSS films are shown in Figure 4. 6. Our pristine PEDOT:PSS sample exhibited only a very small condutivity, in the order of 10^{-3} S/cm. Upon adding 7.5 vol% glycerol, the conducctivity is dramtically enhanced to around 108 S/cm.While we do not expect the transparency of PEDOT:PSS films doped with glycerol to change significantly [283], the surface morphology of the doped PEDOT:PSS films appears to become “swollen” with aggregated features [284].

The effective reduction of resistance in doped PEDOT:PSS films has been attributed to either the plasticizer effect, PSS reduction in the surface content, or a conformational change of the PEDOT chains [86,273,285].

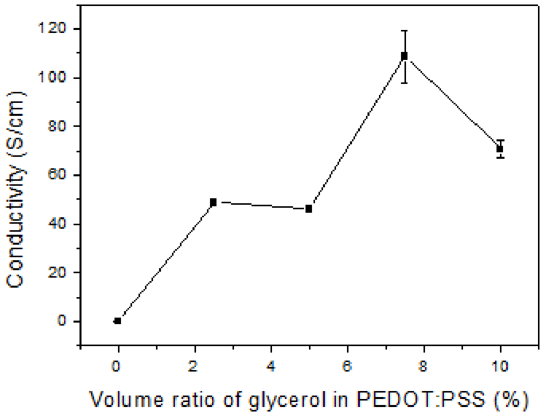

Figure 4. 6 Conductivity of glycerol modified PEDOT:PSS as a function of glycrol volume ratio

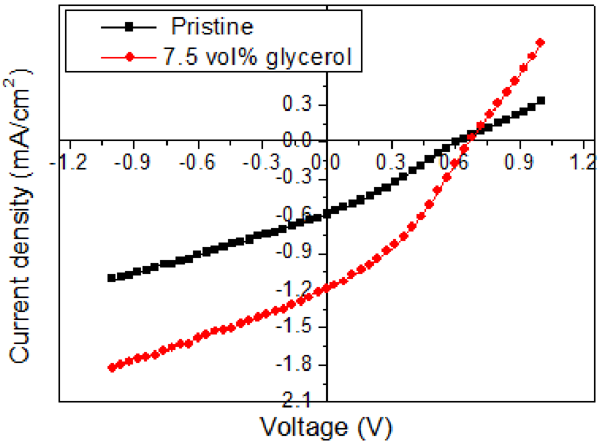

Figure 4. 7 Current density (J)-voltage (V) curves of organic solar cells using glycerol doped and non-doped PEDOT:PSS films

The combination of the significantly enhanced conductivity and the maintained transparency in glycerol modified PEDOT:PSS allows it to be a good choice for OSCs. In this thesis, a batch of OSCs using glycerol doped PEDOT:PSS films (denoted as G-OSCs) was fabricated to study the effect of doping. Figure 4. 7 shows the *J-V* characteristics of two OSCs using glycerol doped and non-doped PEDOT:PSS films. As shown in this figure, upon adding 7.5 vol% of glycerol into the PEDOT:PSS, the J_{sc} was significantly enhanced. We attribute this J_{sc} increase to the reduction of the series resistance by doping glycerol in PEDOT:PSS films.

4.1.3. Optimization of photoactive layer

In bulk heterojunction (BHJ) polymer-fullerene solar cells, the device performance is significantly related to the nanoscale morphology of the active layer. Among different parameters that could affect the nanoscale morphology (see details in Section 1.3.2.3), the starting chemicals, the D/A ratio and their solution concentration, the type of solvent, and the film deposition method were kept as fixed parameters. The parameters that we optimized include the thermal annealing temperature, the film growth rate (effect of solvent annealing) and crystallinity of P3HT in photoactive blend solution (effect of hexane).

Post-deposition thermal annealing is believed to be a simple but effective technique to control the nanoscale morphology of active layer in BHJ polymer-fullerene solar cells [99,104,286]. Heat treatment at an appropriate temperature with a proper duration can activate the polymer/fullerene materials and help moderate phase separation. It has been reported that the increase of P3HT crystallinity and the PCBM domain size in the active layer can enhance the charge mobility [104,286–289] and light absorption [286]. In fact, upon thermal annealing, the side chains of P3HT become mobile and the self-organization of P3HT can occur leading to a higher degree of crystallinity with a closer intermolecular π-stacking in a lamella fashion (Figure 1. 20) [93]. The improved close intermolecular π-stacking (crystallinity) increases the hole mobility and reduces the charge recombination [99] leading to the overall better device performance. In addition, post-deposition thermal annealing can enhance the device performance also due to the removal of residue solvent [289]. However, an annealing temperature too high (> 150 ℃) [290] or prolonged thermal annealing [291] could lead to a macro-phase segregation of P3HT and PCBM crystallized domains. The size of these crystals can reach the range of microns [109,290]. This is not favorable for charge generation, separation, and transport [291] and thus deteriorates the device performance. Consequently, there should be an optimum annealing temperature and duration for polymer-fullerene solar cells [111].

The nanoscale morphology of photoactive layer can be also controlled by solvent annealing through varying the solvent-removal speed (*i.e.*, film growth rate) [99]. In principle, the packing of polymer chains is strongly influenced by the processing solvent evaporation rate. Indeed, a less volatile processing solvent has a longer drying time and thus a longer deposition time. This means that the thin film takes more time to self-organize leading to larger crystalline PCBM and P3HT domains [292,293]. As a result, the use of high-boiling-point solvent and annealing improves the molecular ordering. On the contrary, the use of low-boiling-point solvents will not only lead to a reduction of P3HT crystallinity [293,294] but also an increase in the interlayer distance (b-axis orientation, see Figure 1. 20 in Section 1.3.1.1.1) [294] resulting in a higher hopping barrier and thus a lower charge mobility. Following similar principles the use of solvent additives can improve the morphology of the photoactive layer. It has been demonstrated that, adding a certain amount of “unfriendly” or poor solvent (e.g., n-hexane) in the solution of the organic blend could lead to the formation of strong aggregation of the polymer and hence obtain higher polymer crystallinity [295–300].

4.1.3.1. Thermal annealing

We tested different post-deposition annealing temperatures (devices annealed after electrode deposition): 130 ℃, 140 ℃, 150 ℃, 160 ℃ and 170 ℃, all for 10 minutes. Figure 4. 8 shows the resulting *J-V* curves of the devices obtained under illumination and Figure 4. 9 displays the *PCE*, J_{sc}, V_{oc}, *FF*, R_s and R_{sh} as a function of different annealing temperature for the active layers. The R_s and R_{sh} were also derived by taking the inverse slopes of the *J-V* curve obtained under AM 1.5 simulated illumination.

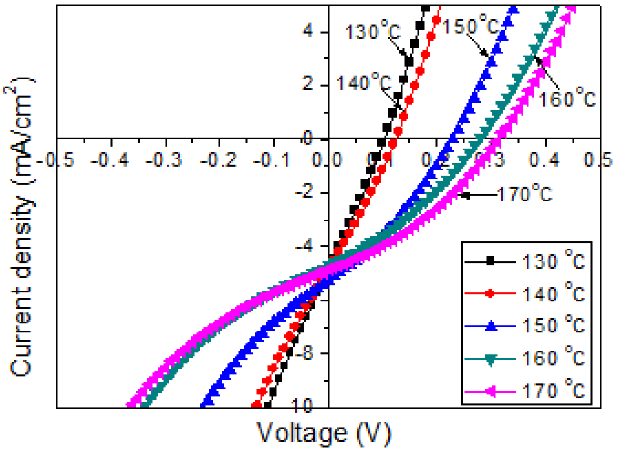

Figure 4. 8 Photovoltaic J-V curves of OSCs with active layer annealed at different temperatures, the curves were obtained under illumination

It has been reported that, upon thermal annealing of photoactive layer, the J_{sc} will increase significantly because of the enhancement of hole mobility [287,288]. But as shown in Figure 4. 8 and Figure 4. 9 (a), the J_{sc} in this study was not improved dramatically. Note that the *J-V* curves exhibit “S-shapes” resulting from high series resistance [301] or contact-driven process [129]. The extracted R_s values are quite large (over 400 Ohms, $R_s/R_{sh} > 0.27$, Figure 4. 9 (e)), thus leading to a low *FF* (Figure 4. 9 (c)) in these devices. Among these devices we found a maximum J_{sc} corresponding to an annealing temperature of 150 ℃. Annealing at higher temperatures causes a deterioration of J_{sc} but an increase in V_{oc}. The reduced J_{sc} can be attributed to the increased phase separation of the components [109,290]. The phase separation starts when the annealing temperature reaches the glass transition temperature (~ 110 ℃ [302]) of the blend and PCBM domains are over-grown when the temperature is higher than

150 ℃ [290]. Larger phase separation results in a reduction of charge mobility [291] or a deterioration between the active layer and the contact electrodes [110,302].

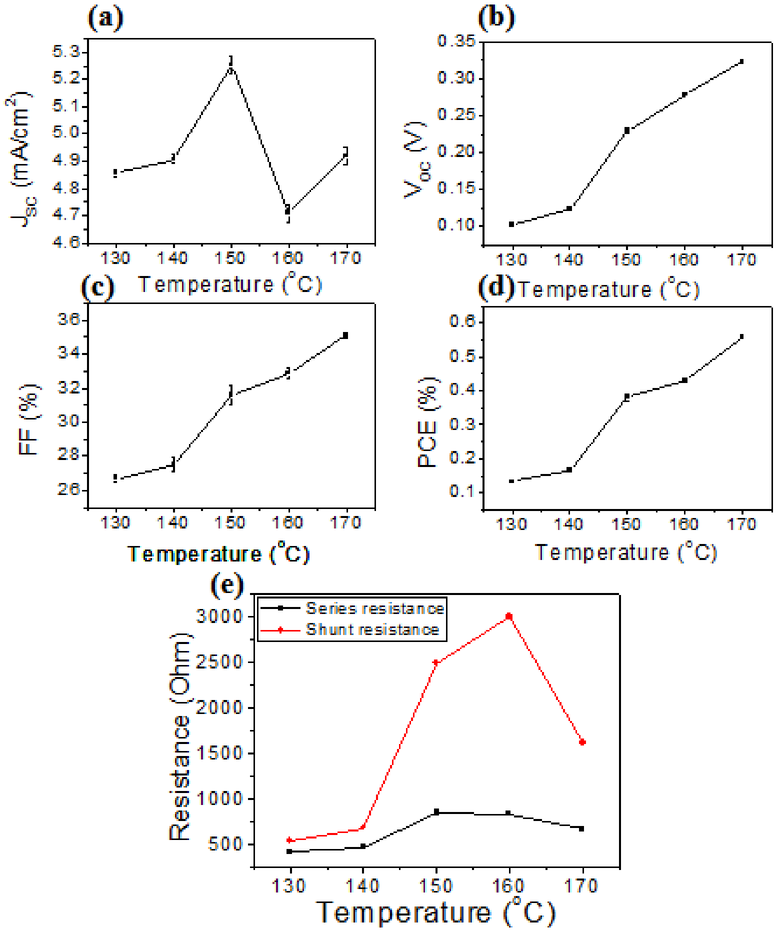

Figure 4. 9 PCE, J_{SC}, V_{OC}, FF and R_s, R_{sh} as a function of active layer annealing temperature

So in general, concerning the results in literature (best annealing temperature 140 ℃ ~150 ℃ [302,303]), 150 ℃ was the chosen to be the annealing temperature for P3HT:PCBM layer in the following studies in this thesis.

4.1.3.2. Solvent annealing and additive for photoactive layer

We also studied the effects of solvent annealing and additive (hexane) on the device performance of OSCs. The experimental conditions for this section are listed in 2.2.2.4.2.

Figure 4. 10 shows the photovoltaic *J-V* curves of the resulting devices. For the "control sample" (sample no. 1), there is an “S-shape” in the *J-V* curve indicating high series resistance (R_s/R_{sh} = 0.4, Table 4. 1) and resulting a low *FF* (32%). By comparison, for devices fabricated using solvent annealing or both solvent annealing and additive, the J_{sc} is dramatically increased reaching 9.87 mA/cm^2 and 8.58 mA/cm^2, respectively. This can be explained by the reduction of series resistance (Table 4. 1 and Figure 4. 11) resulted from the higher crystallinity and

optimized nano-morphology in photoactive layer. We achieved a slightly lower J_{sc} in devices fabricated by adding a small amount of hexane into the photoactive blend solution than devices using solvent annealing only. This is probably due to the addition of hexane together with solvent annealing lead to overgrown P3HT crystallites.

With regards to R_{sh}, compared to the control device it significantly increases in devices using solvent annealing or adding hexane reaching from 1614 ohms to 7981 ohms (R_s/R_{sh} = 0.04) and 7903 ohms (R_s/R_{sh} = 0.03), respectively (Table 4. 1). This can be also attributed to the higher crystallinity and optimized nano-morphology. The increase in R_{sh} may be one of the causes leading to the enhanced V_{oc}.

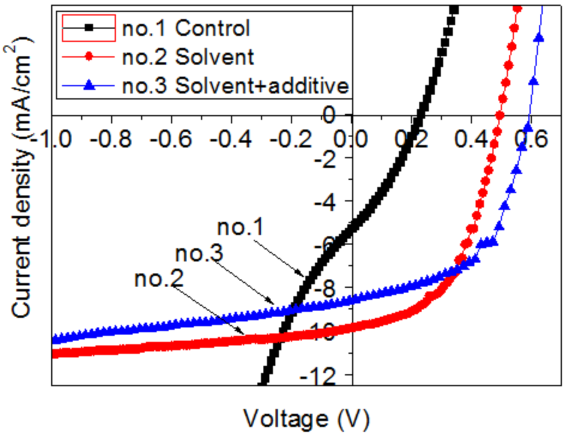

Figure 4. 10 Current density – voltage curves versus solvent annealing and additive. Sample no.1 is the control OSC that was applied only thermal annealing, no.2-slovetn annealing and subsequently thermal annealing, no.3-addtition of hexane, then solvent annealing subsequently thermal annealing

Sample no.	J_{SC} (mA/cm^2)	V_{OC} (V)	*FF* (%)	*PCE* (%)	R_s (Ohm)	R_{sh} (Ohm)
1	5.25	0.23	32	0.38	669	1614
2	9.87	0.50	51	2.50	309	7981
3	8.58	0.59	55	2.77	232	7903

Table 4. 1 Device Parameters of the resulting solar cells present in Figure 4. 10

The *EQE* of these OSCs were shown in Figure 4. 12. The EQE curve of the control sample has a broad peak at ~ 465 nm and a small shoulder at ~ 600 nm. The broad peak at 465 nm is induced by the isolated P3HT chains [304]. Such P3HT chains adopt a flexible coil configuration and are in solution-like state, indicating a very low P3HT crystallinity. The shoulder at ~ 600 nm with a very low intensity shows that there is a small amount of P3HT crystallites formed in the photoactive film. Upon solvent annealing or adding hexane followed by solvent annealing, the shoulders at ~ 600 nm are much more pronounced, indicating a higher degree of ordering of P3HT [305]. These EQE results further demonstrate that the solvent annealing or the addition of hexane together with solvent annealing can improve the P3HT crystallinity.

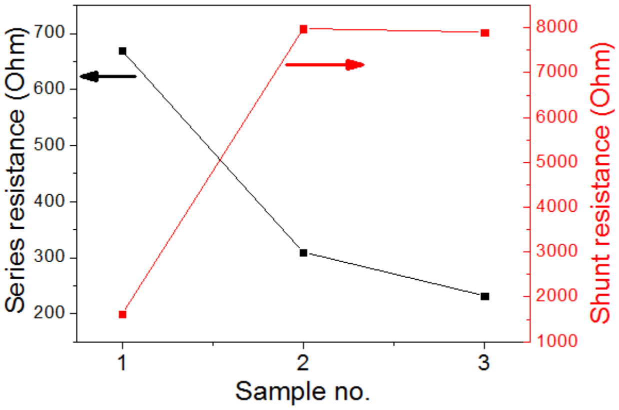

Figure 4. 11 Resistances as a function of fabrication process of active layer. Sample no.1 is the control OSC that was applied only thermal annealing, no.2-slovetn annealing and subsequently thermal annealing, no.3-addtition of hexane, then solvent annealing subsequently thermal annealing

Compared to the control device, devices with solvent annealing or the addition of hexane show an improved *EQE* at the short wavelength range approaching 400 nm, which corresponds to the wavelength range of PCBM absorption. This is possibly due to the fact that the solvent annealing or additive can form more continuous and favorable vertical pathways for electrons to cathode and thus making PCBM a larger contribution in light absorption and *EQE* than that in the control sample.

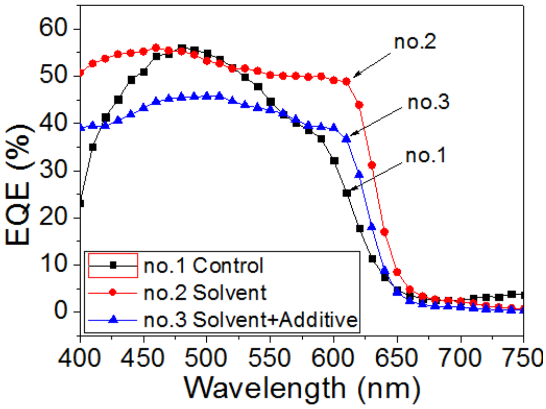

Figure 4. 12 *EQE* as a function of fabrication process of active layer

In summary, the photovoltaic performance was improved by solvent annealing or an addition of hexane accompanied with thermal annealing, leading to a *PCE* enhancement from 0.38% to 2.77%.

Practically, it is complicated to control the addition speed of hexane. When the addition is too fast, P3HT maybe precipitated from the solution [296], leading to deterioration of *PCE* in OSCs. Therefore, in the following part of this thesis we only apply solvent annealing together thermal annealing to fabricate plasmonic solar cells with silver nanoprisms.

4.2. Studies of plasmonic solar cells composing silver nanoprisms in PEDOT:PSS

4.2.1. Introduction

The incorporation of metallic nanoparticles (MNPs) in organic solar cells can enhance the light absorption in active layer by increasing the effective optical path length [109,110,120], by the coupling with the strong near field of MNPs induced by localized surface plasmon resonance [110,120,121], or even by enhancing the exciton dissociation [121].

In order to explore the potential benefits from light scattering and the localized surface plasmon resonance effects in organic solar cells, we experimented the incorporation of Ag nanoprisms (NPSMs) in the PEDOT:PSS layer of P3HT/PCBM bulk heterojunction solar cells. This section presents the results obtained from these solar cells.

4.2.2. plasmonic solar cells composing silver nanoprisms in PEDOT:PSS

4.2.2.1. Introduction

To study the effects of Ag NPSMs on the device performance of OSCs, a control OSC without Ag NPSMs and 3 plasmonic OSCs with different amount of Ag NPSMs in PEDOT:PSS layer were fabricated (see more details in Section 2.2.2.5).

4.2.2.2. Characterization and discussion

Figure 4. 13 displays the photovoltaic *J-V* characteristics under simulated AM 1.5 illumination of the OSCs using pristine PEDOT:PSS and PEDOT:PSS with different amounts of Ag NPSMs incorporated. The control sample exhibits a V_{oc} of 0.50 V, a J_{sc} of 9.87 mA/cm^2, and a *FF* of 50.6%, leading to a *PCE* of 2.50% (Table 4. 2), as presented in Section 4.1.3.2. Upon adding Ag NPSMs, the V_{oc} decreases, from 0.50 to 0.46 V (Table 4. 2 and Figure 4. 14 (b)), probably due to the modified PEDOT:PSS/photoactive layer interface by Ag NPSMs. Similarly, the J_{sc} monotonically declines, from 9.87 mA/cm^2 to 8.58 mA/cm^2 as the concentration of Ag NPSMs increases from zero to 2.6 mg/mL in PEDOT:PSS solution (Figure 4. 14 (a) and Table 4. 2). This indicates that reduced amount of charge carriers were able to be collected into the external circuit, possibly due to the increased series resistance

and/or more recombination losses within the plasmonic OSCs. The *FF*s also decreases upon adding Ag NPSMs comparing to that of control OSC (Figure 4. 14 (c) and Table 4. 2). As a result, there is a slight decline in *PCE* from 2.50 % to 1.93 % as the concentration of Ag NPSMs increases from zero to 2.6 mg/mL in PEDOT:PSS solution (Figure 4. 14 (d) and Table 4. 2).

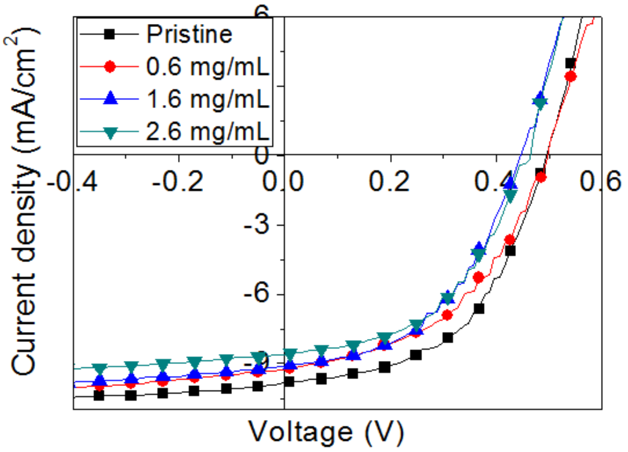

Figure 4. 13 J-V curves of the OSCs using pristine PEDOT:PSS and using different amount of Ag NPSMs in PEDOT:PSS

Figure 4. 15 shows the *J-V* characteristic curves of the control OSC and the different plasmonic OSCs under dark condition. Among all these devices, the shunt resistance of the plasmonic OSC using 2.6 mg/mL in PEDOT:PSS is much lower than those from other OSCs. The lower shunt resistance indicates more shunt pathways for charge carriers. It is possible that, with a high concentration of Ag NPSMs in the PEDOT:PSS layer, the PEDOT:PSS/photoactive layer interface may have more defects leading to increased recombination at this interface. Besides the shunt resistance, as seen in Figure 4. 15, the series resistance of the control OSC is smaller than that of OSCs but close to them. This is consistent with the series resistance results obtained from *J-V* curves under illumination at V_{oc}, as seen in Table 4. 2, although the series resistances of all the plasmonic OSCs are slightly higher than that of the control OSC.

To study how the addition of Ag NPSMs influences the structural and optical properties of the PEDOT:PSS films, we performed characterizations including optical absorption, goniophotometry, AFM, C-AFM and 4-point probe measurements. These results have been presented in Section 3.3.2.

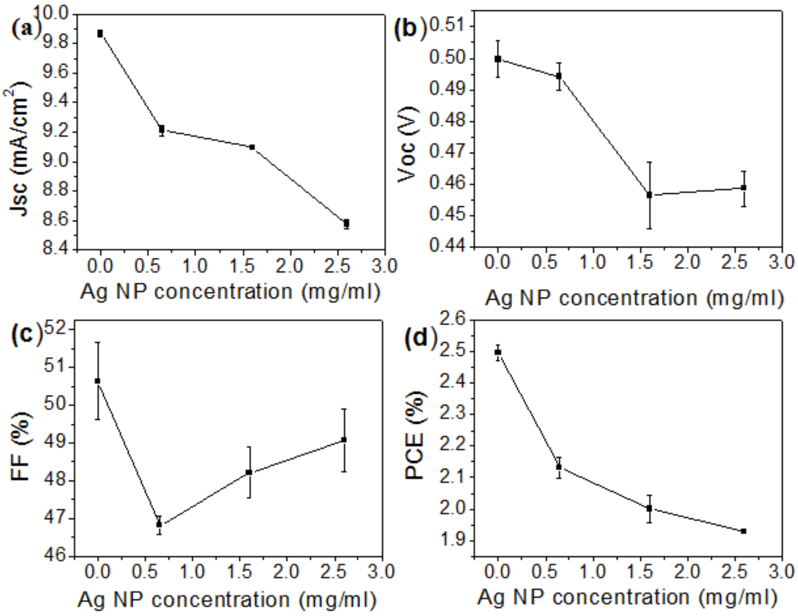

Figure 4. 14 Plots of *Jsc*, *Voc*, *FF* and *PCE* as a function of Ag NPSMs concentration in PEDOT:PSS films of OSCs

Ag NP concentration (mg/ml)	*Voc* (V)	*Jsc* (mA/cm^2)	*FF* (%)	*PCE* (%)	*Rs* (Ohm)
0	0.500	9.87	50.6	2.50	307
0.6	0.494	9.21	46.8	2.13	346
1.6	0.456	9.10	48.2	2.00	374
2.6	0.459	8.58	49.1	1.93	337

Table 4. 2 Photovoltaic parameters of control OSC and OSCs using Ag NPSMs. Note that the series resistances were derived from reverse slope of *J-V* curves under illumination at V_{oc}.

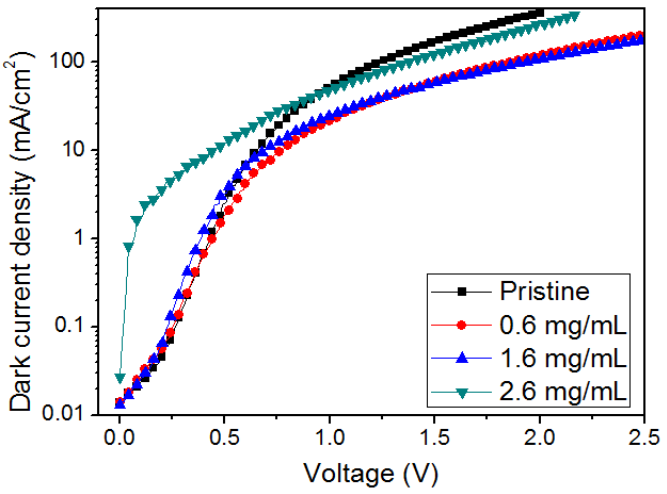

Figure 4. 15 Dark J-V characteristic curves of the OSCs using pristine PEDOT:PSS and using different amount of Ag NPSMs in PEDOT:PSS. *J* is in log10 scale.

These results partly explain the decrease of J_{sc} and V_{oc} in these plasmonic OSCs: first, the addition of Ag NPSMs leads to an increased optical absorption and more scattered light in high angles in the PEDOT:PSS films (Figure 3. 6 and Figure 3. 7).

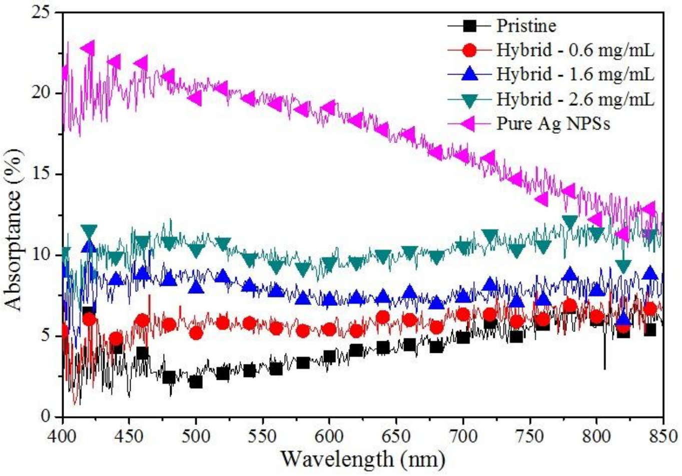

Figure 3.6 Absorption spectra of pure Ag NPSM film, pristine and hybrid PEDOT:PSS films fabricated using different Ag NPSM concentrations. The pure Ag NPSM film was prepared using the method reported in the reference [270].

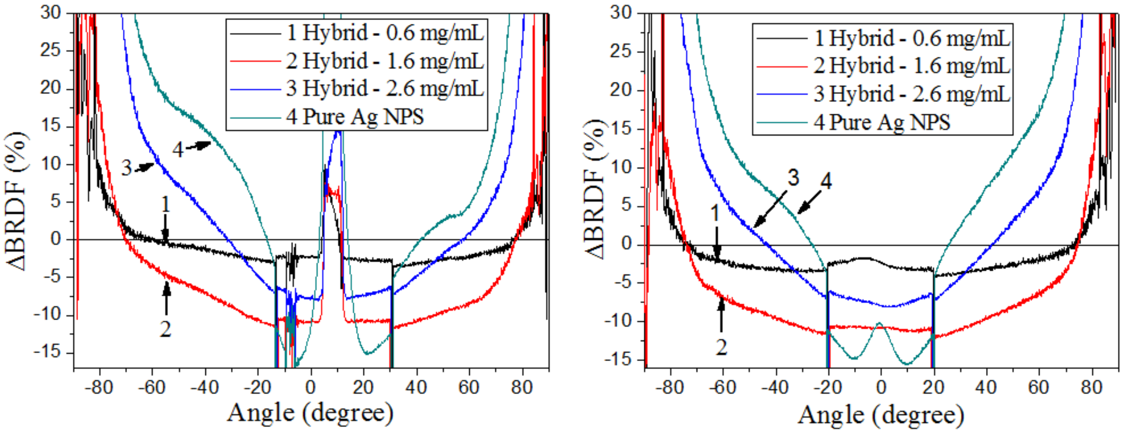

Figure 3.7 In-plane (in the incident light plane, named as in-plane) ΔBRDF (left) and out-of-plane (in the plane perpendicular to the incident plane) ΔBRDF (right) obtained from hybrid PEDOT:PSS films with various Ag NPSM concentrations.

Second, the addition of Ag NPSMs has negative effects on the structural and electrical properties of the PEDOT:PSS films: Increased surface roughness (Figure 4. 17) was observed upon the addition of Ag NPSMs which is likely due to the formation of Ag agglomerates; The global sheet resistance of the hybrid films was found to increase as the concentration of Ag nanoprism increases (Figure 3. 8), despite the formation of local low resistance regions from Ag NPSMs.

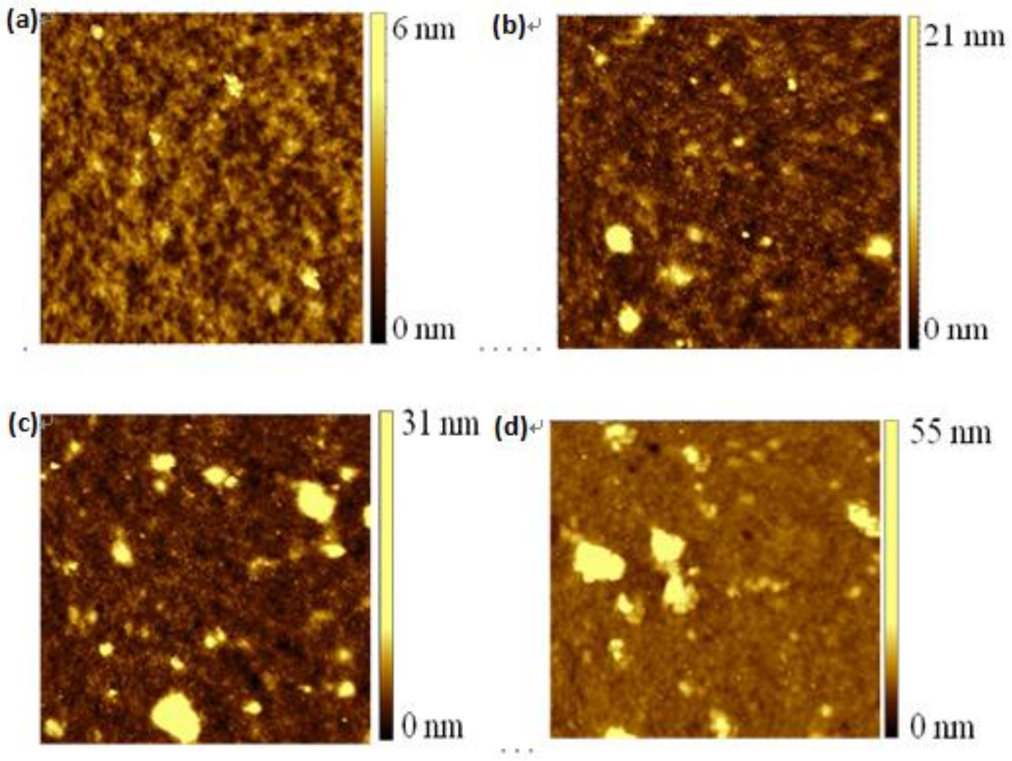

Figure 4. 16 AFM height images for different Ag NPSM concentrations in PEDOT:PSS: (a) 0 mg/mL; (b) 0.6 mg/mL; (c) 1.6 mg/mL; and (d) 2.6 mg/mL. All images have a lateral scale of 2 by 2 microns.

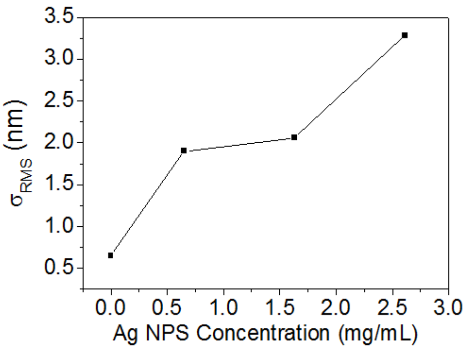

Figure 4. 17 Corresponding root mean square roughness in Figure 4. 16 as a function of Ag NPSM concentration in PEDOT:PSS films: 0.649 nm, 1.9 nm, 2.06 nm and 3.28 nm for Figure 4. 16 (a), (b), (c) and (d), respectively.

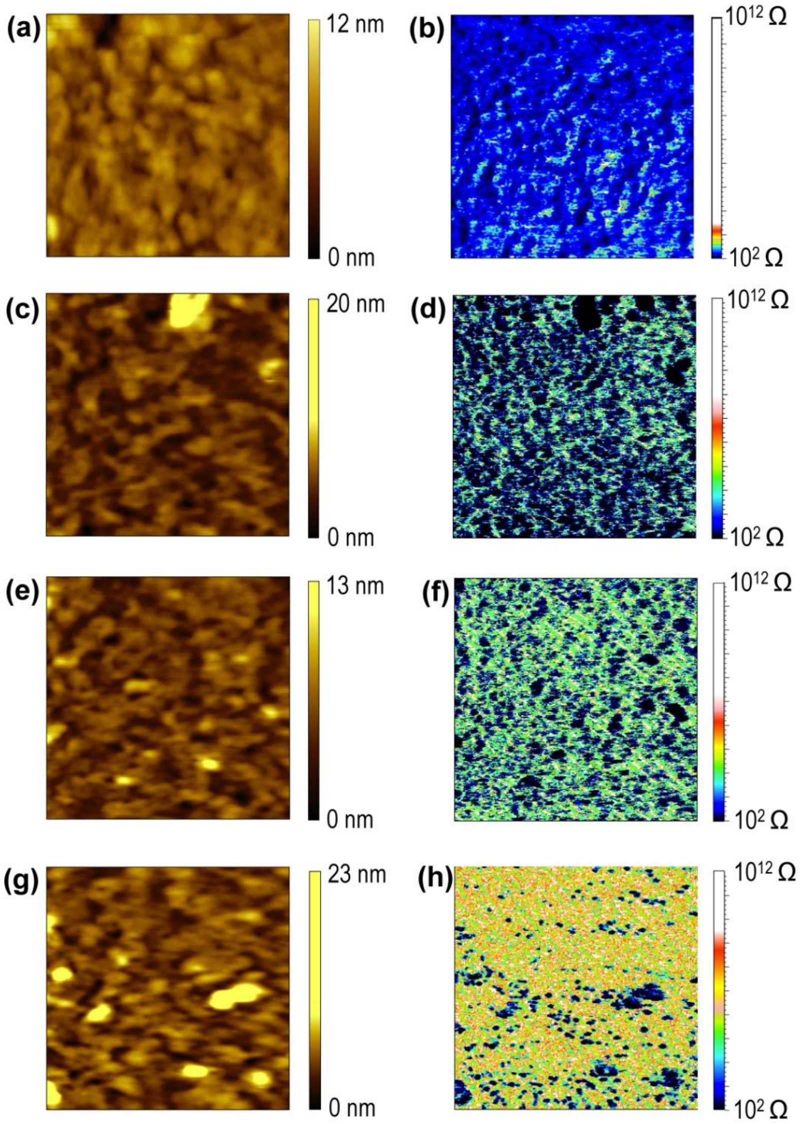

Figure 3.8 AFM height images (a, c, d, e) and C-AFM resistance signal images (b, d, f, h) for different Ag NPSM concentrations in PEDOT:PSS: (a, b) 0 mg/mL; (c, d) 0.6 mg/mL; (e, f) 1.6 mg/mL; and (g, h) 2.6 mg/mL. All images have a lateral scale of 2 by 2 microns.

With regards to J_{sc}: (1) it has been reported that the increased surface roughness (Figure 4. 17) or increased interfacial area of PEDOT:PSS can provide a larger area for more efficient charge collection [306,307] leading to an increase of J_{sc}. (2) The hybrid PEDOT:PSS films have both large Ag agglomerates with a maximum dimension of 300 nm (Figure 4. 16 (c) and (d)) and relatively smaller agglomerates with dimension less than 40 nm (Figure 4. 16 (b)). All agglomerates that are larger than 40 nm (the thickness of the PEDOT:PSS films) may penetrate through the whole film and inserted into the photoactive layer. This may lead to an enhanced recombination at the NPSM surfaces [308,309] and a decrease of shunt resistance and J_{sc}. (3) It has been reported that the metallic nanoparticles (MNPs) in PEDOT:PSS film can slightly reduce the film resistance and thus contribute to the increase of J_{sc} [196,307], since charge carriers can transport through the highly conductive MNP rather than through PEDOT:PSS. This may explain the decreased series resistance of plasmonic OSCs with increasing Ag NPSMs concentration. However, as stated above, the series resistances of all plasmonic OSCs are slightly higher than that of the control OSC. This is contradictory to the previous result incorporating MNPs into PEDOT:PSS [196,307]. We believe that the slightly increased series resistance in our plasmonic OSCs may originate from the insulating PSS polymers contained in the Ag NPSM solutions since PSS was used as stabilizer and agent that plays an importance in the direction-selective growth during the synthesis (see details in Section 3.2.1). Confirming this belief, we observed a significant decrease of sheet resistance in the hybrid films for a fixed concentration of Ag NPSMs to a resistance value comparable to pristine PEDOT:PSS films (Figure 3. 9 in Section 3.3.2.3) after increasing the number of post-synthesis NPSM purification. Such purification involves particle precipitation and their re-dissolution in clean DI-water to eliminate excess organic stabilizers.

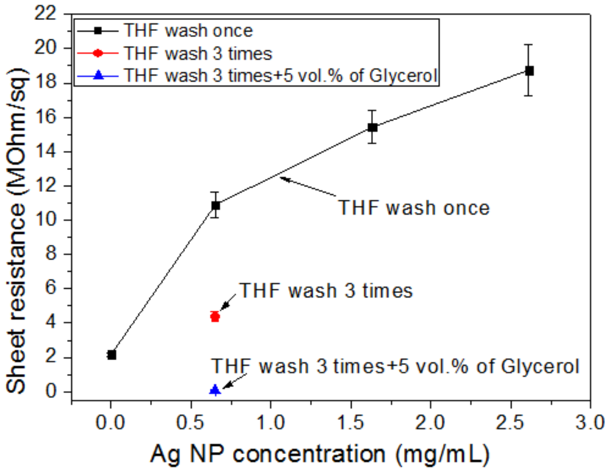

Figure 3.9 Sheet resistance of hybrid Ag NPSM-PEDOT:PSS films as a function of Ag NPSM concentration.

For V_{oc}, the shunt resistance may be reduced through an enhancement of recombination at the Ag agglomerates which leads to a decrease of V_{oc}. The resultant higher leakage current density in the experimental devices leads to a relatively small V_{oc} (< 0.5 V) [310]. Moreover, the addition of Ag NPSMs into PEDOT:PSS has been reported to lead to a formation of bonds between Ag NPSMs and the sulfur atom of PEDOT [311] suppressing the electrostatic interaction between PEDOT and PSS and leading to a significant segregation of PEDOT from the PSS. As a result, this effect leads to a smaller PEDOT:PSS work function [312]. These reported mechanisms explain why the V_{oc} is reduced in our plasmonic solar cells.

EQE of the control and plasmonic OSCs were measured and shown in Figure 4. 18. Consistent with the trend in J_{sc}, the *EQE* declines as the Ag NPSMs concentration in PEDOT:PSS increases.

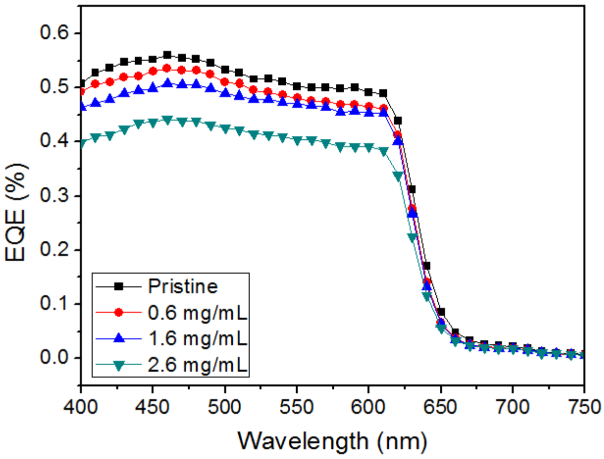

Figure 4. 18 *EQE* as a function of Ag NPSMs in OSCs

In brief summary, the deterioration of device performance of plasmonic OSCs is possibly due to (1) the Ag NPSMs agglomerates at the PEDOT:PSS/photoactive layer interface which act as recombination centers. This leads to a reduction of shunt resistance, J_{sc} and V_{oc}; (2) the excess PSS in Ag NPSMs leads to the observed higher series resistance and also a decrease in J_{sc}. From the results obtained in this section we found that, not only enhanced optical properties due to LSPR, the structural and electrical properties of the hybrid PEDOT:PSS-Ag NPSM films are also important parameters determining the final device performance. In some cases trade-off exists between the enhancement of light absorption due to Ag NPSMs and the negative structural/electrical properties of hybrid films.

4.2.3. Plasmonic OSCs composing Ag NPSMs and glycerol in PEDOT:PSS layer

4.2.3.1. Introduction

In this part, we used the glycerol, an solvent additive, to dramatically reduce the sheet resistance of hybrid Ag-NPSM-PEDOT:PSS films [313–316] and we study the solar cell performance of the resulting plasmonic OSCs. A control OSC using pristine PEDOT:PSS and two plasmonic OSCs using Ag NPSMs and glycerol in PEDOT:PSS layers were fabricated. The Ag NPSM concentrations were fixed to be 0.6 mg/mL and the glycerol concentrations were 1.0 vol% and 2.0 vol%, respectively (see details in Section 2.2.2.6).

4.2.3.2. Characterization and discussion

The resulting sheet resistance of the glycerol-modified hybrid PEDOT:PSS-Ag NPSM films is shown in Figure 4. 19. The addition of a small amount of glycerol remarkably reduces the sheet resistance of the hybrid films.

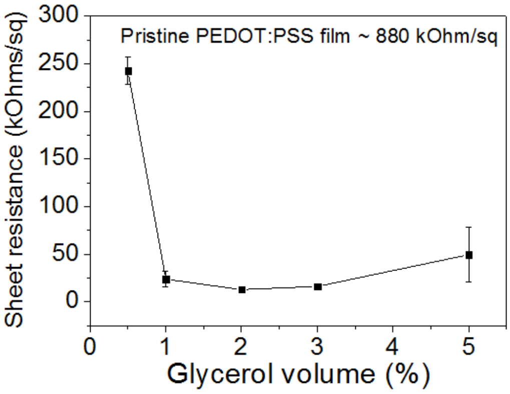

Figure 4. 19 Sheet resistance as a function of glycerol concentration in hybrid PEDOT:PSS-Ag NPSM films

Figure 4. 20 shows the photovoltaic *J-V* curves of the control and the glycerol-modified plasmonic OSCs (denoted as G-plasmonic OSCs) under illumination (AM 1.5). Upon adding glycerol to the hybrid PEDOT:PSS-Ag NPSM films, the J_{sc} increases from 1.65 mA/cm^2 to around 2 mA/cm^2 and the V_{oc} decreases from 0.55 V to 0.45 V (Figure 4. 22 and Table 4. 3). Moreover, the *J-V* curves exhibited “S-shape” which is the indication of high series resistance [301], or contact-driven process [129], or interfacial dipoles or defects [317]. As shown in Table 4. 3, the series resistance of the hybrid OSCs is larger than 4000 Ω. This is much larger than the values found in the previous section (in the range of 200 Ω to 300 Ω). As the series resistance is also high in the control OSC, this indicates that the observed high series resistance does not originate from the addition of glycerol but from the unfavorable contacts in these OSCs. The unfavorable contacts could be possibly attributed to the non-ideal fabrication conditions inducing surface defects (e.g., contaminants) within our limited experimental conditions (e.g., the Al electrodes were thermally deposited outside glovebox).

The decrease in V_{oc} may be due to the decreased shunt resistance in the G-plasmonic OSCs (Figure 4. 21). It may also originate from the lowering of the work function of PEDOT:PSS induced by Ag NPSMs [312] or the addition of glycerol [74].

In terms of J_{sc}, the increase of J_{sc} in plasmonic OSCs can originate from the increased surface roughness due to a larger PEDOT:PSS/photoactive layer interfacial area [306,307], or the enhanced light absorption [233], or the reduction in series resistance [196,307]. In our experiments, as the series resistance increased upon adding Ag NPSMs, the increase of J_{sc} could not be assigned to the reduction of series resistance but rather to the enhanced charge collection and light absorption. While the PEDOT:PSS surface roughness could be increased by both the addition of glycerol [77] and Ag NPSMs (Figure 4. 16 and Figure 4. 17).

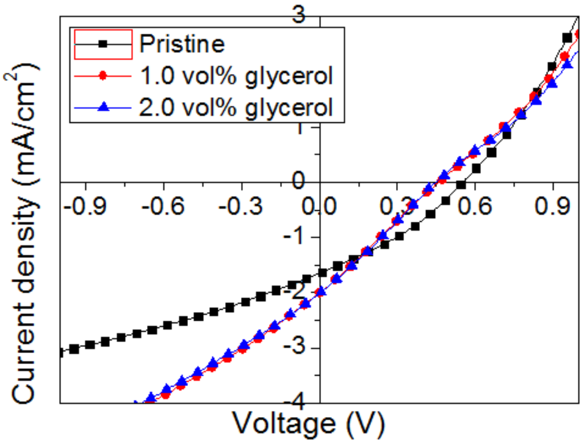

Figure 4. 20 Photovoltaic *J-V* curves of control OSC and G-plasmonic OSCs under illumination

Sample no.	Glycerol (vol%)	*Jsc* (mA/cm^2)	*Voc* (V)	*FF* (%)	*PCE* (%)	*Rs* (Ohm)	*Rsh* (Ohm)
1 (control)	0	1.65	0.552	32.9	0.30	4777	12277
2	1.0	2.00	0.452	25.5	0.23	5786	6278
3	2.0	2.03	0.451	26.56	0.24	5353	6358

Table 4. 3 Photovoltaic parameters of control OSC and G-plasmonic OSCs. Note that the series resistance is extracted from *J-V* curves under illumination.

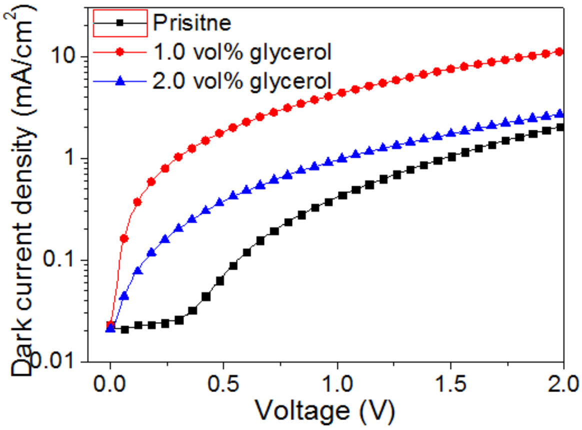

Figure 4. 21 *J-V* curves of control OSC and G-plasmonic OSCs under dark condition. *J* is in log10 scale.

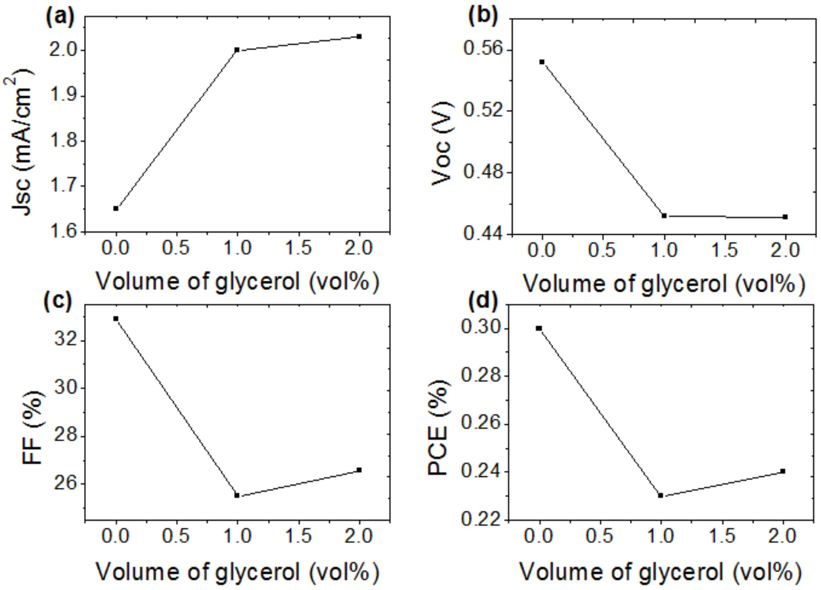

Figure 4. 22 *Jsc*, *Voc*, *FF* and *PCE* as a function glycerol concentration in G-plasmonic OSCs

In conclusion, after incorporating a small amount of glycerol (e.g., 1.0 vol%) into PEDOT:PSS, the plasmonic OSCs exhibited an increase in J_{sc}. Such increased J_{sc} may originate from the increased light absorption due to the LSPR of Ag NPSMs or the enhanced charge collection due to the increase interfacial area between the PEDOT:PSS and the photoactive layer.

4.3. Conclusions

In this chapter, the optimization of fabricating normal organic solar cells using the standard ITO/PEDOT:PSS/P3HT:PCBM/Al structure and the fabrication/characterizations of plasmonic organic solar cells using Ag nanoprisms in PEDOT:PSS layer were investigated.

In the first part of this chapter, in order to obtain functional organic solar cells to study the effects of Ag NPSMs in plasmonic organic solar cells (OSCs) (efficiency > 2 %), we have optimized the thermal annealing temperature, volume percentage of glycerol for PEDOT:PSS. In particular, the nanoscale morphology of photoactive layer was optimized by controlling the thermal annealing temperature and duration, lowering the solvent removal speed through solvent annealing and increasing the crystallinity in photoactive blend solution through adding hexane. At the end of a series of optimization, functional organic bulk heterojunction solar cells based on P3HT/PCBM were obtained. They will be used as test-bed systems for plasmonic OSCs. In fact, in our experiments, after annealing the PEDOT:PSS at 230 ℃ for 30 minutes in a N_2-filled glovebox, a power conversion efficiency (*PCE*) of 2.50 % was obtained by solvent annealing and subsequently thermal annealing at 150 ℃ for 10 minutes; an even higher *PCE* of 2.77% was gained through further adding a small amount of hexane.

In the second part of this chapter, we experimented (1) the incorporation of Ag nanoprisms (NPSMs) into the PEDOT:PSS layer; and (2) the addition of solvent additives (glycerol) into PEDOT:PSS layer to fabricate plasmonic OSCs aiming to improve the device characteristics in (1). Results from (1) showed that, for incorporation of Ag NPSMs into PEDOT:PSS layer of OSCs, the resulting device performance was deteriorated possibly owning to (i) an increased recombination at the Ag NPSMs and aggregations at the PEDOT:PSS/photoactive layer; (ii) an increased series resistance induced by incompletely removed impurities such as PSS in Ag NPSMs. Results from (2) demonstrated that after incorporating a small amount of glycerol (e.g., 1.0 vol%) into PEDOT:PSS, the plasmonic OSCs exhibited an increase in J_{sc} which may originate from increased light absorption due to the LSPR of Ag NPSMs or the enhanced charge collection owning to the increased PEDOT:PSS/photoactive layer surface area.

General conclusions and prospective

General conclusions

Incorporation of metallic plasmonic nanostructures inside organic solar cells is a promising strategy to enhance their power conversion efficiency. In this thesis, we took advantage of the unique optical properties of Ag nanoprisms to enhance the device performance of bulk heterojunction organic solar cells based on a blend of P3HT (donor) and PCBM (acceptor). Practically, the work involved in this thesis includes the following aspects:

First, a series of Ag nanoprisms of similar thickness but of different edge length were successfully synthesized through thermal reduction approach. These Ag nanoprisms with different aspect-ratios exhibit a main in-plane localized surface plasmon resonance peak at different wavelength in visible spectrum.

Second, we fabricated various hybrid PEDOT:PSS-Ag-nanoprism thin films by incorporating a certain proportion of those Ag nanoprisms with a main in-plane localized surface plasmon resonance peak at ~ 560 nm.

Third, we performed various characterizations to reveal the effects of the incorporation of Ag nanoprisms and their concentrations on the structural, optical and electrical properties of PEDOT:PSS thin films. The characterization techniques used include transmission electron microscopy, regular and conductive atomic force microscopy, optical absorption, goniophotometry, and four-point probe resistance measurement.

Fourth, through a series of optimizations we fabricated functional organic solar cells based on a blend of P3HT:PCBM. These fabrication conditions allow us to proceed to the next step to study the plasmonic solar cells.

Fifth, pristine and hybrid PEDOT:PSS thin films containing different amount of Ag nanoprisms were applied as anodic buffer layer to fabricate P3HT:PCBM solar cells. We performed photovoltaic characterizations to study the influences of Ag nanoprisms on their performance.

From this study the following effects of the incorporation of Ag nanoprisms on the optical properties of the PEDOT:PSS films were identified:

1. The addition of Ag nanoprisms led to the increased optical absorption in the PEDOT:PSS-Ag-nanoprism thin films. Such optical absorption improvement were controlled by the Ag nanoprisms concentration in PEDOT:PSS films;
2. In hybrid PEDOT:PSS-Ag-nanoprism films more light is scattered at high angles with respect to the incident light direction. The increased light scattering in hybrid films is a promising aspect for more efficient light harvest in organic solar cells.

The following effects of the incorporation of Ag nanoprisms on the structural and electrical properties of the PEDOT:PSS films were identified:

1) Increased surface roughness was found in hybrid films likely due to the formation of Ag agglomerates. Larger proportion of Ag nanoprisms incorporated, larger surface roughness were resulted in hybrid films.

2) Compared to pristine PEDOT:PSS films, the global sheet resistance of the hybrid films increased due to the addition of Ag nanoprisms. Larger proportion of Ag nanoprisms incorporated, larger sheet resistance were found in hybrid films. We postulated that the origin of such increased resistance to be the residual insulating PSS polymers used during the synthesis of Ag nanoprisms. Coherent with our proposition, the sheet resistance in hybrid films can be reduced to a resistance value comparable to or lower than those in pristine films by increasing the extent of nanoprism post-synthesis purification. Similar sheet resistance reduction can also be achieved by applying organic solvent additives into the hybrid PEDOT:PSS solution.

The following effects of the incorporation of Ag nanoprisms on the plasmonic organic solar cell performance were identified:

1) After adding Ag nanoprisms in PEDOT:PSS, the device performance of plasmonic organic solar cells deteriorated probably due to (i) the Ag nanoprisms and their agglomerates at the PEDOT:PSS/photoactive layer interface can act as recombination centers leading to a reduction of shunt resistance, J_{sc} and V_{oc}; (2) the excess PSS due to incompletely purified Ag nanoprisms can lead to increased series resistance and thus lower J_{SC};

2) By incorporating further purified Ag NPSMs and a small amount of glycerol into PEDOT:PSS, the plasmonic organic solar cells show an increase in J_{sc} compared to solar cells without Ag NPSMs. This was attributed to the beneficial effects from either

enhanced light absorption arisen from the localized surface plasmon resonance of Ag nanoprisms or the enhanced charge collection resulted from increased PEDOT:PSS surface area due to the incorporation of Ag nanoprisms.

In conclusion, we found that key factors controlling the performance of plasmonic solar cells using noble metallic nanoparticles (MNPs) include not only the optical properties but also the structural and electrical properties of the resulting hybrid PEDOT:PSS-MNP films. The unique optical properties of localized surface plasmon resonance arisen from noble MNPs enhance the light absorption in organic solar cells by scattering or concentration. However, the impurities and agglomerates of MNPs increase the series resistance and decrease shunt resistance in organic solar cells. Both future progress on colloidal surface chemistry and the optimization on the nanoparticle incorporation process will be needed to produce plasmonic organic solar cells of better performance.

Prospective

Further efforts to improve the device performance of plasmonic solar cell include:

- ✧ Since the Ag agglomerates in PEDOT:PSS act as recombination centers in organic solar cells, methods leading to a better nanoparticle dispersion in PEDOT:PSS solution is need. Besides dispersion methods, filtration process can be used yet it may modify significantly the nanoparticle concentration (if lots of agglomerates exist).
- ✧ In order to study plasmonic organic solar cells, more efficient and more stable pristine P3HT:PCBM solar cells are needed. In this thesis, the observed high series resistance may due to the limited experimental conditions used (e.g. unsuitable or contaminated evaporator). Any defects or contaminants at either the PEDOT:PSS/active-layer or active-layer/top-electrode interfaces will lead to the deterioration of device performance.
- ✧ The insertion position of metallic nanoparticles in organic solar cells is another interesting topic. Besides inserting these nanoparticles in the PEDOT:PSS layer, we also tried another device structure incorporating Ag nanoprisms within the photoactive layer. Further device optimization is however needed to allow conclusive understanding in this device structure (preliminary results on this device structure are described in Appendix V).

- More in-deepth characterizations employing techniques like photoluminescence and photoinduced absorption spectroscopy will be useful to understand the charge generation mechanisms in plasmonic organic solar cells using metallic nanoparticles [3].

Appendix I Ag Nanospheres Synthesis

Besides the synthesis of Ag nanoprisms (Ag NPSMs), in this thesis, we tried to synthesize the Ag nanospheres (Ag NSs) through reduction of $AgNO_3$ by polyethylene glycol (PEG) under heating.

I.1 Principle

PEG is an environmentally benign material and has been widely used as prodrug in the biological and pharmaceutical industries [318].

A so-called term polyol process [319] is applied when using ethylene glycol and diols as reducing agent to synthesize metal nanoparticles (MNPs) at high temperature. The ethylene glycol or diols acts as both solvent and reducing agent, as well as stabilizer in the synthesis, since they can adsorb onto the nanoparticles (NPs) surface [320].

For preparation of Ag NSs through polyol process, the $AgNO_3$ can be dissolved in PEG liquid and be reduced under heating and vigorous stirring [237,320]. The reduction reaction can be possibly expressed as follows [237,321]:

$$Ag^{+}_{(l)} + PEG_{(l)} \rightarrow [Ag(PEG)]^{+}_{(l)} \rightarrow Ag^{0} + H(OCH_2CH_2)_n OCH_2CHO$$

Where index “l” represents liquid state, $[Ag(PEG)]^+$ is the complex of Ag ion and PEG in the liquid suspension, $H(OCH_2CH_2)_{n+1}OH$ is the formula of PEG, and $H(OCH_2CH_2)_nOCH_2CHO$ is oxidation product of PEG.

The typically resulting Ag NS is shown Figure I. 1. The Ag NS is stabilized by PEG through coordinate bond via lone pair electrons of oxygen atoms of PEG.

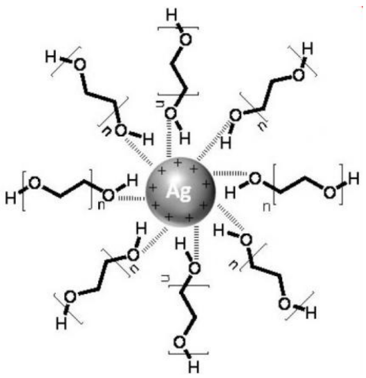

Figure I. 1 Schematic of PEG capped silver nanoparticles [Ag(PEG)] [321].

I.2 Experimental

In a typical process, silver nitrate (0.1 g, $AgNO_3$) is dissolved in PEG (4 g; molecular weight 2000 kDa, solid state at room temperature) at 40 ℃ for 10, 15 and 20 minutes, respectively. The vigorous stirring is used throughout the whole process. The change of the solution color from colorless to yellow or light red indicates the formation of Ag nanoparticles.

I.3 Results

The resulting Ag NP solutions are shown in Figure I. 2. The corresponding absorbance is shown in Figure I. 3. The absorbance peaks at around 400 nm indicate the formation of Ag NSs. The broad absorbance peaks suggest that the NPs have a wide size distribution.

Figure I. 2 Photographs of resulting Ag NP solutions synthesized at 40 ℃ for 10, 15 and 20 minutes (from left to right), respectively.

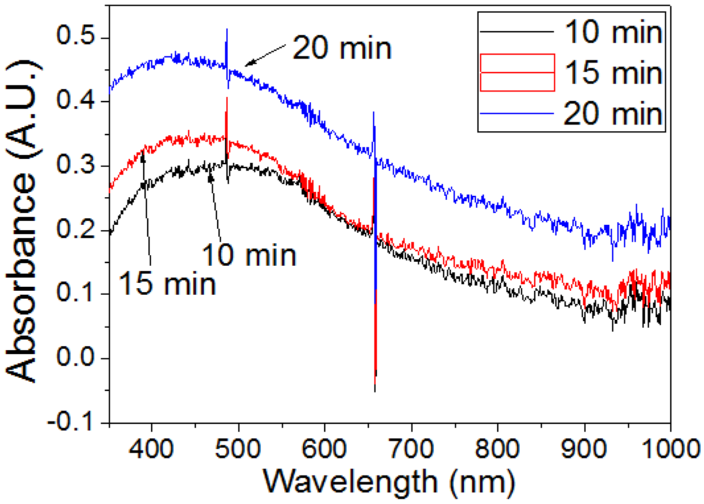

Figure I. 3 Absorbance spectra of the resulting Ag NPs synthesized at 40 ℃ for 10, 15 and 20 minutes, respectively

Appendix II Ag nanoprisms synthesis by one-step thermal reduction

Here we introduce an alternative approach to synthesize Ag nanoprisms (NPSMs) by thermal reduction at room temperature. This is a simplified method and the resulting Ag NPSMs have a unimodal size distribution and their edge lengths are modestly controlled.

III.1 Experimental

The synthesis follows the recipe used in reference [239]. In a typical experiment, aqueous mixture solutions comprising of Silver nitrate ($AgNO_3$; 0.1 mM, 25 mL), trisodium citrate ($Na_3C_6H_5O_7 \cdot 2H_2O$; 30 mM, 1.5 mL), poly(vinylpyrolidone) (PVP, Mw ~ 29000 g/mol; 0.7 mM, 1.5 mL), and hydrogen peroxide (H2O2; 30 wt.-%, 60 µL) were prepared using vigorously stirring at room temperature in ambience air. Different quantities of sodium borohydride ($NaBH_4$; 100 mM) were then rapidly added inside such pre-prepared mixtures, the volume of $NaBH_4$ solutions were 27 µL, 36 µL, 45 µL, 54 µL, 63 µL, 72 µL and 81 µL, respectively, which correspond to 0.3 mM, 0.4 mM, 0.5 mM, 0.6 mM, 0.7 mM, 0.8 mM and 0.9 mM of $NaBH_4$ in the resulting mixtures. After 30 minutes, the color of the solutions changed into yellow or blue from colorless, depending on the concentration of $NaBH_4$ used, indicating the formation of nanoparticles (NPs). Note that stirring and de-ionized (DI) water were used throughout the experiment; the reaction occurred in the dark. In addition, the $NaBH_4$ solution should be freshly prepared.

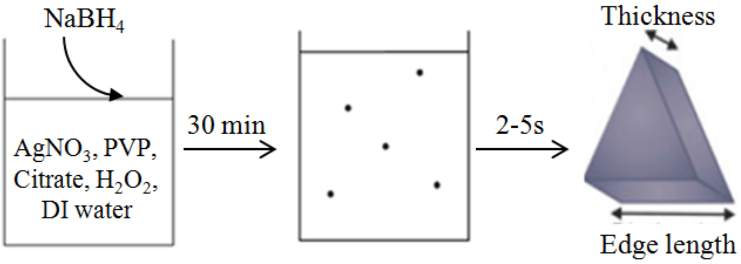

Figure II. 1 The conversion of Ag nanoparticles to Ag NPSMS using $NaBH_4$, H_2O_2, PVP and citrate

III.2 Results

The resulting Ag NPSM solutions are shown in Figure II. 2. The various colors of the solutions suggest varying aspect-ratio of Ag NPSMs. The corresponding absorbance spectra are shown in Figure II. 3. With decreasing NaBH4 concentration in the solution, the absorbance peaks of main in-plane dipoles increasingly res-shift, suggesting that the aspect-ratio of Ag NPSMs increases(except 0.3 mM $NaBH_4$) [233]. Note that the full width at half maximum (FWHM) of the absorbance spectra is quite large, indicating a wide size distribution of Ag NPSMs.

Figure II. 2 Photographs of resulting Ag NPSM solution using different concentration of $NaBH_4$, from left to right: 0.3 mM, 0.4 mM, 0.5 mM, 0.6 mM, 0.7 mM, 0.8 mM and 0.9 mM, respectively.

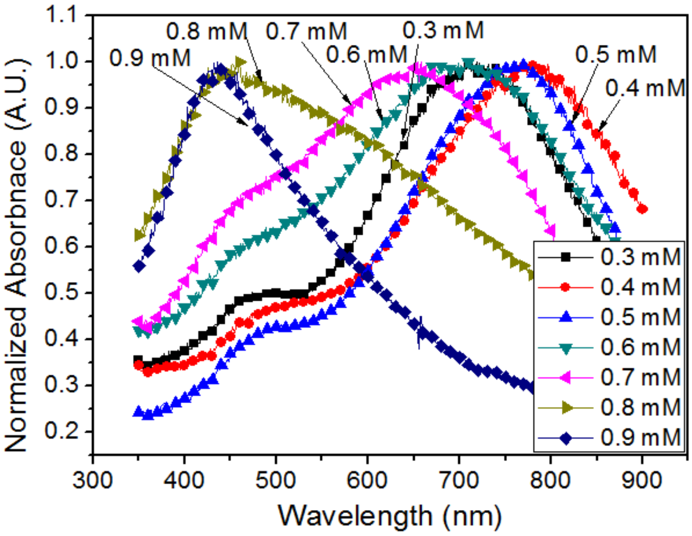

Figure II. 3 Absorbance spectra of Ag NPSM solutions with various $NaBH_4$ concentrations

In the synthesis, the $NaBH_4$ is the reducing agent, the chemical equation for this reduction process could be expressed as follows [263]:

$$AgNO_3 + NaBH_4 \rightarrow Ag^0 + \frac{1}{2}H_2 + \frac{1}{2}B_2H_6 + NaNO_3$$

PVP acts as stabilizer since its oxygen atoms preferentially bind to the {100} facets of Ag [266], and thus preventing Ag nanoparticles from aggregation.

For citrate, it preferentially adsorb onto the Ag {111} facets [239,266] and thus can act as face-selective agent and direct the final triangular shape [239].

H_2O_2 can also affect the shape of the resulting nanoparticles [239]. Without H_2O_2, the obtained nanoparticles are spherical, while by adding a small amount of H_2O_2, the resulting nanoparticles are mixture of nanospheres and nanoprisms.

Appendix III Photovoltaic characteristics of PTB7:PC$_{70}$BM organic solar cell

PTB7 has a lower bandgap (1.8 eV [21]) than P3HT (2.1 eV), so that it has better light absorption ability further into the infrared; PC$_{70}$BM has a higher optical absorption in visible region compared to PC$_{60}$BM [98]. Therefore, a significant improvement of device performance of PTB7:PC$_{70}$BM solar cell is observed compared to P3HT:PC$_{60}$BM solar cell [322].

Appendix III presents the photovoltaic characteristics of PTB7:PC$_{70}$BM OSC using ZnO nanoparticle as optical spacer between photoactive layer and the Al back electrode.

The ZnO has a high electron mobility (0.066 cm^{2}V^{-1}s^{-1}) and a Fermi level of 4.4 eV [307]. These properties provides not only efficient charge transfer from fullerene derivatives, but also effective electron extraction towards to cathode [307,323], as well as reduced contact barrier, and reduced recombination at the cathode [323].

III.1 Experimental

The general fabrication process of OSCs was followed the reference [323] in Centre Interdisciplinaire de Nanoscience de Marseille (CINaM), but some parameters were modified.

First ITO substrates (purchased from OSILLA and LUMTEC) were thoroughly cleaned by ultrasonic bath in acetone and ethanol followed by rinsing with water and ultrasonic bath in isopropanol and applying ultraviolet-ozone for 10 minutes. A thin layer of PEDOT:PSS (CLEVIOS^{TM} Al 4083) was spin-coated on the cleaned ITO-coated glass substrate at the speed of 5000 rpm for 60 s followed by heating on a hot-plate at 150 ℃ for 10 minutes in a nitrogen-filled glove box.

PTB7 (1-Material) and PC$_{70}$BM (Solenne, purity 95%) were solubilized at 50 ℃ over night in chlorobenzene with a weight ratio of 1:1.5 using 10 mg mL^{-1} PTB7. The PTB7: PC$_{70}$BM blend layer, with a nominal thickness of 90 nm, was prepared by spin-coating at 2000 rpm for 30 s. After that, a layer of ZnO nanoparticles with 6 nm as average diameter and a concentration of 2 mg/mL in isopropanol (prepared following reference [323]) was spin-coated on the photoactive layer at 3000 rpm for 60 s. The device was then dried at a hotplate at 75 ℃ for 5 minutes. Note that these two steps were done in nitrogen-filled glove box.

Al cathode (100 nm) was then were thermally evaporated at 2×10^{-6} Torr pressure through a shadow mask and the device area was 0.06 cm^2.

III.2 Photovoltaic characteristics

The resulting photovoltaic *J-V* characteristic curves of PTB7:$PC_{70}BM$ OSCs are shown in Figure III. 1. The PTB7:$PC_{70}BM$ OSCs show a much better device performance than that in Chapter IV with a higher V_{oc} of 0.742 V and a higher J_{sc} of 13.3 with a FF of 53%, leading to a *PCE* of 5.25%. The improvement of device performance could be attributed to the enhanced light absorption due to PTB7 and PC70BM, improved electron extraction, reduced contact barrier, and reduced recombination at the cathode [323].

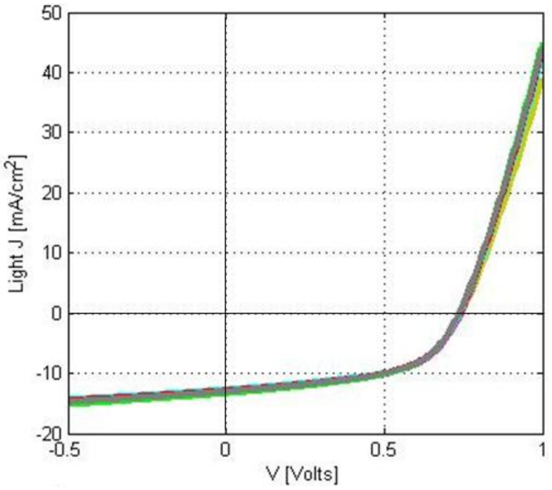

Figure III. 1 Photovoltaic *J-V* characteristic curves of PTB7:$PC_{70}BM$ OSCs under illumination (AM 1.5)

Appendix IV Phase transfer of Ag nanoprisms from aqueous solution into organic solvents

The as-prepared Ag nanoprisms (NPSMs) either in Chapter III or in Appendix II are in aqueous solutions. For applying Ag NPSMs in water-insoluble materials (e.g., P3HT:PCBM), surface modification must be done to transfer Ag NPSMs from aqueous solution to organic solvents.

Since the as-prepared Ag NPSMs are stabilized by citrate in Chapter III (PVP in Appendix II), ligand exchange method can be an effective technique to manage the phase transfer from aqueous solution to organic solvents. The capping agent citrate can provide long term stability, but it is weakly bound to the Ag nanoparticles. Hence, it is readily displaced by various other molecules including thiols, amines, polymers, antibodies, and proteins [324].

Here, we present a phase transfer of Ag NPSMs from aqueous solution into organic solvents using oleylamine (Figure IV. 1) as exchange ligand.

IV.1 Experimental

Experiment 1: 10 mL as-prepared Ag NPS solution washed by THF at 6000 rpm for 15 minutes, precipitate was dissolved in 3 mL DI water, then 3 mL hexane and various volume of oleylamine (0.2, 0.4, 0.6 and 0.8 mL, respectively) were added into these aqueous Ag NPSM solutions. The mixtures were vigorously stirred at 1300 rpm for 30 minutes and let stand for 1 h. The resulting solutions comprised of two layers, the upper layer was the Ag NPSM-hexane solution and the bottom is water subnatant (Figure IV. 1).

Experiment 2: 10 ml as-prepared Ag NPS solution washed by THF at 6000 rpm for 15 minutes, precipitate was dissolved in 3 ml DI water, and then 3ml hexane and 0.2 mL of oleylamine were added. The mixtures were stirred at 1300 rpm for 30 minutes and let stand for 1 h. The upper layer, Ag NPSM-hexane solution, was obtained; then: (1) 0.2 mL organic solvent and 0.8 mL hexane were added into 0.15mL Ag NPSM-hexane solution. Three organic solvents were used here: CB, chloroform (CF) and 1,2-dichlorobenzene (DCB), respectively. These three mixtures were then dispersed using ultrasonic bath for 15 minutes; (2) 1.5 mL ethanol was added into 0.25 mL Ag NPSM-hexane solution with ultrasonic bath for 15 minutes, and then this mixture was centrifuged twice at 8500 rpm for 15 minutes by using ethanol. The resulting precipitate was subsequently dispersed in 1 mL CB, CF or DCB using ultrasonic bath for 30 minutes.

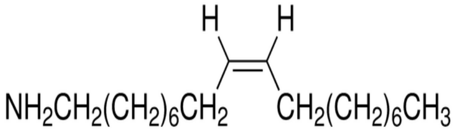

Figure IV. 1 Chemical structure of oleylamine: an amphiphilic ligand

IV.2 Results

IV.2.1 Results of Experiment 1

Different amount of oleylamine was used for phase transfer of Ag NPSMs from aqueous solution to hexane (Figure IV. 2). We noticed that there were many Ag NPSMs are trapped at the interface of the two phases; with increasing the amount of oleylamine, the Ag NPSM-hexane solution (upper layer) became red and the aqueous solution (bottom layer) became emulsion.

The resulting absorbance and normalized absorbance spectra are shown in Figure IV. 3. As shown in left figure in Figure IV. 3, the intensities of the absorbance peaks decrease and plasmon peaks blue-shift slightly with increasing the amount of oleylamine. The decrease in intensity may be probably due to that more Ag NPSMs were trapped in aqueous solution though oleylamine micells (Figure IV. 2). The shift of plasmon peak is also shown in the right figure in Figure IV. 3. The absorbance peaks for Ag NPSM-hexane solutions using 0.2 mL, 0.4 mL, 0.6 mL and 0.8 mL oleylamine are located at about 530 nm, 495 nm, 485 nm and 470 nm, respectively, while the Ag NPSM aqueous solution shows a plasmon peak at 560 nm. According to literature [325], the plasmon peak of nanoparticles is very sensitive to the local refractive index: high index of surrounding medium leads to a red-shift of the plasmon peak. Therefore, the shift of plasmon peak of Ag NPSMs in hexane may be due to the change of local refractive index, since after phase transfer, the Ag NPSMs are presumably stabilized by oleylamine ($n = 1.46$) which has a lower refractive index than citrate ($n = 1.58$). In addition, the Ag NPSMs may be attached by more oleylamine molecules with increasing concentration of oleylamine. This is the possible cause of the further blue-shift of plasmon peaks.

In conclusion, the quantity of 0.2 mL oleylamine (or even less) is possibly appropriate for phase transfer of 10 mL as-prepared Ag NPSMs from aqueous to organic solution.

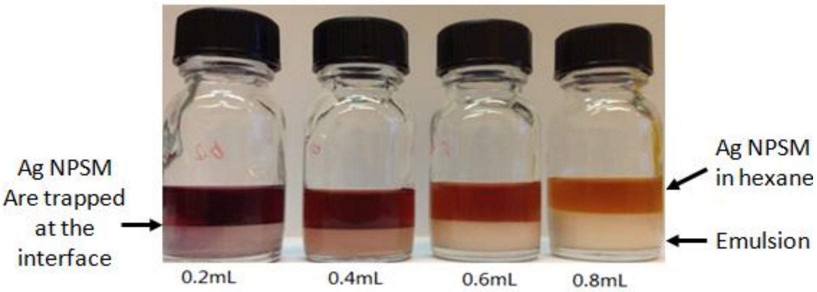

Figure IV. 2 Photographs of Ag NPSM solution after phase transfer using different amount of oleylamine, from left to right: 0.2, 0.4, 0.6 and 0.8 mL, respectively

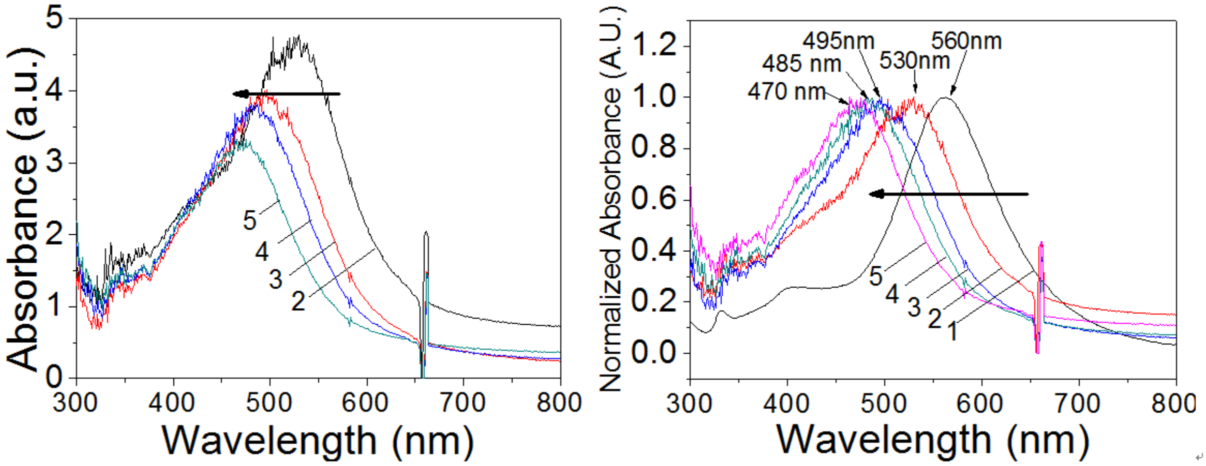

Figure IV. 3 Absorbance and normalized absorbance spectra of Ag NPSM solution after phase transfer using different amount of oleylamine: 0.2, 0.4, 0.6 and 0.8 mL corresponds to curve number 2, 3, 4 and 5, respectively; the curve number 1 is the absorbance of as-prepared Ag NPSM aqueous solution.

IV.2.2 Results of Experiment 2

1) Etching effects

Figure IV. 4 shows the normalized absorbance spectra of Ag NPSM solutions using CF, DCB and CB as solvent, respectively. In Figure IV. 4 (a) and (c), the plasmon peaks blue-shift just 30 minutes after the Ag NPSMs transferred into CF (peak at 480 nm) and CB (peak at 485 nm), and the shift becomes even larger 1 day later (400 nm for CF and 460 nm for CB); in Figure IV. 4 (b), the Ag NPSM solutions show broad peaks, indicating aggregation of Ag NPSMs. Indeed, in Ag nanoparticle-CB/CF solutions, the chloride atoms can be dissociated as chloride ion, and even a trace amount of chloride ion can effectively etch the Ag nanoparticles [266]. This oxidative etching results in a decrease in aspect-ratio (edge length to thickness) of Ag NPSMs and thus a blue-shift [233,326]. Hence, the shift of plasmon peaks may be due to not only the change of local refractive index and but also the chloride ion (Cl^-)-assisted oxidative etching [266,326]. In addition, chloride groups in CF are more active than that in CB and thus more chloride ion are generated in CF, leading to faster oxidative etching, thus a further blue-shift to 400 nm for CF one day after phase transfer (460 nm for CB).

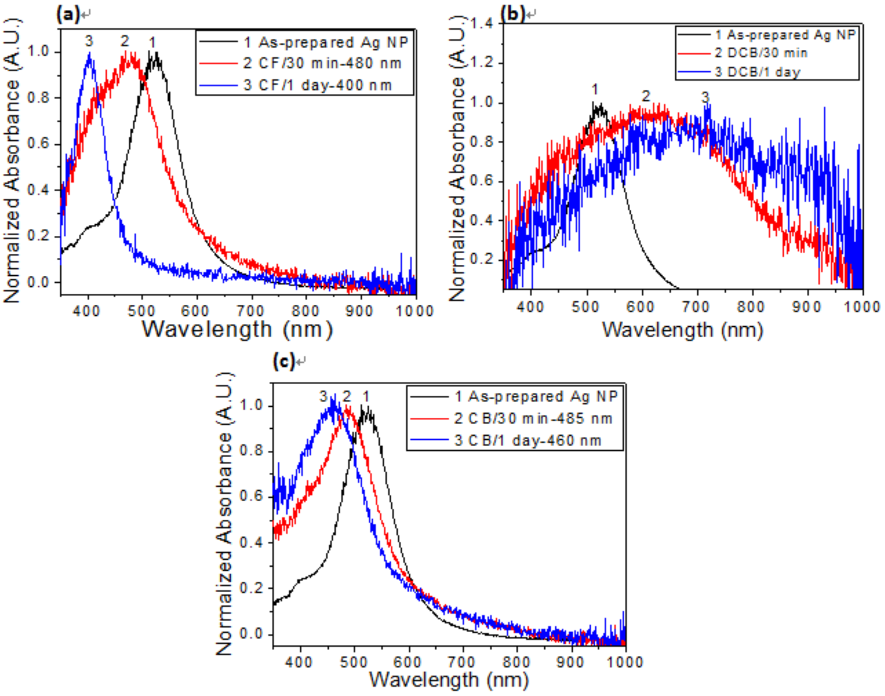

Figure IV. 4 Normalized absorbance spectra of Ag NPSMs transferred in CF, DCB and CB 30 minutes and 1 day later, respectively; the curve number 1 is the absorbance of as-prepared Ag NPSM aqueous solution.

2) Ag NPSMs washed by ethanol

Ag NPSMs were washed by ethanol through centrifugation and then transferred into using CF, DCB and CB. The normalized absorbance spectra of the resulting Ag NPSMs are shown in Figure IV. 5. For CF. The chloride ion-assisted oxidative etching is significant (Figure IV. 5 (a)) and the plasmon peak is blue-shifted to 400 nm just 30 minutes after phase transfer in CF; for DCB, the resulting Ag NPSMs have a broad plasmon peak (Figure IV. 5 (b)), suggesting aggregation of Ag NPSMs in DCB; while for CB, although the line widths become large 30 minutes and 1 day after phase transfer, the plasmon peaks do not shift remarkably (Figure IV. 5 (c)), indicating weaker effect of chloride ion-assisted oxidative etching. Thus, CB could be a good solvent for oleylamine-capped Ag NPSMs for application in OSCs.

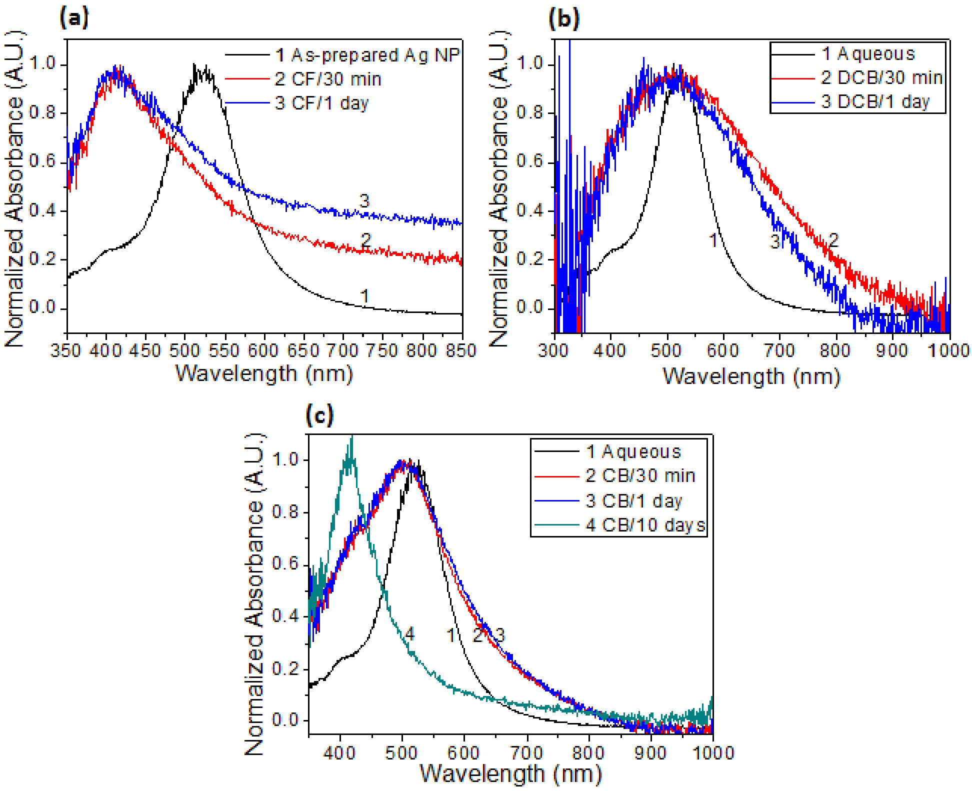

Figure IV. 5 Normalized absorbance spectra of Ag NPSMs in organic solvents. The Ag NPSMs were transferred in hexane and subsequently centrifuged using ethanol and finally dispersed in CF, DCB and CB, respectively; the curve number 1 is the absorbance of as-prepared Ag NPSM aqueous solution.

IV.3 Conclusion

An approach to transfer Ag NPSMs from aqueous solution to organic solvents, especially to CB was developed: 10 mL as-prepared aqueous Ag NPSM solution is centrifuged at 6000 rpm for 15 minutes. The precipitate is then dispersed in 3 mL water and mixed with 3 mL hexane and 0.2 mL oleylamine by vigorous stirring for 30 minutes. After standing for 2 h, the resulting upper layer is washed by ethanol twice through centrifugation at 8500 rpm for 15 minutes. The precipitate is finally dispersed in 1 mL CB by ultrasonic bath for 30 minutes.

Appendix V Plasmonic organic solar cells using Ag nanoprisms in active layer

Besides using Ag nanoprisms (NPSMs) in PEDOT:PSS film, an attempt to incorporate Ag NPSMs into photoactive layer of organic solar cells (OSCs) was made and the results are presented in Appendix V.

V.1Experimental

Preparation of Ag-NPSM-CB solution: For incorporation of Ag NPSMs in photoactive blend, we used the method developed in Appendix IV. 10 mL as-prepared aqueous Ag NPSM solution was centrifuged at 6000 rpm for 15 minutes and then a pellet of Ag NPSMs was obtained at the bottom of the centrifuge tube. Four such pellets of precipitate were then dispersed in 3 mL water and mixed with 3 mL hexane and 0.8 mL oleylamine by vigorous stirring for one night. After standing for 2 h, the resulting upper layer was mixed with ~ 20 mL ethanol by ultrasonic bath for 15 minutes and then washed twice by centrifugation at 8500 rpm for 15 minutes using ethanol. The precipitate was finally dispersed in 0.2 mL chlorobenzene (CB) by ultrasonic bath for 30 minutes.

P3HT:PCBM:CB solution: In parallel, P3HT and PCBM (20 mg P3HT and 20 mg PCBM) was dissolved in 1 mL CB by heating at 45 ℃ for one night with vigorous stirring.

P3HT:PCBM:Ag NPSM:CB solution: After that, the 0.2 mL Ag NPSM-CB solution was mixed with 0.4 mL pre-prepared P3HT:PCBM:CB solution at 45 ℃ for 2 h with vigorous stirring.

Plasmonic OSC: Finally a plasmonic OSC doped with Ag NPSMs in photoactive layer and a control OSC without Ag NPSMs were fabricated following the general process introduced in Section 2.2.2.5.

V.2Results and discussion

Figure V. 1 shows the photovoltaic *J-V* characteristic curves of the control OSC (denoted as pristine) and plasmonic OSC with Ag NPSMs in photoactive layer under AM 1.5 illumination. Compared to the pristine OSC, the J_{sc} decreases dramatically for plasmonic OSC, from 8.58

mA/cm^2 to 4.56 mA/cm^2; the V_{oc} is essentially unchanged; while the *FF* drops from 54% to 27%. The decrease in J_{sc} and *FF* leads to a deterioration of *PCE*, from 2.77% to 0.79%.

The corresponding *EQE*s are shown in Figure V 1. The plasmonic OSC has a much lower *EQE* than the pristine one, consistent with the tendency in J_{sc}.

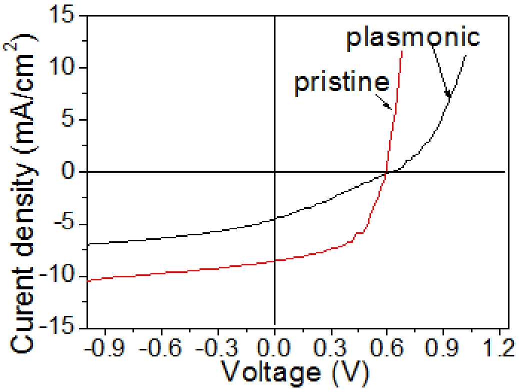

Figure V. 1 *J-V* curves of the control OSC (denoted as pristine) and plasmonic OSC with Ag NPSMs in photoactive layer under AM 1.5 illumination

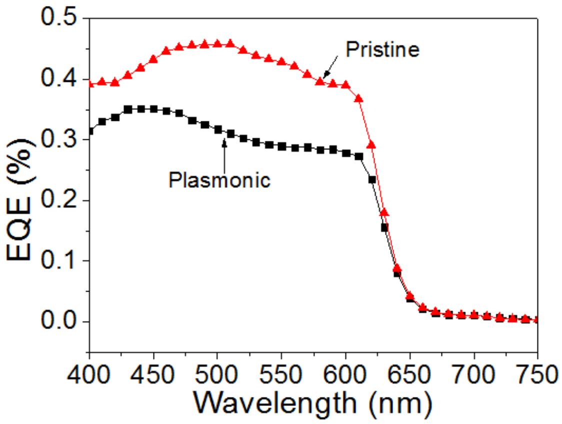

Figure V 1 *EQE* of the control OSC (denoted as pristine) and plasmonic OSC with Ag NPSMs in photoactive layer

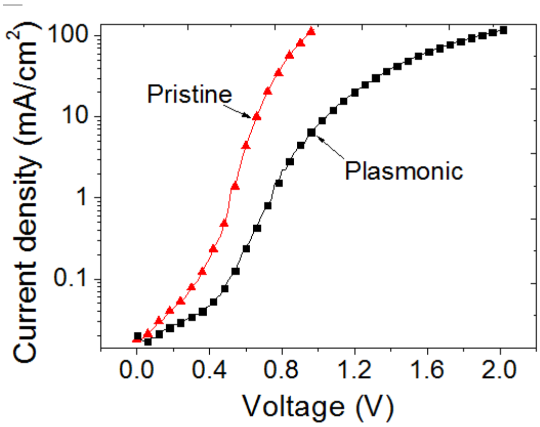

Figure V 2 *J-V* curves of the control OSC (denoted as pristine) and plasmonic OSC with Ag NPSMs in photoactive layer under dark condition.

The decrease in J_{sc} and *EQE* may be due to introduction of oleylamine. The oleylamine has a long hydrocarbon chain and thus it can probably vary the nano-morphology through disturbing the molecular packing, leading to an increased in R_s. In addition, the oleylamine is not conductive. Hence, the introduction of oleylamine in photoactive layer could further increase the series resistance. The increased series resistance is confirmed by the *J*-*V* curves of control OSC and plasmonic OSC under dark condition (Figure V 2).

References

1. BP group, *BP Statistical Review of World Energy 2014* (2014).
2. IEA, *PVPS Report Snapshot of Global PV 1992-2013* (2014).
3. Frederik C. Krebs, ed., *Polymer Photovoltaics: A Practical Approach* (SPIE Press, 2008).
4. A. Gabbard, "Coal Combustion: Nuclear Resource or Danger," http://web.ornl.gov/info/ornlreview/rev26-34/text/colmain.html.
5. D. G. Streets and S. T. Waldhoff, "Present and future emissions of air pollutants in China:SO2 ,NOx, and CO," Atmos. Environ. **34**, 363–374 (2000).
6. S. Hameed and J. Dignon, "Changes in the geographical distributions of global emissions of NOx and SOx from fossil-fuel combustion between 1966 and 1980," Atmos. Environ. **22**, 441–449 (1988).
7. A. E. Becquerel, "Recherches sur les effets de la radiation chimique de la lumiere solaire au moyen des courants electriques," Comptes Rendus L’Academie des Sci. 145–149 (1839).
8. "Solar Cells and Modules," https://energypedia.info/wiki/Solar_Cells_and_Modules.
9. "Photovoltaics Report," http://www.ise.fraunhofer.de/en/downloads-englisch/pdf-files-englisch/photovoltaics-report-slides.pdf.
10. "Best-research cell efficiencies," http://www.nrel.gov/ncpv/images/efficiency_chart.jpg.
11. "The Nobel Prize in Chemistry 2000," http://www.nobelprize.org/nobel_prizes/chemistry/laureates/2000/.
12. C. W. Tang, "Two-layer organic photovoltaic cell," Appl. Phys. Lett. **48**, 183 (1986).
13. N. S. Sariciftci, L. Smilowitz, a. J. Heeger, and F. Wudl, "Semiconducting polymers (as donors) and buckminsterfullerene (as acceptor): photoinduced electron transfer and heterojunction devices," Synth. Met. **59**, 333–352 (1993).
14. G. Yu, K. Pakbaz, and a. J. Heeger, "Semiconducting polymer diodes: Large size, low cost photodetectors with excellent visible-ultraviolet sensitivity," Appl. Phys. Lett. **64**, 3422 (1994).

15. H. Shirakawa, E. J. Louis, A. G. MacDiarmid, C. K. Chiang, and A. J. Heeger, "Synthesis of electrically conducting organic polymers: halogen derivatives of polyacetylene, (CH) x," J. Chem. Soc. Chem. Commun. 578 (1977).
16. C. Chiang, C. F. Jr, and Y. Park, "Electrical conductivity in doped polyacetylene," Phys. Rev. Lett. **39**, 1098–1101 (1977).
17. B. R. Weinberger, M. Akhtar, and S. C. Gau, "Polyacetylene photovoltaic devices," Synth. Met. **4**, 187–197 (1982).
18. S. Glenis, G. Tourillon, and F. Garnier, "Influence of the doping on the photovoltaic properties of thin films of poly-3-methylthiophene," Thin Solid Films **139**, 221–231 (1986).
19. S. Karg, W. Riess, V. Dyakonov, and M. Schwoerer, "Electrical and optical characterization of poly(phenylene-vinylene) light emitting diodes," Synth. Met. **54**, 427–433 (1993).
20. K. P. C. Vollhardt, *Organic Chemistry* (W. H. Freeman, 1987).
21. V. Švrček, T. Yamanari, D. Mariotti, K. Matsubara, and M. Kondo, "Enhancement of hybrid solar cell performance by polythieno [3,4-b]thiophenebenzodithiophene and microplasma-induced surface engineering of silicon nanocrystals," Appl. Phys. Lett. **100**, 223904 (2012).
22. M. Heeney, C. Bailey, K. Genevicius, M. Shkunov, D. Sparrowe, S. Tierney, and I. McCulloch, "Stable polythiophene semiconductors incorporating thieno[2,3-b]thiophene.," J. Am. Chem. Soc. **127**, 1078–9 (2005).
23. L. Fang, Y. Zhou, Y.-X. Yao, Y. Diao, W.-Y. Lee, A. L. Appleton, R. Allen, J. Reinspach, S. C. B. Mannsfeld, and Z. Bao, "Side-Chain Engineering of Isoindigo-Containing Conjugated Polymers Using Polystyrene for High-Performance Bulk Heterojunction Solar Cells," Chem. Mater. **25**, 4874–4880 (2013).
24. C. Kanimozhi, N. Yaacobi-Gross, E. K. Burnett, A. L. Briseno, T. D. Anthopoulos, U. Salzner, and S. Patil, "Use of side-chain for rational design of n-type diketopyrrolopyrrole-based conjugated polymers: what did we find out?," Phys. Chem. Chem. Phys. **16**, 17253–65 (2014).
25. C. J. Brabec, "Organic Photovoltaics. Concepts and Realization by Christoph Joseph Brabec," (2003).
26. "Excitons," http://en.wikipedia.org/wiki/Exciton.

27. S. Alvarado, P. Seidler, D. Lidzey, and D. Bradley, "Direct Determination of the Exciton Binding Energy of Conjugated Polymers Using a Scanning Tunneling Microscope," Phys. Rev. Lett. **81**, 1082–1085 (1998).
28. M. Knupfer, "Exciton binding energies in organic semiconductors," Appl. Phys. A Mater. Sci. Process. **77**, 623–626 (2003).
29. M. Knupfer, J. Fink, E. Zojer, G. Leising, and D. Fichou, "Universal exciton size scaling in π conjugated systems," Chem. Phys. Lett. **318**, 585–589 (2000).
30. J.-J. J. Simon, L. Escoubas, F. Monestier, P. Torchio, and F. F. Flory, "Optical properties engineering for Organic Solar Cells," Int. J. Mater. Prod. Technol. **34**, 469 (2009).
31. A. K. Pandey, J. M. Nunzi, B. Ratier, and A. Moliton, "Size effect on organic optoelectronics devices: Example of photovoltaic cell efficiency," Phys. Lett. A **372**, 1333–1336 (2008).
32. a. Köhler and D. Beljonne, "The Singlet–Triplet Exchange Energy in Conjugated Polymers," Adv. Funct. Mater. **14**, 11–18 (2004).
33. M. C. Scharber, D. Mühlbacher, M. Koppe, P. Denk, C. Waldauf, a. J. Heeger, and C. J. Brabec, "Design Rules for Donors in Bulk-Heterojunction Solar Cells—Towards 10 % Energy-Conversion Efficiency," Adv. Mater. **18**, 789–794 (2006).
34. H. Ohkita, S. Cook, Y. Astuti, W. Duffy, S. Tierney, W. Zhang, M. Heeney, I. McCulloch, J. Nelson, D. D. C. Bradley, and J. R. Durrant, "Charge carrier formation in polythiophene/fullerene blend films studied by transient absorption spectroscopy.," J. Am. Chem. Soc. **130**, 3030–42 (2008).
35. A. Luque and S. Hegedus, eds., *Handbook of Photovoltaic Science and Engineering*, 2nd ed. (John Wiley & Sons, Ltd, 2010).
36. "Air mass," http://en.wikipedia.org/wiki/Air_mass_(solar_energy).
37. S. van Bavel, E. Sourty, G. de With, K. Frolic, and J. Loos, "Relation between Photoactive Layer Thickness, 3D Morphology, and Device Performance in P3HT/PCBM Bulk-Heterojunction Solar Cells," Macromolecules **42**, 7396–7403 (2009).
38. A. J. Moulé, J. B. Bonekamp, and K. Meerholz, "The effect of active layer thickness and composition on the performance of bulk-heterojunction solar cells," J. Appl. Phys. **100**, 094503 (2006).

39. E. Stratakis and E. Kymakis, "Nanoparticle-based plasmonic organic photovoltaic devices," Mater. Today **16**, 133–146 (2013).
40. J.-L. Brédas, J. E. Norton, J. Cornil, and V. Coropceanu, "Molecular understanding of organic solar cells: the challenges.," Acc. Chem. Res. **42**, 1691–9 (2009).
41. "Solar Spectral Irradiance: Air Mass 1.5," http://rredc.nrel.gov/solar/spectra/am1.5/.
42. S. Vedraine, "INTEGRATION de NANOSTRUCTURES PLASMONIQUES au sein de DISPOSITIFS PHOTOVOLTAÏQUES ORGANIQUES : ETUDE NUMERIQUE et EXPERIMENTALE," AIX-MARSEILLE UNIVERSITÉ (2012).
43. T. G. J. van der Hofstad, D. Di Nuzzo, M. van den Berg, R. a. J. Janssen, and S. C. J. Meskers, "Influence of Photon Excess Energy on Charge Carrier Dynamics in a Polymer-Fullerene Solar Cell," Adv. Energy Mater. **2**, 1095–1099 (2012).
44. B. A. Gregg and J. Van De Lagemaat, "Folding photons," **6**, (2012).
45. J. Nelson, "Polymer:fullerene bulk heterojunction solar cells," Mater. Today **14**, 462–470 (2011).
46. J. Nelson, "Polymer:fullerene bulk heterojunction solar cells," Mater. Today **14**, 462–470 (2011).
47. A. E. Jailaubekov, A. P. Willard, J. R. Tritsch, W.-L. Chan, N. Sai, R. Gearba, L. G. Kaake, K. J. Williams, K. Leung, P. J. Rossky, and X.-Y. Zhu, "Hot charge-transfer excitons set the time limit for charge separation at donor/acceptor interfaces in organic photovoltaics.," Nat. Mater. **12**, 66–73 (2013).
48. M. Urien, G. Wantz, E. Cloutet, L. Hirsch, P. Tardy, L. Vignau, H. Cramail, and J.-P. Parneix, "Field-effect transistors based on poly(3-hexylthiophene): Effect of impurities," Org. Electron. **8**, 727–734 (2007).
49. P. Wurfel, *Physics of Solar Cells: From the Principles to New Concepts* (Willey, 2005), p. 129.
50. D. K. Schroder, *Semiconductor Material and Device Characterization*, 3rd ed. (John Wiley & Sons, 2006), p. 128.
51. G. Heimel, L. Romaner, E. Zojer, and J.-L. Bredas, "The interface energetics of self-assembled monolayers on metals.," Acc. Chem. Res. **41**, 721–9 (2008).
52. Y. Y. Kee, S. S. Tan, T. K. Yong, C. H. Nee, S. S. Yap, T. Y. Tou, G. Sáfrán, Z. E. Horváth, J. P. Moscatello, and Y. K. Yap, "Low-temperature synthesis of indium tin oxide nanowires as the transparent electrodes for organic light emitting devices.," Nanotechnology **23**, 025706 (2012).

53. L. Groenendaal, F. Jonas, D. Freitag, H. Pielartzik, and J. R. Reynolds, "Poly(3,4-ethylenedioxythiophene) and Its Derivatives: Past, Present, and Future," Adv. Mater. **12**, 481–494 (2000).

54. M. Dietrich, J. Heinze, G. Heywang, and F. Jonas, "Electrochemical and spectroscopic characterization of polyalkylenedioxythiophenes," J. Electroanal. Chem. **369**, 87–92 (1994).

55. S. Kirchmeyer and K. Reuter, "Scientific importance, properties and growing applications of poly(3,4-ethylenedioxythiophene)," J. Mater. Chem. **15**, 2077 (2005).

56. A. M. Nardes, M. Kemerink, R. a. J. Janssen, J. a. M. Bastiaansen, N. M. M. Kiggen, B. M. W. Langeveld, a. J. J. M. van Breemen, and M. M. de Kok, "Microscopic Understanding of the Anisotropic Conductivity of PEDOT:PSS Thin Films," Adv. Mater. **19**, 1196–1200 (2007).

57. U. Lang, E. Müller, N. Naujoks, and J. Dual, "Microscopical Investigations of PEDOT:PSS Thin Films," Adv. Funct. Mater. **19**, 1215–1220 (2009).

58. E. Vitoratos, S. Sakkopoulos, E. Dalas, N. Paliatsas, D. Karageorgopoulos, F. Petraki, S. Kennou, and S. Choulis, "Thermal degradation mechanisms of PEDOT:PSS," Org. Electron. **10**, 61–66 (2009).

59. H. Frohne, S. E. Shaheen, C. J. Brabec, D. C. Müller, N. S. Sariciftci, and K. Meerholz, "Influence of the anodic work function on the performance of organic solar cells.," Chemphyschem **3**, 795–799 (2002).

60. Z. Su, L. Wang, Y. Li, H. Zhao, B. Chu, and W. Li, "Ultraviolet-ozone-treated PEDOT:PSS as anode buffer layer for organic solar cells.," Nanoscale Res. Lett. **7**, 465 (2012).

61. S.-W. Baek, J. Noh, C.-H. Lee, B. Kim, M.-K. Seo, and J.-Y. Lee, "Plasmonic forward scattering effect in organic solar cells: a powerful optical engineering method.," Sci. Rep. **3**, 1726 (2013).

62. A. M. Nardes, M. Kemerink, M. M. de Kok, E. Vinken, K. Maturova, and R. a. J. Janssen, "Conductivity, work function, and environmental stability of PEDOT:PSS thin films treated with sorbitol," Org. Electron. **9**, 727–734 (2008).

63. J. S. Kim, M. Granström, R. H. Friend, N. Johansson, W. R. Salaneck, R. Daik, W. J. Feast, and F. Cacialli, "Indium–tin oxide treatments for single- and double-layer polymeric light-emitting diodes: The relation between the anode physical, chemical,

and morphological properties and the device performance," J. Appl. Phys. **84**, 6859 (1998).

64. A. Elschner, F. Bruder, H.-W. Heuer, F. Jonas, A. Karbach, S. Kirchmeyer, S. Thurm, and R. Wehrmann, "PEDT/PSS for efficient hole-injection in hybrid organic light-emitting diodes," Synth. Met. **111-112**, 139–143 (2000).
65. A. Yakimov and S. R. Forrest, "High photovoltage multiple-heterojunction organic solar cells incorporating interfacial metallic nanoclusters," Appl. Phys. Lett. **80**, 1667 (2002).
66. J. C. Scott, S. A. Carter, S. Karg, and M. Angelopoulos, "Polymeric anodes for organic light-emitting diodes," Synth. Met. **85**, 1197–1200 (1997).
67. P. Melpignano, A. Baron-Toaldo, V. Biondo, S. Priante, R. Zamboni, M. Murgia, S. Caria, L. Gregoratti, A. Barinov, and M. Kiskinova, "Mechanism of dark-spot degradation of organic light-emitting devices," Appl. Phys. Lett. **86**, 041105 (2005).
68. X. Crispin, S. Marciniak, W. Osikowicz, G. Zotti, A. W. D. van der Gon, F. Louwet, M. Fahlman, L. Groenendaal, F. De Schryver, and W. R. Salaneck, "Conductivity, morphology, interfacial chemistry, and stability of poly(3,4-ethylene dioxythiophene)-poly(styrene sulfonate): A photoelectron spectroscopy study," J. Polym. Sci. Part B Polym. Phys. **41**, 2561–2583 (2003).
69. G. Greczynski, T. Kugler, M. Keil, W. Osikowicz, M. Fahlman, and W. . Salaneck, "Photoelectron spectroscopy of thin films of PEDOT–PSS conjugated polymer blend: a mini-review and some new results," J. Electron Spectros. Relat. Phenomena **121**, 1–17 (2001).
70. J. Hwang, F. Amy, and A. Kahn, "Spectroscopic study on sputtered PEDOT ·PSS: Role of surface PSS layer," Org. Electron. **7**, 387–396 (2006).
71. A. M. Nardes, "On the conductivity of PEDOT:PSS thin films," Eindhoven (2007).
72. "Clevios^{TM} P standard dispersion," http://www.heraeus-clevios.com/media/webmedia_local/media/datenblaetter/81075818_Clevios_P_20101217.pdf.
73. R. C. Hiorns, R. de Bettignies, J. Leroy, S. Bailly, M. Firon, C. Sentein, a. Khoukh, H. Preud’homme, and C. Dagron-Lartigau, "High Molecular Weights, Polydispersities, and Annealing Temperatures in the Optimization of Bulk-Heterojunction Photovoltaic Cells Based on Poly(3-hexylthiophene) or Poly(3-butylthiophene)," Adv. Funct. Mater. **16**, 2263–2273 (2006).

74. B. Friedel, P. E. Keivanidis, T. J. K. Brenner, A. Abrusci, C. R. McNeill, R. H. Friend, and N. C. Greenham, "Effects of Layer Thickness and Annealing of PEDOT:PSS Layers in Organic Photodetectors," Macromolecules **42**, 6741–6747 (2009).

75. S. Ghosh and O. Inganäs, "Nano-structured conducting polymer network based on PEDOT-PSS," Synth. Met. **121**, 1321–1322 (2001).

76. J. Ouyang and Y. Yang, "Conducting Polymer as Transparent Electric Glue," Adv. Mater. **18**, 2141–2144 (2006).

77. J. Huang, P. F. Miller, J. S. Wilson, a. J. de Mello, J. C. de Mello, and D. D. C. Bradley, "Investigation of the Effects of Doping and Post-Deposition Treatments on the Conductivity, Morphology, and Work Function of Poly(3,4-ethylenedioxythiophene)/Poly(styrene sulfonate) Films," Adv. Funct. Mater. **15**, 290–296 (2005).

78. H. Randriamahazaka, F. Vidal, P. Dassonville, C. Chevrot, and D. Teyssié, "Semi-interpenetrating polymer networks based on modified cellulose and poly(3,4-ethylenedioxythiophene)," Synth. Met. **128**, 197–204 (2002).

79. M. C. Morvant and J. R. Reynolds, "In situ conductivity studies of poly(3,4-ethylenedioxythiophene)," Synth. Met. **92**, 57–61 (1998).

80. S. Kirchmeyer and K. Reuter, "Scientific importance, properties and growing applications of poly(3,4-ethylenedioxythiophene)," J. Mater. Chem. **15**, 2077 (2005).

81. J.-S. Yeo, J.-M. Yun, D.-Y. Kim, S. Park, S.-S. Kim, M.-H. Yoon, T.-W. Kim, and S.-I. Na, "Significant Vertical Phase Separation in Solvent-Vapor-Annealed Poly(3,4-ethylenedioxythiophene):Poly(styrene sulfonate) Composite Films Leading to Better Conductivity and Work Function for High-Performance Indium Tin Oxide-Free Optoelectronics.," ACS Appl. Mater. Interfaces (2012).

82. A. Nardes, M. Kemerink, and R. Janssen, "Anisotropic hopping conduction in spin-coated PEDOT:PSS thin films," Phys. Rev. B **76**, 085208 (2007).

83. J.-L. Wu, F.-C. Chen, Y.-S. Hsiao, F.-C. Chien, P. Chen, C.-H. Kuo, M. H. Huang, and C.-S. Hsu, "Surface plasmonic effects of metallic nanoparticles on the performance of polymer bulk heterojunction solar cells.," ACS Nano **5**, 959–67 (2011).

84. B. V. K. Naidu, J. S. Park, S. C. Kim, S.-M. Park, E.-J. Lee, K.-J. Yoon, S. Joon Lee, J. Wook Lee, Y.-S. Gal, and S.-H. Jin, "Novel hybrid polymer photovoltaics made by generating silver nanoparticles in polymer:fullerene bulk-heterojunction structures," Sol. Energy Mater. Sol. Cells **92**, 397–401 (2008).

85. C.-H. Kim, S.-H. Cha, S. C. Kim, M. Song, J. Lee, W. S. Shin, S.-J. Moon, J. H. Bahng, N. a Kotov, and S.-H. Jin, "Silver nanowire embedded in P3HT:PCBM for high-efficiency hybrid photovoltaic device applications.," ACS Nano **5**, 3319–25 (2011).
86. A. Elschner, *PEDOT Principles and Applications of an Intrinsically Conductive Polymer* (Taylor and Francis Group, LLC, 2011).
87. A. Assadi, C. Svensson, M. Willander, and O. Inganäs, "Field-effect mobility of poly(3-hexylthiophene)," Appl. Phys. Lett. **53**, 195 (1988).
88. T. A. Chen and R. D. Rieke, "The first regioregular head-to-tail poly(3-hexylthiophene-2,5-diyl) and a regiorandom isopolymer: nickel versus palladium catalysis of 2(5)-bromo-5(2)-(bromozincio)-3-hexylthiophene polymerization," J. Am. Chem. Soc. **114**, 10087–10088 (1992).
89. R. D. McCullough, "The Chemistry of Conducting Polythiophenes," Adv. Mater. **10**, 93–116 (1998).
90. R. D. McCullough and R. D. Lowe, "Enhanced electrical conductivity in regioselectively synthesized poly(3-alkylthiophenes)," J. Chem. Soc. Chem. Commun. 70 (1992).
91. H. Sirringhaus, "Integrated Optoelectronic Devices Based on Conjugated Polymers," Science (80-.). **280**, 1741–1744 (1998).
92. B. S. Ong, Y. Wu, Y. Li, P. Liu, and H. Pan, "Thiophene polymer semiconductors for organic thin-film transistors.," Chemistry **14**, 4766–78 (2008).
93. P. G. Nicholson, V. Ruiz, J. V Macpherson, and P. R. Unwin, "Effect of composition on the conductivity and morphology of poly(3-hexylthiophene)/gold nanoparticle composite Langmuir-Schaeffer films.," Phys. Chem. Chem. Phys. **8**, 5096–105 (2006).
94. T. Erb, U. Zhokhavets, G. Gobsch, S. Raleva, B. Stühn, P. Schilinsky, C. Waldauf, and C. J. Brabec, "Correlation Between Structural and Optical Properties of Composite Polymer/Fullerene Films for Organic Solar Cells," Adv. Funct. Mater. **15**, 1193–1196 (2005).
95. Z. Bao, A. Dodabalapur, and A. J. Lovinger, "Soluble and processable regioregular poly(3-hexylthiophene) for thin film field-effect transistor applications with high mobility," Appl. Phys. Lett. **69**, 4108 (1996).
96. H. N. Tsao and K. Müllen, "Improving polymer transistor performance via morphology control.," Chem. Soc. Rev. **39**, 2372–86 (2010).

97. R. J. Kline and M. D. McGehee, "Morphology and Charge Transport in Conjugated Polymers," J. Macromol. Sci. Part C Polym. Rev. **46**, 27–45 (2006).
98. D. Kronholm and J. C. Hummelen, "Fullerene-Based n-Type Semiconductors in Organic Electronics," http://www.sigmaaldrich.com/technical-documents/articles/material-matters/fullerene-based-n-type.html.
99. L.-M. Chen, Z. Hong, G. Li, and Y. Yang, "Recent Progress in Polymer Solar Cells: Manipulation of Polymer:Fullerene Morphology and the Formation of Efficient Inverted Polymer Solar Cells," Adv. Mater. **21**, 1434–1449 (2009).
100. P. Peumans, A. Yakimov, and S. R. Forrest, "Small molecular weight organic thin-film photodetectors and solar cells," J. Appl. Phys. **93**, 3693 (2003).
101. S. Cataldo and B. Pignataro, "Polymeric Thin Films for Organic Electronics: Properties and Adaptive Structures," Materials (Basel). **6**, 1159–1190 (2013).
102. J. Liu, Y. Shi, and Y. Yang, "Solvation-Induced Morphology Effects on the Performance of Polymer-Based Photovoltaic Devices," Adv. Funct. Mater. **11**, 420 (2001).
103. Z. Hu and A. J. Gesquiere, "PCBM concentration dependent morphology of P3HT in composite P3HT/PCBM nanoparticles," Chem. Phys. Lett. **476**, 51–55 (2009).
104. W. Hammed, R. Yahya, A. Bola, and H. Mahmud, "Recent Approaches to Controlling the Nanoscale Morphology of Polymer-Based Bulk-Heterojunction Solar Cells," Energies **6**, 5847–5868 (2013).
105. T. Wang, A. D. F. Dunbar, P. a. Staniec, A. J. Pearson, P. E. Hopkinson, J. E. MacDonald, S. Lilliu, C. Pizzey, N. J. Terrill, A. M. Donald, A. J. Ryan, R. a. L. Jones, and D. G. Lidzey, "The development of nanoscale morphology in polymer:fullerene photovoltaic blends during solvent casting," Soft Matter **6**, 4128 (2010).
106. N. Camaioni, M. Catellani, S. Luzzati, and A. Migliori, "Morphological characterization of poly(3-octylthiophene):plasticizer:C60 blends," Thin Solid Films **403-404**, 489–494 (2002).
107. C. D. Dimitrakopoulos and P. R. L. Malenfant, "Organic Thin Film Transistors for Large Area Electronics," Adv. Mater. **14**, 99–117 (2002).
108. E. Verploegen, C. E. Miller, K. Schmidt, Z. Bao, and M. F. Toney, "Manipulating the Morphology of P3HT–PCBM Bulk Heterojunction Blends with Solvent Vapor Annealing," Chem. Mater. **24**, 3923–3931 (2012).

109. P. G. Karagiannidis, S. Kassavetis, C. Pitsalidis, and S. Logothetidis, "Thermal annealing effect on the nanomechanical properties and structure of P3HT:PCBM thin films," Thin Solid Films **519**, 4105–4109 (2011).

110. H. Kim, W.-W. W. So, and S. S.-J. MOON, "Effect of thermal annealing on the performance of P3HT/PCBM polymer photovoltaic cells," J. Korean Phys. Soc. **48**, 441–445 (2006).

111. M. T. Dang, L. Hirsch, and G. Wantz, "P3HT:PCBM, Best Seller in Polymer Photovoltaic Research," Adv. Mater. **23**, 3597–3602 (2011).

112. G. Dennler, M. C. Scharber, and C. J. Brabec, "Polymer-Fullerene Bulk-Heterojunction Solar Cells," Adv. Mater. **21**, 1323–1338 (2009).

113. F. B. Kooistra, V. D. Mihailetchi, L. M. Popescu, D. Kronholm, P. W. M. Blom, and J. C. Hummelen, "New C 84 Derivative and Its Application in a Bulk Heterojunction Solar Cell," Chem. Mater. **18**, 3068–3073 (2006).

114. H. Hoppe and N. S. Sariciftci, "Organic solar cells: An overview," J. Mater. Res. **19**, 1924–1945 (2011).

115. I. D. Parker, "Carrier tunneling and device characteristics in polymer light-emitting diodes," J. Appl. Phys. **75**, 1656 (1994).

116. D. I. K. Petritsch, "Organic Solar Cell Architectures," University of Cambridge, United Kingdom (2000).

117. Y. S. Park, E. Kim, B. Hong, and J. Lee, "Characteristics of ITO films with oxygen plasma treatment for thin film solar cell applications," Mater. Res. Bull. **48**, 5115–5120 (2013).

118. S. Jang, H. Chae, H. Kim, and C. Kim, "Simultaneous Oxygen Plasma and Thermal Treatments of an ITO Surface to Improve the Electrical Characteristics of Organic Light-Emitting Diodes," J. Korean Phys. Soc. **51**, 956–962 (2007).

119. L. Zang, *Energy Efficiency and Renewable Energy Through Nanotechnology* (Springer, 2011).

120. C. J. Brabec, A. Cravino, D. Meissner, N. S. Sariciftci, T. Fromherz, M. T. Rispens, L. Sanchez, and J. C. Hummelen, "Origin of the Open Circuit Voltage of Plastic Solar Cells," Adv. Funct. Mater. **11**, 374–380 (2001).

121. C. . Brabec, A. Cravino, D. Meissner, N. . Sariciftci, M. . Rispens, L. Sanchez, J. . Hummelen, and T. Fromherz, "The influence of materials work function on the open circuit voltage of plastic solar cells," Thin Solid Films **403-404**, 368–372 (2002).

122. V. D. Mihailetchi, P. W. M. Blom, J. C. Hummelen, and M. T. Rispens, "Cathode dependence of the open-circuit voltage of polymer:fullerene bulk heterojunction solar cells," J. Appl. Phys. **94**, 6849 (2003).

123. L. J. a. Koster, V. D. Mihailetchi, R. Ramaker, and P. W. M. Blom, "Light intensity dependence of open-circuit voltage of polymer:fullerene solar cells," Appl. Phys. Lett. **86**, 123509 (2005).

124. J. D. Servaites, M. a. Ratner, and T. J. Marks, "Practical efficiency limits in organic photovoltaic cells: Functional dependence of fill factor and external quantum efficiency," Appl. Phys. Lett. **95**, 163302 (2009).

125. M. C. Scharber and N. S. Sariciftci, "Efficiency of bulk-heterojunction organic solar cells.," Prog. Polym. Sci. **38**, 1929–1940 (2013).

126. D. Credgington and J. R. Durrant, "Insights from Transient Optoelectronic Analyses on the Open-Circuit Voltage of Organic Solar Cells," J. Phys. Chem. Lett. **3**, 1465–1478 (2012).

127. P. Schilinsky, "Simulation of light intensity dependent current characteristics of polymer solar cells," J. Appl. Phys. **95**, 2816 (2004).

128. J. Peet, J. Y. Kim, N. E. Coates, W. L. Ma, D. Moses, a J. Heeger, and G. C. Bazan, "Efficiency enhancement in low-bandgap polymer solar cells by processing with alkane dithiols.," Nat. Mater. **6**, 497–500 (2007).

129. D. Gupta, S. Mukhopadhyay, and K. S. Narayan, "Fill factor in organic solar cells," Sol. Energy Mater. Sol. Cells **94**, 1309–1313 (2010).

130. M. Chegaar and Z. Ouennoughi, "Determination of solar cells parameters under illuminated conditions," J. Electron Devices **2**, 17–21 (2003).

131. C. Zhang, J. Zhang, Y. Hao, Z. Lin, and C. Zhu, "A simple and efficient solar cell parameter extraction method from a single current-voltage curve," J. Appl. Phys. **110**, 064504 (2011).

132. M.-S. Kim, B.-G. Kim, and J. Kim, "Effective variables to control the fill factor of organic photovoltaic cells.," ACS Appl. Mater. Interfaces **1**, 1264–9 (2009).

133. D.-H. Ko, J. R. Tumbleston, L. Zhang, S. Williams, J. M. DeSimone, R. Lopez, and E. T. Samulski, "Photonic crystal geometry for organic solar cells.," Nano Lett. **9**, 2742–6 (2009).

134. S. Chanyawadee, R. Harley, M. Henini, D. Talapin, and P. Lagoudakis, "Photocurrent Enhancement in Hybrid Nanocrystal Quantum-Dot p-i-n Photovoltaic Devices," Phys. Rev. Lett. **102**, 077402 (2009).
135. K. R. Catchpole and a Polman, "Plasmonic solar cells.," Opt. Express **16**, 21793–800 (2008).
136. H. A. Atwater and A. Polman, "Plasmonics for improved photovoltaic devices.," Nat. Mater. **9**, 865 (2010).
137. A. Tao, F. Kim, C. Hess, J. Goldberger, R. He, Y. Sun, Y. Xia, and P. Yang, "Langmuir−Blodgett Silver Nanowire Monolayers for Molecular Sensing Using Surface-Enhanced Raman Spectroscopy," Nano Lett. **3**, 1229–1233 (2003).
138. S. a. Maier and H. a. Atwater, "Plasmonics: Localization and guiding of electromagnetic energy in metal/dielectric structures," J. Appl. Phys. **98**, 011101 (2005).
139. H. Choi, S.-J. Ko, Y. Choi, P. Joo, T. Kim, B. R. Lee, J.-W. Jung, H. J. Choi, M. Cha, J.-R. Jeong, I.-W. Hwang, M. H. Song, B.-S. Kim, and J. Y. Kim, "Versatile surface plasmon resonance of carbon-dot-supported silver nanoparticles in polymer optoelectronic devices," Nat. Photonics **7**, 732–738 (2013).
140. E. Stratakis and E. Kymakis, "Nanoparticle-based plasmonic organic photovoltaic devices," Mater. Today **16**, 133–146 (2013).
141. A. Sayigh, S. Pillai, and M. A. Green, "Plasmonics for Photovoltaics," in *Comprehensive Renewable Energy* (2012), pp. 641–656.
142. D. Pines, "Collective energy losses in solids," Rev. Mod. Phys. **28**, 184–199 (1956).
143. R. A. Ferrell, "Predicted Radiation of Plasma Oscillations in Metal Films," Phys. Rev. **111**, 1214 (1958).
144. R. H. Ritchie and H. B. Eldridge, "Optical Emission from Irradiated Foils. I," Phys. Rev. **126**, 1935 (1962).
145. L. Tonks and I. Langmuir, "Oscillations in ionized gases," Phys. Rev. **33**, 195 (1929).
146. C. Kittel, *Introduction to Solid State Physics*, 7th ed. (Wiley, 1995).
147. U. Kreibig and M. Vollmer, *Optical Properties of Metal Clusters*, Springer Series in Materials Science (Springer Berlin Heidelberg, 1995), Vol. 25.
148. F. Wooten, *OPTICAL PROPERTIES OF SOLIDS* (ACADEMIC PRESS, 1972).
149. C. Bréchignac, P. Houdy, and M. Lahmani, *Nanomaterials and Nanochemistry* (Springer Science & Business Media, 2008), p. 777.

150. E. Kretschmann, "The Determination of the Optical Constants of Metals by Excitation of Surface Plasmons," Zeitschrift für Phys. **241**, 313–324 (1971).

151. R. J. Gale, *Spectroelectrochemistry: Theory and Practice* (Springer Science & Business Media, 1988).

152. E. Devaux, T. W. Ebbesen, J.-C. Weber, and " A. D., "Launching and decoupling surface plasmons via micro-gratings," Appl. Phys. Lett. **83**, 4936 (2003).

153. "Plasmons in metal nanostructures," (2001).

154. C. F. Bohren and D. R. Huffman, *Absorption and Scattering of Light by Small Particles* (Wiley-VCH Verlag GmbH, 1998).

155. Y. Zhi, L. I. Xiu, and H. U. Jian, "The Size and Shape Effects on the Optical Properties of Gold Nanoparticles," 1–5 (2003).

156. E. Stefan Kooij and B. Poelsema, "Shape and size effects in the optical properties of metallic nanorods.," Phys. Chem. Chem. Phys. **8**, 3349–57 (2006).

157. C. Noguez, "Surface Plasmons on Metal Nanoparticles: The Influence of Shape and Physical Environment," J. Phys. Chem. C **111**, 3806–3819 (2007).

158. S. Link, Z. L. Wang, and M. a. El-Sayed, "Alloy Formation of Gold−Silver Nanoparticles and the Dependence of the Plasmon Absorption on Their Composition," J. Phys. Chem. B **103**, 3529–3533 (1999).

159. L. J. Sherry, S.-H. Chang, G. C. Schatz, R. P. Van Duyne, B. J. Wiley, and Y. Xia, "Localized surface plasmon resonance spectroscopy of single silver nanocubes.," Nano Lett. **5**, 2034–8 (2005).

160. K.-S. Lee and M. A. El-Sayed, "Dependence of the enhanced optical scattering efficiency relative to that of absorption for gold metal nanorods on aspect ratio, size, end-cap shape, and medium refractive index.," J. Phys. Chem. B **109**, 20331–8 (2005).

161. M. M. Alvarez, J. T. Khoury, T. G. Schaaff, M. N. Shafigullin, I. Vezmar, and R. L. Whetten, "Optical Absorption Spectra of Nanocrystal Gold Molecules," **5647**, 3706–3712 (1997).

162. P. K. Jain, "Plasmons in assembled metal nanostructures: radiative and nonradiative properties, near-field coupling and its universal scaling behavior," Georgia Institute of Technology (2008).

163. S. Link and M. a. El-Sayed, "Size and Temperature Dependence of the Plasmon Absorption of Colloidal Gold Nanoparticles," J. Phys. Chem. B **103**, 4212–4217 (1999).

164. C. Sönnichsen, T. Franzl, T. Wilk, G. von Plessen, and J. Feldmann, "Drastic Reduction of Plasmon Damping in Gold Nanorods," Phys. Rev. Lett. **88**, 077402 (2002).
165. D. Aherne, D. M. Ledwith, M. Gara, and J. M. Kelly, "Optical Properties and Growth Aspects of Silver Nanoprisms Produced by a Highly Reproducible and Rapid Synthesis at Room Temperature," Adv. Funct. Mater. **18**, 2005–2016 (2008).
166. M. Meier and A. Wokaun, "Enhanced fields on large metal particles: dynamic depolarization," Opt. Lett. **8**, 581 (1983).
167. A. Wokaun, J. P. Gordon, and P. F. Liao, "Radiation Damping in Surface-Enhanced Raman Scattering," Phys. Rev. Lett. **48**, 957–960 (1982).
168. A. J. Haes, C. L. Haynes, A. D. Mcfarland, and G. C. Schatz, "Plasmonic Materials for Surface-Enhanced Sensing and," **30**, (2005).
169. K. L. Kelly, E. Coronado, L. L. Zhao, and G. C. Schatz, "The Optical Properties of Metal Nanoparticles: The Influence of Size, Shape, and Dielectric Environment," J. Phys. Chem. B **107**, 668–677 (2003).
170. X. Zhang, E. M. Hicks, J. Zhao, G. C. Schatz, and R. P. Van Duyne, "Electrochemical Tuning of Silver Nanoparticles Fabricated by Nanosphere Lithography," Nano Lett. **5**, 1503–1507 (2005).
171. E. Hao, G. C. Schatz, and J. T. Hupp, "Synthesis and optical properties of anisotropic metal nanoparticles.," J. Fluoresc. **14**, 331–41 (2004).
172. S. Link, M. B. Mohamed, and M. A. El-Sayed, "Simulation of the Optical Absorption Spectra of Gold Nanorods as a Function of Their Aspect Ratio and the Effect of the Medium Dielectric Constant," J. Phys. Chem. B **103**, 3073–3077 (1999).
173. S. W. Prescott and P. Mulvaney, "Gold nanorod extinction spectra," J. Appl. Phys. **99**, 123504 (2006).
174. H. Wang, G. P. Goodrich, F. Tam, C. Oubre, P. Nordlander, and N. J. Halas, "Controlled texturing modifies the surface topography and plasmonic properties of Au nanoshells.," J. Phys. Chem. B **109**, 11083–7 (2005).
175. A. D. McFarland and R. P. Van Duyne, "Single Silver Nanoparticles as Real-Time Optical Sensors with Zeptomole Sensitivity," Nano Lett. **3**, 1057–1062 (2003).
176. P. Mulvaney, J. Pérez-Juste, M. Giersig, L. M. Liz-Marzán, and C. Pecharromán, "Drastic Surface Plasmon Mode Shifts in Gold Nanorods Due to Electron Charging," Plasmonics **1**, 61–66 (2006).

177. S. Link and M. A. El-Sayed, "Optical properties and ultrafast dynamics of metallic nanocrystals.," Annu. Rev. Phys. Chem. **54**, 331–66 (2003).

178. H. Hövel, S. Fritz, A. Hilger, U. Kreibig, and M. Vollmer, "Width of cluster plasmon resonances: Bulk dielectric functions and chemical interface damping," Phys. Rev. B **48**, 18178–18188 (1993).

179. A. J. Haes and R. P. Van Duyne, "A Nanoscale Optical Biosensor: Sensitivity and Selectivity of an Approach Based on the Localized Surface Plasmon Resonance Spectroscopy of Triangular Silver Nanoparticles," J. Am. Chem. Soc. **124**, 10596–10604 (2002).

180. T. Jensen, L. Kelly, A. Lazarides, and G. C. Schatz, "Electrodynamics of Noble Metal Nanoparticles and Nanoparticle Clusters," J. Clust. Sci. **10**, 295–317 (1999).

181. M. Rights, "Optical properties of metal nanoparticles and their influence on silicon solar cells," UNIVERSITY OF SOUTHAMPTON FACULTY (2009).

182. W. Rechberger, a. Hohenau, a. Leitner, J. R. Krenn, B. Lamprecht, and F. R. Aussenegg, "Optical properties of two interacting gold nanoparticles," Opt. Commun. **220**, 137–141 (2003).

183. K. Sokolov, M. Follen, J. Aaron, I. Pavlova, A. Malpica, R. Lotan, and R. Richards-Kortum, "Real-time vital optical imaging of precancer using anti-epidermal growth factor receptor antibodies conjugated to gold nanoparticles.," Cancer Res. **63**, 1999–2004 (2003).

184. X. Wu, J. Zhang, J. Chen, C. Zhao, and Q. Gong, "Refractive index sensor based on surface-plasmon interference," Opt. Lett. **34**, 392 (2009).

185. M. Moskovits, "Surface-enhanced spectroscopy," Rev. Mod. Phys. **57**, 783–826 (1985).

186. W. Huang, W. Qian, and M. A. El-Sayed, "Photothermal reshaping of prismatic Au nanoparticles in periodic monolayer arrays by femtosecond laser pulses," J. Appl. Phys. **98**, 114301 (2005).

187. K. R. Catchpole and a. Polman, "Design principles for particle plasmon enhanced solar cells," Appl. Phys. Lett. **93**, 191113 (2008).

188. S. Pillai and M. A. Green, "Plasmonics for photovoltaic applications," Sol. Energy Mater. Sol. Cells **94**, 1481–1486 (2010).

189. G. D. Spyropoulos, M. M. Stylianakis, E. Stratakis, and E. Kymakis, "Organic bulk heterojunction photovoltaic devices with surfactant-free Au nanoparticles embedded in the active layer," Appl. Phys. Lett. **100**, 213904 (2012).

190. E. Stratakis and E. Kymakis, "Nanoparticle-based plasmonic organic photovoltaic devices," Mater. Today **16**, 133–146 (2013).

191. K. Topp, H. Borchert, F. Johnen, A. V Tunc, M. Knipper, E. von Hauff, J. Parisi, and K. Al-Shamery, "Impact of the incorporation of Au nanoparticles into polymer/fullerene solar cells.," J. Phys. Chem. A **114**, 3981–9 (2010).

192. H. Shen, P. Bienstman, and B. Maes, "Plasmonic absorption enhancement in organic solar cells with thin active layers," J. Appl. Phys. **106**, 073109 (2009).

193. M. Xue, L. Li, B. J. Tremolet de Villers, H. Shen, J. Zhu, Z. Yu, A. Z. Stieg, Q. Pei, B. J. Schwartz, and K. L. Wang, "Charge-carrier dynamics in hybrid plasmonic organic solar cells with Ag nanoparticles," Appl. Phys. Lett. **98**, 253302 (2011).

194. M. D. Brown, T. Suteewong, R. S. S. Kumar, V. D'Innocenzo, A. Petrozza, M. M. Lee, U. Wiesner, and H. J. Snaith, "Plasmonic dye-sensitized solar cells using core-shell metal-insulator nanoparticles.," Nano Lett. **11**, 438–45 (2011).

195. D. D. S. Fung, L. Qiao, W. C. H. Choy, C. Wang, W. E. I. Sha, F. Xie, and S. He, "Optical and electrical properties of efficiency enhanced polymer solar cells with Au nanoparticles in a PEDOT–PSS layer," J. Mater. Chem. **21**, 16349 (2011).

196. N. G. Semaltianos, W. Perrie, S. Romani, R. J. Potter, G. Dearden, and K. G. Watkins, "Polymer-nanoparticle composites composed of PEDOT:PSS and nanoparticles of Ag synthesised by laser ablation," Colloid Polym. Sci. **290**, 213–220 (2012).

197. J. Yang, J. You, C.-C. Chen, W.-C. Hsu, H. Tan, X. W. Zhang, Z. Hong, and Y. Yang, "Plasmonic polymer tandem solar cell.," ACS Nano **5**, 6210–7 (2011).

198. S. Vedraine, P. Torchio, A. Merlen, J. Bagierek, F. Flory, A. Sangar, and L. Escoubas, "Optical characterization of organic blend films integrating metallic nanoparticles," Sol. Energy Mater. Sol. Cells **102**, 31–35 (2012).

199. A. Sangar, A. Merlen, P. Torchio, S. Vedraine, F. Flory, L. Escoubas, L. Patrone, G. Delafosse, V. Chevallier, E. Moyen, and M. Hanbucken, "Fabrication and characterization of large metallic nanodots arrays for organic thin film solar cells using anodic aluminum oxide templates," Sol. Energy Mater. Sol. Cells **117**, 657–662 (2013).

200. S. Shahin, P. Gangopadhyay, and R. A. Norwood, "Ultrathin organic bulk heterojunction solar cells: Plasmon enhanced performance using Au nanoparticles," Appl. Phys. Lett. **101**, 053109 (2012).

201. W.-J. Yoon, K.-Y. Jung, J. Liu, T. Duraisamy, R. Revur, F. L. Teixeira, S. Sengupta, and P. R. Berger, "Plasmon-enhanced optical absorption and photocurrent in organic bulk heterojunction photovoltaic devices using self-assembled layer of silver nanoparticles," Sol. Energy Mater. Sol. Cells **94**, 128–132 (2010).

202. H. Liu, W.-P. Goh, M.-Y. Leung, Y. Li, and T. B. Norsten, "Effect of nanoparticle stabilizing ligands and ligand-capped gold nanoparticles in polymer solar cells," Sol. Energy Mater. Sol. Cells **96**, 302–306 (2012).

203. G. D. Spyropoulos, M. Stylianakis, E. Stratakis, and E. Kymakis, "Plasmonic organic photovoltaics doped with metal nanoparticles," Photonics Nanostructures - Fundam. Appl. **9**, 184–189 (2011).

204. A. Elschner, W. Loevenich, A. Eiling, and J. Bayley, "ITO Alternative: solution deposited Clevios ^{TM} PEDOT:PSS for transparent conductive applications," http://www.heraeus-clevios.com/media/webmedia_local/media/datenblaetter/White_Paper_ITO_Alternative_Solution_Deposited_Clevios_PEDOT_PSS_materials_for_transparent_conductive_applications.pdf.

205. "PCBM," http://www.solarischem.com/PC61BM_files/PSW - SOL5061A v1.pdf.

206. "Spin Coater," http://www.ossila.com/support/spin_coating_guide/speed_duration.php.

207. D. B. Hall, P. Underhill, and J. M. Torkelson, "Spin coating of thin and ultrathin polymer films," Polym. Eng. Sci. **38**, 2039–2045 (1998).

208. "Spin coating theory," http://www.brewerscience.com/uploads/equipment/datasheets/spintheory.pdf.

209. R. M. Eastment and C. H. B. Mee, "Work function measurements on (100), (110) and (111) surfaces of aluminium," J. Phys. F Met. Phys. **3**, 1738–1745 (1973).

210. D. B. Williams and C. B. Carter, *Transmission Electron Microscopy* (Springer US, 2009).

211. "De Broglie wavelength," http://en.wikipedia.org/w/index.php?title=De_Broglie_wavelength&redirect=no.

212. P. B. Hirsch, A. Howie, R.B. Nicholson, D.W. Pashley, and M.J. Whelan, *Electron Microscopy of Thin Crystals* (Krieger Publishing Company, 1977).

213. Z. L. Wang, "Transmission Electron Microscopy of Shape-Controlled Nanocrystals and Their Assemblies," J. Phys. Chem. B **104**, 1153–1175 (2000).

214. O. Douhéret, L. Lutsen, A. Swinnen, M. Breselge, K. Vandewal, L. Goris, and J. Manca, "Nanoscale electrical characterization of organic photovoltaic blends by conductive atomic force microscopy," Appl. Phys. Lett. **89**, 032107 (2006).

215. C. Ionescu-Zanetti, A. Mechler, S. A. Carter, and R. Lal, "Semiconductive Polymer Blends: Correlating Structure with Transport Properties at the Nanoscale," Adv. Mater. **16**, 385–389 (2004).

216. O. G. Reid, K. Munechika, and D. S. Ginger, "Space charge limited current measurements on conjugated polymer films using conductive atomic force microscopy.," Nano Lett. **8**, 1602–9 (2008).

217. A. Alexeev, J. Loos, and M. M. Koetse, "Nanoscale electrical characterization of semiconducting polymer blends by conductive atomic force microscopy (C-AFM).," Ultramicroscopy **106**, 191–9 (2006).

218. "Atomic force microscopy," http://en.wikipedia.org/wiki/Atomic_force_microscopy.

219. S. Li, M. Meng Lin, M. S. Toprak, D. K. Kim, and M. Muhammed, "Nanocomposites of polymer and inorganic nanoparticles for optical and magnetic applications.," Nano Rev. **1**, 1–19 (2010).

220. O. M. Folarin, E. R. Sadiku, and A. Maity, "Polymer-noble metal nanocomposites: Review," Int. J. Phys. Sci. **6**, 4869–4882 (2011).

221. G. Kickelbick, "Concepts for the incorporation of inorganic building blocks into organic polymers on a nanoscale," Prog. Polym. Sci. **28**, 83–114 (2003).

222. D. W. Hatchett and M. Josowicz, "Composites of intrinsically conducting polymers as sensing nanomaterials.," Chem. Rev. **108**, 746–769 (2008).

223. B. C. Sih and M. O. Wolf, "Metal nanoparticle-conjugated polymer nanocomposites.," Chem. Commun. (Camb). 3375–3384 (2005).

224. S. Pothukuchi, Y. Li, and C. P. Wong, "Development of a novel polymer-metal nanocomposite obtained through the route ofin situ reduction for integral capacitor application," J. Appl. Polym. Sci. **93**, 1531–1538 (2004).

225. S. Woo, J. H. Jeong, H. K. Lyu, Y. S. Han, and Y. Kim, "In situ-prepared composite materials of PEDOT: PSS buffer layer-metal nanoparticles and their application to organic solar cells.," Nanoscale Res. Lett. **7**, 641 (2012).

226. Z. Hu, J. Zhang, Z. Hao, and Y. Zhao, "Influence of doped PEDOT:PSS on the performance of polymer solar cells," Sol. Energy Mater. Sol. Cells **95**, 2763–2767 (2011).

227. D. Duche, P. Torchio, L. Escoubas, F. Monestier, J.-J. Simon, F. Flory, and G. Mathian, "Improving light absorption in organic solar cells by plasmonic contribution," Sol. Energy Mater. Sol. Cells **93**, 1377–1382 (2009).

228. S. Vedraine, P. Torchio, D. Duché, F. Flory, J.-J. Simon, J. Le Rouzo, and L. Escoubas, "Intrinsic absorption of plasmonic structures for organic solar cells," Sol. Energy Mater. Sol. Cells **95**, S57–S64 (2011).

229. M. A. G. Namboothiry, T. Zimmerman, F. M. Coldren, J. Liu, K. Kim, and D. L. Carroll, "Electrochromic properties of conducting polymer metal nanoparticles composites," Synth. Met. **157**, 580–584 (2007).

230. H. A. Atwater and A. Polman, "Plasmonics for improved photovoltaic devices.," Nat. Mater. **9**, 205–13 (2010).

231. K. J. Moreno, I. Moggio, E. Arias, I. Llarena, S. E. Moya, R. F. Ziolo, and H. Barrientos, "Silver nanoparticles functionalized in situ with the conjugated polymer (PEDOT:PSS).," J. Nanosci. Nanotechnol. **9**, 3987–3992 (2009).

232. R. G. Melendez, K. J. Moreno, I. Moggio, E. Arias, A. Ponce, I. Llanera, and S. E. Moya, "On the Influence of Silver Nanoparticles Size in the Electrical Conductivity of PEDOT: PSS," Mater. Sci. Forum **644**, 85–90 (2010).

233. H. S. Noh, E. H. Cho, H. M. Kim, Y. D. Han, and J. Joo, "Organic solar cells using plasmonics of Ag nanoprisms," Org. Electron. **14**, 278–285 (2013).

234. L. Lu, Z. Luo, T. Xu, and L. Yu, "Cooperative plasmonic effect of Ag and Au nanoparticles on enhancing performance of polymer solar cells.," Nano Lett. **13**, 59–64 (2013).

235. V. Bastys, I. Pastoriza-Santos, B. Rodríguez-González, R. Vaisnoras, and L. M. Liz-Marzán, "Formation of Silver Nanoprisms with Surface Plasmons at Communication Wavelengths," Adv. Funct. Mater. **16**, 766–773 (2006).

236. F. Nicodemus, J. Richmond, J. Hsia, I. Ginsburg, and T. Limperis., *Geometrical Considerations and Nomenclature for Reflectance* (U.S. Dept. of Commerce, National Bureau of Standards: for sale by the Supt. of Docs., U.S. Govt. Print. Off., 1977).

237. C. Luo, Y. Zhang, X. Zeng, Y. Zeng, and Y. Wang, "The role of poly(ethylene glycol) in the formation of silver nanoparticles.," J. Colloid Interface Sci. **288**, 444–8 (2005).

238. P.-Y. Silvert, R. Herrera-Urbina, and K. Tekaia-Elhsissen, "Preparation of colloidal silver dispersions by the polyol process," J. Mater. Chem. **7**, 293–299 (1997).

239. G. S. Metraux and C. A. Mirkin, "Rapid Thermal Synthesis of Silver Nanoprisms with Chemically Tailorable Thickness," Adv. Mater. **17**, 412–415 (2005).

240. M. G. Guzman, J. Dille, and S. Godet, "Synthesis of silver nanoparticles by chemical reduction method and their antibacterial activity," Int. J. Chem. Biomol. Eng. **2**, 104–111 (2009).

241. V. G. Pol, D. N. Srivastava, O. Palchik, V. Palchik, M. A. Slifkin, A. M. Weiss, and A. Gedanken, "Sonochemical Deposition of Silver Nanoparticles on Silica Spheres," Langmuir **18**, 3352–3357 (2002).

242. N. Perkas, G. Amirian, G. Applerot, E. Efendiev, Y. Kaganovskii, A. V. Ghule, B.-J. Chen, Y.-C. Ling, and A. Gedanken, "Depositing silver nanoparticles on/in a glass slide by the sonochemical method.," Nanotechnology **19**, 435604 (2008).

243. J. Dai and M. L. Bruening, "Catalytic Nanoparticles Formed by Reduction of Metal Ions in Multilayered Polyelectrolyte Films," Nano Lett. **2**, 497–501 (2002).

244. T. C. Wang, M. F. Rubner, and R. E. Cohen, "Polyelectrolyte Multilayer Nanoreactors for Preparing Silver Nanoparticle Composites: Controlling Metal Concentration and Nanoparticle Size," Langmuir **18**, 3370–3375 (2002).

245. M. Raffi, A. K. Rumaiz, M. M. Hasan, and S. I. Shah, "Studies of the growth parameters for silver nanoparticle synthesis by inert gas condensation," J. Mater. Res. **22**, 3378–3384 (2011).

246. M. Maicu, R. Schmittgens, D. Hecker, D. Glöß, P. Frach, and G. Gerlach, "Synthesis and deposition of metal nanoparticles by gas condensation process," J. Vac. Sci. Technol. A Vacuum, Surfaces, Film. **32**, 02B113 (2014).

247. J. P. Abid, A. W. Wark, P. F. Brevet, and H. H. Girault, "Preparation of silver nanoparticles in solution from a silver salt by laser irradiation," Chem. Commun. 792–793 (2002).

248. R. Jin, Y. C. Cao, E. Hao, G. S. Métraux, G. C. Schatz, and C. A. Mirkin, "Controlling anisotropic nanoparticle growth through plasmon excitation.," Nature **425**, 487–90 (2003).

249. R. Jin, Y. Cao, C. A. Mirkin, K. L. Kelly, G. C. Schatz, and J. G. Zheng, "Photoinduced conversion of silver nanospheres to nanoprisms.," Science **294**, 1901–3 (2001).

250. H. Liang, W. Wang, Y. Huang, S. Zhang, H. Wei, and H. Xu, "Controlled Synthesis of Uniform Silver Nanospheres †," J. Phys. Chem. C **114**, 7427–7431 (2010).
251. B. Pietrobon, M. McEachran, and V. Kitaev, "Synthesis of size-controlled faceted pentagonal silver nanorods with tunable plasmonic properties and self-assembly of these nanorods.," ACS Nano **3**, 21–6 (2009).
252. P. Guyot-Sionnest, "Synthesis and Optical Characterization of Au/Ag Core/Shell Nanorods," J. Phys. Chem. B **108**, 5882–5888 (2004).
253. X. Tang and M. Tsuji, "Syntheses of Silver Nanowires in Liquid Phase," in (2010).
254. S. De, T. M. Higgins, P. E. Lyons, E. M. Doherty, P. N. Nirmalraj, W. J. Blau, J. J. Boland, and J. N. Coleman, "Silver Nanowire Networks as Flexible, Transparent, Conducting Films: Extremely High DC to Optical Conductivity Ratios.," ACS Nano **3**, 1767–74 (2009).
255. P. Zhang, S. Yang, L. Wang, J. Zhao, Z. Zhu, B. Liu, J. Zhong, and X. Sun, "Large-scale uniform Au nanodisk arrays fabricated via x-ray interference lithography for reproducible and sensitive SERS substrate.," Nanotechnology **25**, 245301 (2014).
256. M. Maillard, P. Huang, and L. Brus, "Silver Nanodisk Growth by Surface Plasmon Enhanced Photoreduction of Adsorbed [Ag +]," Nano Lett. **3**, 1611–1615 (2003).
257. S. Chen, Z. Fan, and D. L. Carroll, "Silver Nanodisks: Synthesis, Characterization, and Self-Assembly," J. Phys. Chem. B **106**, 10777–10781 (2002).
258. S. E. Skrabalak, L. Au, X. Li, and Y. Xia, "Facile synthesis of Ag nanocubes and Au nanocages.," Nat. Protoc. **2**, 2182–90 (2007).
259. A. Manna, T. Imae, M. Iida, and N. Hisamatsu, "Formation of Silver Nanoparticles from a N -Hexadecylethylenediamine Silver Nitrate Complex," Langmuir **17**, 6000–6004 (2001).
260. S. Kalele, S. Gosavi, J. Urban, and S. Kulkarni, "Nanoshell particles: synthesis, properties and applications," Curr. Sci. **91**, (2006).
261. C. Xue and C. a Mirkin, "pH-switchable silver nanoprism growth pathways.," Angew. Chem. Int. Ed. Engl. **46**, 2036–8 (2007).
262. J. E. Millstone, S. J. Hurst, G. S. Métraux, J. I. Cutler, and C. a Mirkin, "Colloidal gold and silver triangular nanoprisms.," Small **5**, 646–64 (2009).
263. M. U. Rashid, M. K. H. Bhuiyan, and M. E. Quayum, "Synthesis of Silver Nano Particles (Ag-NPs) and their uses for Quantitative Analysis of Vitamin C Tablets," Dhaka Univ. J. Pharm. Sci. **12**, 1–5 (2013).

264. I. Sondi, D. V Goia, and E. Matijević, "Preparation of highly concentrated stable dispersions of uniform silver nanoparticles," J. Colloid Interface Sci. **260**, 75–81 (2003).
265. K. P. Velikov, G. E. Zegers, and A. van Blaaderen, "Synthesis and Characterization of Large Colloidal Silver Particles," Langmuir **19**, 1384–1389 (2003).
266. Y. Xia, Y. Xiong, B. Lim, and S. E. Skrabalak, "Shape-controlled synthesis of metal nanocrystals: simple chemistry meets complex physics?," Angew. Chem. Int. Ed. Engl. **48**, 60–103 (2009).
267. J. Zhu, F. Zhang, J.-J. Li, and J.-W. Zhao, "The effect of nonhomogeneous silver coating on the plasmonic absorption of Au–Ag core–shell nanorod," Gold Bull. **47**, 47–55 (2013).
268. D. Aherne, D. E. Charles, M. E. Brennan-Fournet, J. M. Kelly, and Y. K. Gun'ko, "Etching-resistant silver nanoprisms by epitaxial deposition of a protecting layer of gold at the edges.," Langmuir **25**, 10165–73 (2009).
269. T. Pal, T. Sau, and N. Jana, "Reversible formation and dissolution of silver nanoparticles in aqueous surfactant media," Langmuir **7463**, 1481–1485 (1997).
270. A. P. Kulkarni, K. M. Noone, K. Munechika, S. R. Guyer, and D. S. Ginger, "Plasmon-enhanced charge carrier generation in organic photovoltaic films using silver nanoprisms.," Nano Lett. **10**, 1501–5 (2010).
271. J. Y. Kim, J. H. Jung, D. E. Lee, and J. Joo, "Enhancement of electrical conductivity of poly(3,4-ethylenedioxythiophene)/poly(4-styrenesulfonate) by a change of solvents," Synth. Met. **126**, 311–316 (2002).
272. O. P. Dimitriev, D. a. Grinko, Y. V. Noskov, N. a. Ogurtsov, and A. a. Pud, "PEDOT:PSS films—Effect of organic solvent additives and annealing on the film conductivity," Synth. Met. **159**, 2237–2239 (2009).
273. J. Ouyang, Q. Xu, C.-W. Chu, Y. Yang, G. Li, and J. Shinar, "On the mechanism of conductivity enhancement in poly(3,4-ethylenedioxythiophene):poly(styrene sulfonate) film through solvent treatment," Polymer (Guildf). **45**, 8443–8450 (2004).
274. J. Huang, P. F. Miller, J. C. de Mello, A. J. de Mello, and D. D. C. Bradley, "Influence of thermal treatment on the conductivity and morphology of PEDOT/PSS films," Synth. Met. **139**, 569–572 (2003).
275. Q. Feng, K. Du, Y.-K. Li, P. Shi, and Q. Feng, "Effect of annealing on performance of PEDOT:PSS/n-GaN Schottky solar cells," Chinese Phys. B **23**, 077303 (2014).

276. G. Greczynski, T. Kugler, and W. . Salaneck, "Characterization of the PEDOT-PSS system by means of X-ray and ultraviolet photoelectron spectroscopy," Thin Solid Films **354**, 129–135 (1999).

277. R. Kiebooms, A. Aleshin, K. Hutchison, F. Wudl, and A. Heeger, "Doped poly(3,4-ethylenedioxythiophene) films: Thermal, electromagnetical and morphological analysis," Synth. Met. **101**, 436–437 (1999).

278. Y. Kim, a Ballantyne, J. Nelson, and D. Bradley, "Effects of thickness and thermal annealing of the PEDOT:PSS layer on the performance of polymer solar cells," Org. Electron. **10**, 205–209 (2009).

279. I. Winter, C. Reese, J. Hormes, G. Heywang, and F. Jonas, "The thermal ageing of poly(3,4-ethylenedioxythiophene). An investigation by X-ray absorption and X-ray photoelectron spectroscopy," Chem. Phys. **194**, 207–213 (1995).

280. D. M. Huang, S. a. Mauger, S. Friedrich, S. J. George, D. Dumitriu-LaGrange, S. Yoon, and A. J. Moulé, "The Consequences of Interface Mixing on Organic Photovoltaic Device Characteristics," Adv. Funct. Mater. **21**, 1657–1665 (2011).

281. S. C. C. Veenstra, L. H. H. Slooff, W. J. H. J. H. Verhees, A. Barbot, F. O. O. Lenzmann, J. M. M. Kroon, H. J. Bolink, M. Sessolo, and E. M. Cobussen-Pool, "Unconventional device concepts for polymer solar cells," in *24th EuropeanEuropean Photovoltaic Solar Energy Conference and Exhibition* (WIP-Munich, 2009), pp. 84–88.

282. A. Diacon, L. Derue, C. Lecourtier, O. Dautel, G. Wantz, and P. Hudhomme, "Cross-linkable azido C 60 -fullerene derivatives for efficient thermal stabilization of polymer bulk-heterojunction solar cells," J. Mater. Chem. C **2**, 7163 (2014).

283. W. H. Kim, G. P. Kushto, H. Kim, and Z. H. Kafafi, "Effect of annealing on the electrical properties and morphology of a conducting polymer used as an anode in organic light-emitting devices," J. Polym. Sci. Part B Polym. Phys. **41**, 2522–2528 (2003).

284. H. Snaith, H. Kenrick, M. Chiesa, and R. Friend, "Morphological and electronic consequences of modifications to the polymer anode “PEDOT:PSS,”" Polymer (Guildf). **46**, 2573–2578 (2005).

285. L. A. . Pettersson, S. Ghosh, and O. Inganäs, "Optical anisotropy in thin films of poly(3,4-ethylenedioxythiophene)–poly(4-styrenesulfonate)," Org. Electron. **3**, 143–148 (2002).

286. P. Vanlaeke, a. Swinnen, I. Haeldermans, G. Vanhoyland, T. Aernouts, D. Cheyns, C. Deibel, J. D’Haen, P. Heremans, J. Poortmans, and J. V. Manca, "P3HT/PCBM bulk heterojunction solar cells: Relation between morphology and electro-optical characteristics," Sol. Energy Mater. Sol. Cells **90**, 2150–2158 (2006).

287. T. J. Savenije, J. E. Kroeze, X. Yang, and J. Loos, "The Effect of Thermal Treatment on the Morphology and Charge Carrier Dynamics in a Polythiophene-Fullerene Bulk Heterojunction," Adv. Funct. Mater. **15**, 1260–1266 (2005).

288. J. Huang, G. Li, and Y. Yang, "Influence of composition and heat-treatment on the charge transport properties of poly(3-hexylthiophene) and [6,6]-phenyl C[sub 61]-butyric acid methyl ester blends," Appl. Phys. Lett. **87**, 112105 (2005).

289. Q. Liu, Z. Liu, X. Zhang, L. Yang, N. Zhang, G. Pan, S. Yin, Y. Chen, and J. Wei, "Polymer Photovoltaic Cells Based on Solution-Processable Graphene and P3HT," Adv. Funct. Mater. **19**, 894–904 (2009).

290. G. F. Malgas, D. E. Motaung, and C. J. Arendse, "Temperature-dependence on the optical properties and the phase separation of polymer–fullerene thin films," J. Mater. Sci. **47**, 4282–4289 (2012).

291. G. Nagarjuna and D. Venkataraman, "Strategies for controlling the active layer morphologies in OPVs," J. Polym. Sci. Part B Polym. Phys. **50**, 1045–1056 (2012).

292. X. Yang, J. K. J. van Duren, R. A. J. Janssen, M. A. J. Michels, and J. Loos, "Morphology and Thermal Stability of the Active Layer in Poly(p -phenylenevinylene)/Methanofullerene Plastic Photovoltaic Devices," Macromolecules **37**, 2151–2158 (2004).

293. G. Li, V. Shrotriya, J. Huang, Y. Yao, T. Moriarty, K. Emery, and Y. Yang, "High-efficiency solution processable polymer photovoltaic cells by self-organization of polymer blends," Nat. Mater. **4**, 864–868 (2005).

294. C.-W. Chu, H. Yang, W.-J. Hou, J. Huang, G. Li, and Y. Yang, "Control of the nanoscale crystallinity and phase separation in polymer solar cells," Appl. Phys. Lett. **92**, 103306 (2008).

295. F. C. Krebs, ed., *Polymeric Solar Cells: Materials, Design, Manufacture* (DEStech Publications, Inc, 2010), p. 42.

296. L. Li, G. Lu, and X. Yang, "Improving performance of polymer photovoltaic devices using an annealing-free approach via construction of ordered aggregates in solution," J. Mater. Chem. **18**, 1984 (2008).

297. P. Brown, D. Thomas, A. Köhler, J. Wilson, J.-S. Kim, C. Ramsdale, H. Sirringhaus, and R. Friend, "Effect of interchain interactions on the absorption and emission of poly(3-hexylthiophene)," Phys. Rev. B **67**, 064203 (2003).

298. N. Kiriy, E. Jähne, H.-J. Adler, M. Schneider, A. Kiriy, G. Gorodyska, S. Minko, D. Jehnichen, P. Simon, A. A. Fokin, and M. Stamm, "One-Dimensional Aggregation of Regioregular Polyalkylthiophenes," Nano Lett. **3**, 707–712 (2003).

299. J. K. Keum, K. Xiao, I. N. Ivanov, K. Hong, J. F. Browning, G. S. Smith, M. Shao, K. C. Littrell, A. J. Rondinone, E. Andrew Payzant, J. Chen, and D. K. Hensley, "Solvent quality-induced nucleation and growth of parallelepiped nanorods in dilute poly(3-hexylthiophene) (P3HT) solution and the impact on the crystalline morphology of solution-cast thin film," CrystEngComm **15**, 1114 (2013).

300. W. Yu, D. Yang, X. Zhu, X. Wang, G. Tu, D. Fan, J. Zhang, and C. Li, "Control of nanomorphology in all-polymer solar cells via assembling nanoaggregation in a mixed solution.," ACS Appl. Mater. Interfaces **6**, 2350–5 (2014).

301. F. Yang, M. Shtein, and S. R. Forrest, "Controlled growth of a molecular bulk heterojunction photovoltaic cell," Nat. Mater. **4**, 37–41 (2004).

302. Y. Kim, S. A. Choulis, J. Nelson, D. D. C. Bradley, S. Cook, and J. R. Durrant, "Device annealing effect in organic solar cells with blends of regioregular poly(3-hexylthiophene) and soluble fullerene," Appl. Phys. Lett. **86**, 063502 (2005).

303. N. D. Treat, C. G. Shuttle, M. F. Toney, C. J. Hawker, and M. L. Chabinyc, "In situ measurement of power conversion efficiency and molecular ordering during thermal annealing in P3HT:PCBM bulk heterojunction solar cells," J. Mater. Chem. **21**, 15224 (2011).

304. K. Tremel and S. Ludwigs, "Morphology of P3HT in thin films in relation to optical and electrical properties," in *Advances in Polymer Science*, A. Abe, A.-C. Albertsson, and G. W. Coates, eds. (Springer Berlin Heidelberg, 2014).

305. M. Sundberg, O. Inganäs, S. Stafström, G. Gustafsson, and B. Sjögren, "Optical absorption of poly(3-alkylthiophenes) at low temperatures," Solid State Commun. **71**, 435–439 (1989).

306. F.-X. Xie, W. C. H. Choy, C. C. D. Wang, W. E. I. Sha, and D. D. S. Fung, "Improving the efficiency of polymer solar cells by incorporating gold nanoparticles into all polymer layers," Appl. Phys. Lett. **99**, 153304 (2011).

307. W. C. H. Choy, ed., *Organic Solar Cells: Materials and Device Physics*, Green Energy and Technology (Springer London, 2013).

308. M. Xue, L. Li, B. J. Tremolet de Villers, H. Shen, J. Zhu, Z. Yu, A. Z. Stieg, Q. Pei, B. J. Schwartz, and K. L. Wang, "Charge-carrier dynamics in hybrid plasmonic organic solar cells with Ag nanoparticles," Appl. Phys. Lett. **98**, 253302 (2011).

309. D. Kong, J. Z. Y. Tan, F. Yang, J. Zeng, and X. Zhang, "Electrodeposited Ag nanoparticles on TiO2 nanorods for enhanced UV visible light photoreduction CO2 to CH4," Appl. Surf. Sci. **277**, 105–110 (2013).

310. W. Yoon, K. Jung, J. Liu, T. Duraisamy, R. Revur, F. L. Teixeira, S. Sengupta, and P. R. Berger, "Plasmon-enhanced optical absorption and photocurrent in organic bulk heterojunction photovoltaic devices using self-assembled layer of silver nanoparticles," Sol. Energy Mater. Sol. Cells **94**, 128–132 (2010).

311. N. G. Semaltianos, W. Perrie, S. Romani, R. J. Potter, G. Dearden, and K. G. Watkins, "Polymer-nanoparticle composites composed of PEDOT:PSS and nanoparticles of Ag synthesised by laser ablation," Colloid Polym. Sci. **290**, 213–220 (2011).

312. S.-J. Wang, Y.-J. Choi, and H.-H. Park, "Investigation of Ag-poly(3,4-ethylenedioxythiophene):polystyrene sulfonate nanocomposite films prepared by a one-step aqueous method," J. Appl. Phys. **109**, 124902 (2011).

313. S. K. . Jönsson, J. Birgerson, X. Crispin, G. Greczynski, W. Osikowicz, A. . Denier van der Gon, W. . Salaneck, and M. Fahlman, "The effects of solvents on the morphology and sheet resistance in poly(3,4-ethylenedioxythiophene)–polystyrenesulfonic acid (PEDOT–PSS) films," Synth. Met. **139**, 1–10 (2003).

314. S. Timpanaro, M. Kemerink, F. J. Touwslager, M. M. De Kok, and S. Schrader, "Morphology and conductivity of PEDOT/PSS films studied by scanning–tunneling microscopy," Chem. Phys. Lett. **394**, 339–343 (2004).

315. Y. H. Kim, C. Sachse, M. L. Machala, C. May, L. Müller-Meskamp, and K. Leo, "Highly Conductive PEDOT:PSS Electrode with Optimized Solvent and Thermal Post-Treatment for ITO-Free Organic Solar Cells," Adv. Funct. Mater. **21**, 1076–1081 (2011).

316. J. Ouyang, C.-W. Chu, F.-C. Chen, Q. Xu, and Y. Yang, "High-Conductivity Poly(3,4-ethylenedioxythiophene):Poly(styrene sulfonate) Film and Its Application in Polymer Optoelectronic Devices," Adv. Funct. Mater. **15**, 203–208 (2005).

317. A. Kumar, S. Sista, and Y. Yang, "Dipole induced anomalous S-shape I-V curves in polymer solar cells," J. Appl. Phys. **105**, 094512 (2009).

318. "Polyethylene glycol," http://en.wikipedia.org/wiki/Polyethylene_glycol.

319. "Polyol process," http://www.rsc.org/publishing/journals/prospect/ontology.asp?id=CMO:0002167&MSID=b9nr00089e.

320. R. Brayner, F. Fiévet, and T. Coradin, eds., *Nanomaterials: A Danger or a Promise?* (Springer London, 2013), p. 2.

321. K. Shameli, M. Bin Ahmad, S. D. Jazayeri, S. Sedaghat, P. Shabanzadeh, H. Jahangirian, M. Mahdavi, and Y. Abdollahi, "Synthesis and characterization of polyethylene glycol mediated silver nanoparticles by the green method.," Int. J. Mol. Sci. **13**, 6639–50 (2012).

322. Y. Liang, Z. Xu, J. Xia, S.-T. Tsai, Y. Wu, G. Li, C. Ray, and L. Yu, "For the bright future-bulk heterojunction polymer solar cells with power conversion efficiency of 7.4%.," Adv. Mater. **22**, E135–8 (2010).

323. S. Ben Dkhil, D. Duché, M. Gaceur, A. K. Thakur, F. B. Aboura, L. Escoubas, J.-J. Simon, A. Guerrero, J. Bisquert, G. Garcia-Belmonte, Q. Bao, M. Fahlman, C. Videlot-Ackermann, O. Margeat, and J. Ackermann, "Interplay of Optical, Morphological, and Electronic Effects of ZnO Optical Spacers in Highly Efficient Polymer Solar Cells," Adv. Energy Mater. n/a–n/a (2014).

324. S. J. Oldenburg, "Silver Nanoparticles: Properties and Applications," http://www.sigmaaldrich.com/materials-science/nanomaterials/silver-nanoparticles.html.

325. J. J. Mock, D. R. Smith, and S. Schultz, "Local Refractive Index Dependence of Plasmon Resonance Spectra from Individual Nanoparticles," Nano Lett. **3**, 485–491 (2003).

326. A. P. Kulkarni, K. Munechika, K. M. Noone, J. M. Smith, and D. S. Ginger, "Phase transfer of large anisotropic plasmon resonant silver nanoparticles from aqueous to organic solution.," Langmuir **25**, 7932–9 (2009).